Karol Miller

Poul M.F. Nielsen

Editors

Computational
Biomechanics for
Medicine

2 Springer

Computational Biomechanics for Medicine

Karol Miller · Poul M.F. Nielsen
Editors

Computational Biomechanics for Medicine

Springer

Editors
Karol Miller
Intelligent Systems for
  Medicine Laboratory
The University of Western
  Australia
35 Stirling Highway
Crawley/Perth WA 6009
Australia
kmiller@mech.uwa.edu.au

Poul M.F. Nielsen
Auckland Bioengineering Institute
The University of Auckland
Level 6
70 Symonds Street
Auckland 1030
New Zealand
p.nielsen@auckland.ac.nz

Printed on acid-free paper

Preface

A novel partnership between surgeons and machines, made possible by advances in computing and engineering technology, could overcome many of the limitations of traditional surgery. By extending surgeons' ability to plan and carry out surgical interventions more accurately and with less trauma, computer-integrated surgery (CIS) systems could help to improve clinical outcomes and the efficiency of healthcare delivery. CIS systems could have a similar impact on surgery to that long since realized in computer-integrated manufacturing (CIM). Mathematical modeling and computer simulation have proved tremendously successful in engineering. Computational mechanics has enabled technological developments in virtually every area of our lives. One of the greatest challenges for mechanists is to extend the success of computational mechanics to fields outside traditional engineering, in particular to biology, the biomedical sciences, and medicine.

Computational Biomechanics for Medicine Workshop series was established in 2006 with the first meeting held in Copenhagen. The fourth workshop was held in conjunction with the Medical Image Computing and Computer Assisted Intervention Conference (MICCAI 2009) in London on 24 September 2009. It provided an opportunity for specialists in computational sciences to present and exchange opinions on the possibilities of applying their techniques to computer-integrated medicine.

Computational Biomechanics for Medicine IV was organized into two streams: Computational Biomechanics of Soft Tissues and Flow, and Computational Biomechanics of Tissues of Musculoskeletal System. The application of advanced computational methods to the following areas was discussed:

- Medical image analysis
- Image-guided surgery
- Surgical simulation
- Surgical intervention planning
- Disease prognosis and diagnosis
- Injury mechanism analysis
- Implant and prostheses design
- Medical robotics

After rigorous review of full (8–12 pages) manuscripts we accepted 13 chapters, collected in this volume. The proceedings also include abstracts of two invited lectures by world-leading researchers Professor Perumal Nithiarasu from Swansea University and Professor Marcus Pandy from the University of Melbourne.

Information about Computational Biomechanics for Medicine Workshops, including Proceedings of previous meetings, is available at http://cbm.mech. uwa.edu.au/. We would like to thank the MICCAI 2009 organizers for help with administering the Workshop, invited lecturers for deep insights into their research fields, the authors for submitting high-quality work, and the reviewers for helping with paper selection.

Crawley/Perth, Australia   Karol Miller
Auckland, New Zealand   Poul M.F. Nielsen

Contents

Contributors

Nadya Amor Division of Biomechanics and Engineering Design, Department of Mechanical Engineering, Katholieke Universiteit Leuven, Heverlee 3001, Leuven, Belgium

Thibaut Bardyn Institute for Surgical Technology & Biomechanics, University of Bern, Bern, Switzerland

Philippe Büchler Institute for Surgical Technology & Biomechanics, University of Bern, Bern, Switzerland

Kiyoyuki Chinzei Surgical Assist Technology Group, Institute for Human Science and Biomedical Engineering, National Institute of Advanced Industrial Science and Technology (AIST), Tsukuba, Ibaraki 305-8564, Japan

Yong-Suk Choi Department of Oral and Maxillofacial Radiology, School of Dentistry, Kyung Hee University, Seoul 130-702, Republic of Korea

Samjin Choi Department of Biomedical Engineering, School of Medicine, Kyung Hee University, Seoul 130-702, Republic of Korea; Healthcare Industry Research Institute, Seoul 130-702, Republic of Korea

Jae-Hoon Chung Auckland Bioengineering Institute, The University of Auckland, Auckland, New Zealand

Ginmo Chung Department of Mathematics, University of California, Los Angeles, CA, USA

François Chung Asclepios Project, INRIA, Sophia Antipolis, France

Hervé Delingette Asclepios Project, INRIA, Sophia Antipolis, France

Ivo D. Dinov Laboratory of Neuro Imaging, University of California, Los Angeles, CA, USA

Tonmoy Dutta-Roy School of Mechanical Engineering, The University of Western Australia, Crawley, WA 6009, Australia

Liesbet Geris Division of Biomechanics and Engineering Design, Department of Mechanical Engineering, Katholieke Universiteit Leuven, Heverlee 3001, Leuven, Belgium

Tobias Heimann Asclepios Project, INRIA, Sophia Antipolis, France

Ralph P. Highnam Highnam Associates Limited, Wellington, New Zealand

Harvey Ho Auckland Bioengineering Institute, The University of Auckland, Auckland, New Zealand

Andrew Holden Department of Radiology, Auckland Hospital, Auckland, New Zealand

Peter Hunter Auckland Bioengineering Institute, The University of Auckland, Auckland, New Zealand

Grand Roman Joldes Intelligent Systems for Medicine Laboratory, School of Mechanical Engineering, The University of Western Australia, Crawley 6009, WA, Australia

Kyung-Sook Kim Department of Biomedical Engineering, School of Medicine, Kyung Hee University, Seoul 130-702, Republic of Korea; Healthcare Industry Research Institute, Seoul 130-702, Republic of Korea

Jennifer A. Kruger Department of Sport and Exercise Science, The University of Auckland, Auckland, New Zealand

David Ladd Auckland Bioengineering Institute, The University of Auckland, Auckland, New Zealand

Hans Lamecker Asclepios Project, INRIA, Sophia Antipolis, France

Xabier Larrea Institute for Surgical Technology & Biomechanics, University of Bern, Bern, Switzerland

Angela W.C. Lee Auckland Bioengineering Institute, The University of Auckland, Auckland, New Zealand

Gi-Ja Lee Department of Biomedical Engineering, School of Medicine, Kyung Hee University, Seoul 130-702, Republic of Korea; Healthcare Industry Research Institute, Seoul 130-702, Republic of Korea

Xinshan Li Auckland Bioengineering Institute, The University of Auckland, Auckland, New Zealand

Jiajie Ma Intelligent Systems for Medicine Laboratory, School of Mechanical Engineering, The University of Western Australia, Crawley-Perth 6009, WA, Australia

Karol Miller Intelligent Systems for Medicine Laboratory, School of Mechanical Engineering, The University of Western Australia, Crawley-Perth 6009, WA, Australia

José Moreno Laboratory of Robotics and Artificial Vision, University of Extremadura, Cáceres, Spain

José L. Moyano Department of Laparoscopic Surgery, Minimally Invasive Surgery Centre Jesús Usón, Cáceres, Spain

Martyn P. Nash Auckland Bioengineering Institute, The University of Auckland, Auckland, New Zealand

Poul M.F. Nielsen Auckland Bioengineering Institute, The University of Auckland, Auckland, New Zealand

Perumal Nithiarasu Civil and Computational Engineering Centre, Swansea University, Swansea SA2 8PP, UK

José B. Pagador Department of Laparoscopic Surgery, Minimally Invasive Surgery Centre Jesús Usón, Cáceres, Spain

Marcus Pandy Department of Mechanical Engineering, University of Melbourne, Melbourne, Australia

Jeong-Hoon Park Department of Biomedical Engineering, School of Medicine, Kyung Hee University, Seoul 130-702, Republic of Korea; Healthcare Industry Research Institute, Seoul 130-702, Republic of Korea

Ji-Hye Park Department of Biomedical Engineering, School of Medicine, Kyung Hee University, Seoul 130-702, Republic of Korea; Healthcare Industry Research Institute, Seoul 130-702, Republic of Korea

Young-Ho Park Department of Biomedical Engineering, School of Medicine, Kyung Hee University, Seoul 130-702, Republic of Korea; Healthcare Industry Research Institute, Seoul 130-702, Republic of Korea

Hun-Kuk Park Department of Biomedical Engineering, School of Medicine, Kyung Hee University, Seoul 130-702, Republic of Korea; Healthcare Industry Research Institute, Kyung Hee University, Seoul 130-702, Republic of Korea; Program of Medical Engineering, Kyung Hee University, Seoul 130-702, Republic of Korea

Vijay Rajagopal Auckland Bioengineering Institute, The University of Auckland, Auckland, New Zealand

Mauricio Reyes Institute for Surgical Technology & Biomechanics, University of Bern, Bern, Switzerland

Francisco M. Sánchez-Margallo Department of Laparoscopic Surgery, Minimally Invasive Surgery Centre Jesús Usón, Cáceres, Spain

Juan A. Sánchez-Margallo Department of Laparoscopic Surgery, Minimally Invasive Surgery Centre Jesús Usón, Cáceres, Spain

Surya Singh Intelligent Systems for Medicine Laboratory, School of Mechanical Engineering, The University of Western Australia, Crawley-Perth 6009, WA, Australia

Arthur W. Toga Laboratory of Neuro Imaging, University of California, Los Angeles, CA, USA

Jesús Usón Department of Laparoscopic Surgery, Minimally Invasive Surgery Centre Jesús Usón, Cáceres, Spain

Hans Van Oosterwyck Division of Biomechanics and Engineering Design, Department of Mechanical Engineering, Katholieke Universiteit Leuven, Heverlee 3001, Leuven, Belgium

Jos Vander Sloten Division of Biomechanics and Engineering Design, Department of Mechanical Engineering, Katholieke Universiteit Leuven, Heverlee 3001, Leuven, Belgium

Luminita A. Vese Department of Mathematics, University of California, Los Angeles, CA, USA

Ruth Warren Department of Radiology, Addenbrooke's Hospital, Cambridge, UK

Toshikatsu Washio Surgical Assist Technology Group, Institute for Human Science and Biomedical Engineering, National Institute of Advanced Industrial Science and Technology (AIST), Tsukuba, Ibaraki 305-8564, Japan

Adam Wittek Intelligent Systems for Medicine Laboratory, School of Mechanical Engineering, The University of Western Australia, Crawley-Perth 6009, WA, Australia

Part I
Computational Biomechanics of Soft Tissues and Flow

Chapter 1
Patient-Specific Modelling of Cardiovascular and Respiratory Flow Problems – Challenges

Perumal Nithiarasu

Abstract Patient-specific or subject-specific biofluid dynamics modelling has been an active area of research over the last 10 years. This is one of the advancing areas of research in computer-assisted biomechanics and it has started making an impact in terms of clinical use. However, the progress has been slow and the day-to-day use of modelling as a clinical tool is a long way away. This presentation investigates the genuine reasons for the slow progress and it also addresses how progress could be accelerated.

A patient-specific study normally includes some form of data from a patient. For biofluid dynamics studies, scan and/or flow rate is often available. The scan is first processed and the geometry is reconstructed using appropriate reconstruction tools. Establishing the accuracy of reconstruction and the implications of inaccuracy is still an unresolved research problem. The reconstructed geometry is meshed and a flow solver along with an appropriate flow/structure boundary condition (measured or assumed) is applied to obtain a steady- or unsteady-state solution depending on the requirement. The solution could be used either in making a clinical decision or to understand the problem better.

The main challenges of patient-specific fluid dynamics studies are in the translational aspects. Many research groups all over the world are carrying out research in this area but no consistent effort is made in identifying the problems relevant to translational aspects. The translational element consists of two difficulties. They are (i) technological issues and (ii) implementation issues. Technological issues are associated with the accuracy and difficulties associated with automating the technology. The implementation issues include the general scepticism and general lack of strong interdisciplinary understanding. This lecture will discuss both aspects in detail.

Keywords Patient-specific modelling · CFD · Blood flow

P. Nithiarasu (✉)
Civil and Computational Engineering Centre, Swansea University, Swansea SA2 8PP, UK
e-mail: p.nithiarasu@swansea.ac.uk

Chapter 2
MRI Tissue Segmentation Using a Variational Multilayer Approach

Ginmo Chung, Ivo D. Dinov, Arthur W. Toga, and Luminita A. Vese

Abstract We propose novel piecewise-constant minimization models for three-dimensional MRI brain data segmentation into white matter, gray matter, and cerebrospinal fluid. The proposed approaches are based on a multilayer or nested implicit surface evolution in variational form, well adapted to this problem. We propose two models, with and without using prior spatial information. The prior information is in the form of a probabilistic brain atlas, encoding spatial information of these three anatomical structures. Extensive experimental results and comparisons with manual segmentation and with automated segmentation are presented, together with quantitative assessment.

Keywords MRI image segmentation · Variational level set methods · Active surfaces · Partial differential equations · Multilayer approach

1 Introduction

Three-dimensional brain segmentation of magnetic resonance imaging (MRI) volumes is the process of obtaining two, or more, tissue classes that carry significant anatomical information. This process is critical for the estimation of subject-specific proportions of white matter (WM), gray matter (GM), and cerebrospinal fluid (CSF)–important markers of growth, aging, and disease; construction of deterministic and probabilistic population-based atlases of brain tissue types; carrying robust functional activation analyses, where the perfusional imaging data is restricted over the gray matter or white matter, according to the anatomical segmentation; for various clinical applications (e.g., real-time estimation and guidance for surgeons in the

G. Chung (✉)
Department of Mathematics, University of California, Los Angeles, CA, USA
e-mail: senninha@math.ucla.edu

operating room, for correlating of neurocognitive and demographic measures with tissue-specific imaging characteristics, for monitoring brain functional or anatomical changes induced by treatment regiments). Traditionally, the MRI segmentation has been done manually. That is, someone with knowledge of anatomy outlines target tissues on each image slice in a 3D volume data. The task is very tedious and time consuming for the segmenter. Combined with the difficulty to accurately delineate complex 3D structures, it makes the manual segmentation impractical on large data sets.

We propose here two models for MRI tissue segmentation into white matter, gray matter, and cerebrospinal fluid. The mathematical model that we employ is a piecewise-constant segmentation model in a variational framework. The problem that we solve is related with [1, 2, 24, 25], where curve evolution techniques and implicit boundary representation were proposed to solve particular cases of the Mumford–Shah segmentation problem [13]. In the standard approach of front propagation [14], only one level line is used to represent the boundary. But we can use more than one level line of the same implicit function ϕ to represent nested boundaries [3, 4]. In this chapter we adapt this idea to the specific case of 3D MRI brain segmentation into white matter, gray matter, and cerebrospinal fluid. The nested structure of level lines is appropriate for such application. We thus propose two models: the first one does not use any prior anatomical information, while the second model uses prior spatial information of the WM, GM, and CSF, in the form of a probabilistic atlas. We show comparison and sensitivity analysis with manual segmentation (gold standard) and with an automatic segmentation method called partial volume correction (PVC) [17]. Our proposed models are simple, robust, with faster computations than by the automatic PVC method, and give satisfactory results without any prior or with minimum atlas prior.

Related work on MRI brain segmentation and tissue classification is semi-automated segmentation of cortical subvolumes via hierarchical mixture modeling by Ratnanather et al. [15]; comparative assessment of statistical brain MR image segmentation algorithms and their impact on partial volume correction in PET by Zaidi et al. [27]; whole brain segmentation by Fischl et al. [6]; segmentation of MR image based on maximum a posteriori by Liu et al. [11]; segmentation of brain MR images using hidden Markov random field and the E-M algorithm by Zhang et al. [28]; brain segmentation and generation of cortical surfaces by Joshi et al. [9]; performance analysis of automatic techniques for tissue classification in MRI images by Kollokian [10]; cortical surface segmentation and mapping by Tosun et al. [22, 23]; CRUISE: cortical reconstruction using implicit surface evolution by Han et al. [7], among other works.

Our proposed methods are different from the above-mentioned methods since we exploit the nested structure of iso-surfaces in a multilayer representation. Moreover, even without any prior, satisfactory results are obtained, almost of the same quality as those produced by the PVC method, but in a very simple framework and with reduced computational time. The proposed methods can be further improved or modified for other applications. Additional results and more details can be found in the UCLA C.A.M. Report [5].

2 Proposed Multilayer MRI Segmentation Models

We apply the multilayer level set representation idea to 3D brain MR images. The difficulty is that the data, while noisy, has low contrast and is a blurry version of the true data, due to the resolution. Anatomical boundaries are not clear, thus standard general methods of segmentation do not give satisfactory results. In our proposed approach, we first exploit the fact that the non-brain region has intensity value 0. We introduce the characteristic function $\chi_B(x)$ in three dimensions for the brain region. That is, $\chi_B(x) = 1$ when x belongs to the brain region and $\chi_B(x) = 0$ when x belongs to the non-brain region. We then evolve the surface only within the region where $\chi_B(x) = 1$, by restricting all energy terms to the brain region. This avoids segmenting the non-brain region and thus reduces non-desired artifacts and complexity. One function ϕ with two distinct iso-surfaces is sufficient to segment the volumetric MR images into three tissue types. Let $\Omega \subset \mathbb{R}^3$ be the spatial volume (a rectangular parallelepiped), $f : \Omega \rightarrow \mathbb{R}$ the MRI volume data, $\phi : \Omega \rightarrow \mathbb{R}$ the unknown level set function; c_{GM}, c_{WM}, c_{CSF} are unknown intensity averages over the disjoint regions that would correspond to the white matter, the gray matter, and the cerebrospinal fluid, respectively; H denotes the one-dimensional Heaviside function: $H(\phi(x) - l) = 1$ if $\phi(x) \geq l$ and $H(\phi(x) - l) = 0$ if $\phi(x) < l$. Only the brain region will be segmented into three regions $\{x \in B, \phi(x) < 0\}$, $\{x \in B, 0 \leq \phi(x) \leq l\}$, and $\{x \in B, \phi(x) > l\}$. The models can be easily extended to tissue classification into more than three classes.

Multilayer segmentation model without atlas prior Assuming known only the desired number of classes, we propose to minimize the energy:

$$F(c_{GM}, c_{WM}, c_{CSF}, \phi) = \lambda_1 \int_\Omega |f(x) - c_{GM}|^2 \chi_B(x) H(-\phi(x))dx$$

$$+ \lambda_2 \int_\Omega |f(x) - c_{WM}|^2 \chi_B(x) H(\phi(x)) H(l - \phi(x))dx$$

$$+ \lambda_3 \int_\Omega |f(x) - c_{CSF}|^2 \chi_B(x) H(\phi(x) - l)dx$$

$$+ \mu_1 \int_\Omega |\nabla H(\phi)| \chi_B(x)dx + \mu_2 \int_\Omega |\nabla H(\phi - l)| \chi_B(x)dx.$$

The first three terms denote data fidelity terms, while the last two terms are regularizing terms, giving the surface area of implicit boundaries $\phi(x) = 0$ and $\phi(x) = l$. λ_i, μ_i, and level l are positive parameters. Minimizing the above energy F alternately with respect to the unknowns yields the associated Euler–Lagrange equations, parameterizing the descent direction by an artificial time $t \geq 0$: $c_{GM} = \frac{\int_\Omega f(x) H(-\phi) \chi_B dx}{\int_\Omega H(-\phi) \chi_B dx}$, $c_{WM} = \frac{\int_\Omega f(x) H(\phi) H(l-\phi) \chi_B dx}{\int_\Omega H(\phi) H(l-\phi) \chi_B dx}$, $c_{CSF} = \frac{\int_\Omega f(x) H(\phi-l) \chi_B dx}{\int_\Omega H(\phi-l) \chi_B dx}$, and

$$\frac{\partial \phi}{\partial t} = \delta(\phi) \left[\lambda_1 |f - c_{GM}|^2 \chi_B - \lambda_2 |f - c_{WM}|^2 \chi_B H(l - \phi) + \mu_1 \text{div} \left(\chi_B \frac{\nabla \phi}{|\nabla \phi|} \right) \right]$$

$$+ \delta(\phi - l) \left[\lambda_2 |f - c_{WM}|^2 \chi_B H(\phi) - \lambda_3 |f - c_{CSF}|^2 \chi_B + \mu_2 \text{div} \left(\chi_B \frac{\nabla \phi}{|\nabla \phi|} \right) \right].$$

The above partial differential equation in ϕ is discretized by semi-implicit finite difference scheme and fixed-point iteration to steady state, while updating c_{GM}, c_{WM}, c_{CSF} at each iteration. The non-differentiable Heaviside function H is approximated and substituted by a smoother differentiable function H_ϵ, as in [1, 2]. In general we use $\lambda_i = 1$, $\mu_1 = \mu_2$. Note that coefficients λ_i can be automatically selected during the process by introducing the variance on each region as an unknown [18].

Multilayer segmentation model with brain atlas prior The objects to be segmented from MR images are the actual anatomical structures, which are complex in shape and exhibit considerable variability from person to person [8]. Combined with limitations in the imaging equipment and the motion artifacts that may appear in the images due to movement of the subject, MRI segmentation is challenging. To cope with such difficulties, we propose to incorporate prior spatial information in the form of a brain atlas into the multilayer model (the model introduced above already gives satisfactory results, but sometimes prior information is needed to improve the segmentation). The atlas that we use incorporates the most likely locations and shapes of anatomical structures and the spatial relationships between them [16]. In Fig. 2.1 we show 2D and 3D views of the brain atlas information. The atlas consists of three channels (corresponding to WM, GM, and CSF), and the intensity value of the atlas in a channel for each voxel is the probability of that voxel belonging to the corresponding anatomical structure. The given atlas channels are denoted by $(A_{GM}, A_{WM}, A_{CSF})$. The energy functional to be minimized, which incorporates the atlas prior, is

$$
\begin{aligned}
F_A(c_{GM}, & c_{WM}, c_{CSF}, \phi) \\
&= \int_\Omega (a_1|f - c_{GM}|^2 + b_1|A_{GM} - d_{GM}|^2)\chi_B H(-\phi(x))dx \\
&+ \int_\Omega (a_2|f - c_{WM}|^2 + b_2|A_{WM} - d_{WM}|^2)\chi_B H(\phi(x))H(l - \phi(x))dx \\
&+ \int_\Omega (a_3|f - c_{CSF}|^2 + b_3|A_{CSF} - d_{CSF}|^2)\chi_B H(\phi(x) - l)dx \\
&+ \mu_1 \int_\Omega |\nabla H(\phi)|\chi_B dx + \mu_2 \int_\Omega |\nabla H(\phi - l)|\chi_B dx \,,
\end{aligned}
$$

where d_{GM}, d_{WM}, and d_{CSF} are the known average intensity values of the atlas channels for GM, WM, and CSF, respectively, obtained only from the non-zero values of each channel. The above energy is minimized if in the detected GM region we have both $f \approx c_{GM}$ and $A_{GM} \approx d_{GM}$ (similarly for WM and CSF). Coefficients a_i and b_i are used to weight the influence from the data and from the atlas. In our experiments, this model gives similar or improved results with our previous model without atlas prior. However, when necessary, weights b_i can be chosen larger than a_i, so that more influence is given to the atlas. This may be necessary on MRI data with very poor resolution.

Minimizing the energy F_A alternately with respect to the unknowns yields the associated Euler–Lagrange equations, parameterizing the descent direction by an
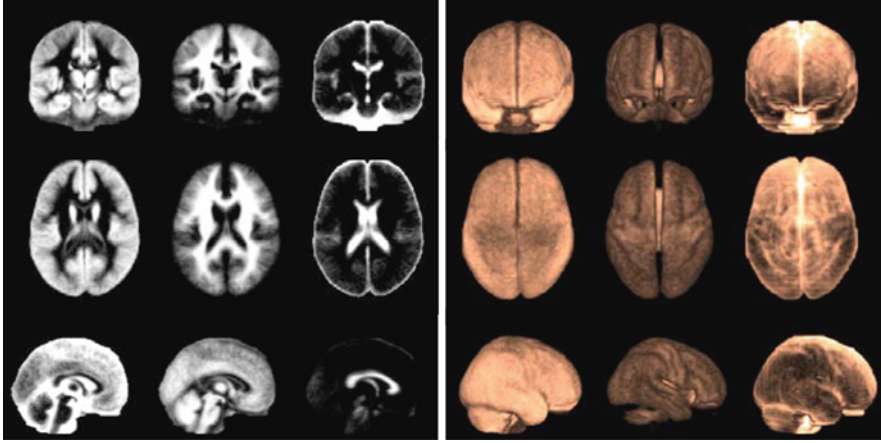
Fig. 2.1 2D (*left*) and 3D (*right*) views of brain MRI atlas spatial information (gray matter, white matter, cerebrospinal fluid; coronal, axial, and sagittal)

artificial time $t \geq 0$. The unknown constants, c_{GM}, c_{WM}, and c_{CSF}, are the same as in the case of the multilayer model without atlas. The time evolution equation for ϕ becomes

$$
\begin{aligned}
\frac{\partial \phi}{\partial t} = \delta(\phi) &\left[(a_1|f - c_{GM}|^2 + b_1|A_{GM} - d_{GM}|^2)\chi_B - \left(a_2|f - c_{WM}|^2 \right.\right. \\
&\left. + b_2|A_{WM} - d_{WM}|^2 \right) \chi_B H(l - \phi) \right] + \delta(\phi - l)\left[\left(a_2|f - c_{WM}|^2 \right.\right. \\
&\left.\left. + b_2|A_{WM} - d_{WM}|^2 \right) \chi_B H(\phi) - (a_3|f - c_{CSF}|^2 + b_3|A_{CSF} - d_{CSF}|^2)\chi_B \right] \\
&+ \mu_1 \delta(\phi)\mathrm{div}\left(\chi_B \frac{\nabla \phi}{|\nabla \phi|} \right) + \mu_2 \delta(\phi - l)\mathrm{div}\left(\chi_B \frac{\nabla \phi}{|\nabla \phi|} \right),
\end{aligned}
$$

which is discretized and solved using finite differences and fixed-point iteration.

3 Experimental Results and Comparisons

In this section we show experimental results for MRI brain segmentation with the proposed multilayer models with and without atlas information. We also compare these results with automated partial volume correction method (PVC algorithm provided by Center for Computational Biology, UCLA) and manual segmentation. The methods and comparisons were applied on nine data sets.

Data. Nine young adult normal control volunteers (mean age 24 years; five men, four women) were scanned using a gradient-echo (SPGR) T1-weighted protocol.

Data pre-processing. Volume data sets were subjected to the following pre-processing analyses: re-slicing the volume into a standard orientation, 3D digital

filtering to reduce inhomogeneity artifacts [19], tissue segmentation into brain and non-brain regions using semi-automated algorithms [10] for skull-stripping (these cannot be directly used for brain region segmentation), and finally scaling into a standard space. The data was aligned in Talairach space using six-parameter rigid body registration, AIR [26], followed by a nearest-neighbor interpolation for re-slicing the transformed volumes in Talairach coordinates [21]. Signal intensity nonuniformities caused by inhomogeneities in the scanner may result in poor tissue classification in different spatial regions of an imaged volume. Thus a 3D spatial filter was applied to each data set to remove low-frequency changes or "drifts" in signal value across the volume [19].

"Manual" tissue segmentation ("gold standard" or "ground truth"). Semi-automated tissue segmentation was obtained for all nine subjects' MRI volumes to classify voxels as gray matter, white matter, or cerebrospinal fluid based on signal value. Non-brain tissue and cerebellar structures were excluded before the tissue classification process. Trained neuroanatomists tagged samples of gray matter (40 voxels), white matter (40 voxels), ventricular cerebrospinal fluid (20 voxels), and background (20 voxels) throughout the volume of each re-sliced data set. These samples were used as training sets in a tissue classification algorithm that assigned each voxel to one of the four categories. A minimum distance classifier was chosen for this study because it provided the best results (for this T1-weighted imaging protocol) in a qualitative analysis of the different methods [20]. Although we call the segmented data obtained in this way "ground truth," we recognize that this depends on how the seeds were classified and on the semi-automated method. We mention that these "manual segmentation" results were not used as a prior or as an initial guess in our multilayer level set segmentation.

Probabilistic atlas. The ICBM-305 average and probabilistic brain atlases [12] were used to provide probabilistic restrictions for the evolution of the level set function. The ICBM atlas has a deterministic component that represents the "average" brain and a probabilistic component that contains probability maps for the likelihood that each voxel is part of any region of interest. These probability maps are used in our method with prior to penalize level set evolution outside the "common" brain.

Performance measures. To measure the performance of the segmentation methods, we use the standard concepts of sensitivity and specificity defined as

[Sensitivity = TP/(TP+FN), TP = True positives, FN = False negatives]
[Specificity = TN/(FP+TN), TN = True negatives, FP = False positives].

Numerical results. We first show in Fig. 2.2 2D views of the obtained 3D segmentations for visual comparison with the manual segmentation and with the PVC segmentation; thus we show the data, the manual segmentation, the PVC segmentation, the multilayer segmentation without prior, and the multilayer segmentation with prior applied to two of the nine data sets (note that for the manual result b and the PVC result c, the intensity values are artificial colors, while for the multilayer segmentation results d and e, the intensity values are the computed averages of the data on each anatomical region).
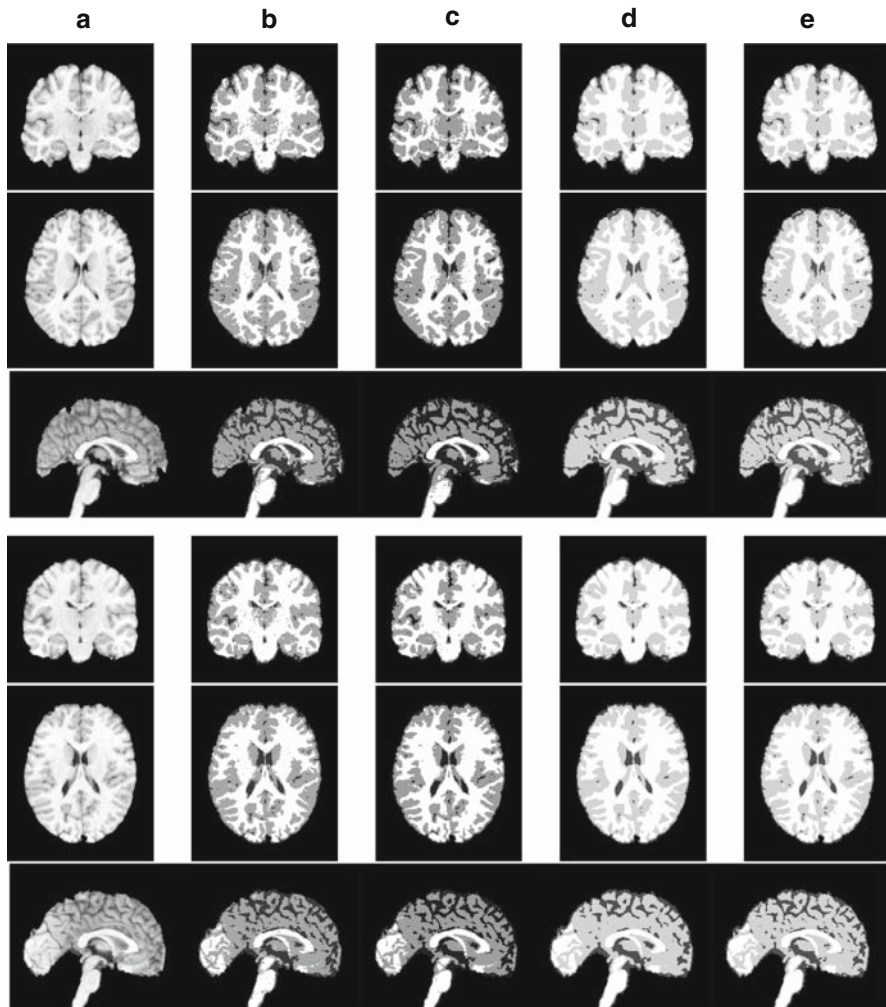
Fig. 2.2 Data sets 1 and 2.(**a**) Original; (**b**) ground truth; (**c**) PVC segmentation; (**d**) multilayer segmentation without prior; (**e**) multilayer segmentation with atlas prior

In Fig. 2.3, we show 2D results and set differences for data set 1 and each anatomical structure independently (gray matter, white matter, cerebrospinal fluid) corresponding to the PVC results, multilayer model without prior, and multilayer model with prior. Respectively column a corresponds to ground truth; column b corresponds to PVC and column c corresponds to the set difference $|b - a|$; column d corresponds to multilayer model without prior and column e corresponds to the set difference $|d - a|$; column f corresponds to the multilayer model with prior and column g is the set difference $|f - a|$.
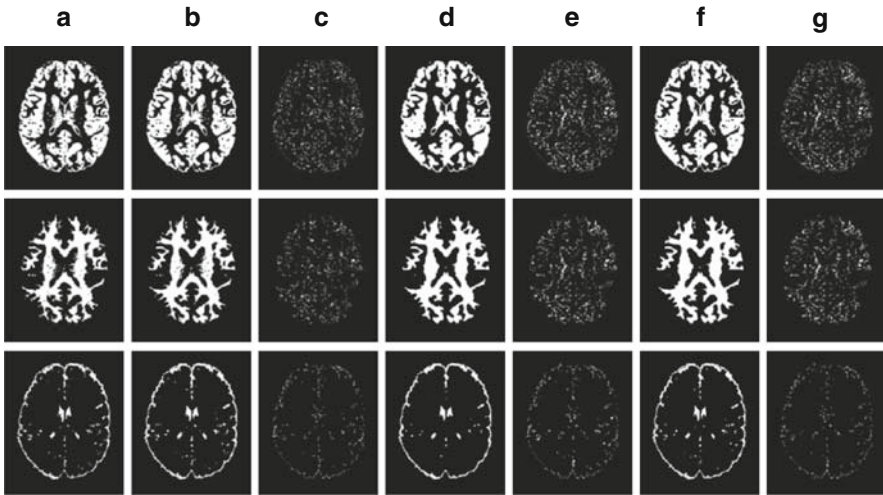
Fig. 2.3 GM (*top*), WM (*middle*), CSF (*bottom*) for data set 1. (**a**) Ground truth; (**b**) PVC result; (**c**) |**b** − **a**|; (**d**) multilayer result without prior; (**e**) |**d** − **a**|; (**f**) multilayer result with prior; (**g**) |**f** − **a**|

Table 2.1 Quantitative assessments for all nine data sets

Data	Measure	PVC			No prior			Prior		
		GM	WM	CSF	GM	WM	CSF	GM	WM	CSF
Data set 1	Sensitivity	0.93	0.91	0.96	0.90	0.94	0.90	0.90	0.94	0.92
	Specificity	0.93	0.97	0.97	0.93	0.93	0.98	0.93	0.94	0.98
Data set 2	Sensitivity	0.89	0.97	0.95	0.86	0.97	0.87	0.87	0.97	0.87
	Specificity	0.96	0.93	0.97	0.95	0.90	0.98	0.94	0.90	0.98
Data set 3	Sensitivity	0.92	0.95	0.94	0.90	0.94	0.90	0.88	0.96	0.87
	Specificity	0.95	0.96	0.98	0.93	0.93	0.98	0.93	0.93	0.98
Data set 4	Sensitivity	0.97	0.92	0.91	0.91	0.96	0.89	0.91	0.96	0.90
	Specificity	0.92	0.98	0.98	0.94	0.93	0.98	0.95	0.93	0.98
Data set 5	Sensitivity	0.95	0.92	0.93	0.92	0.89	0.86	0.93	0.88	0.91
	Specificity	0.92	0.97	0.98	0.88	0.95	0.98	0.89	0.96	0.98
Data set 6	Sensitivity	0.93	0.96	0.92	0.91	0.94	0.88	0.92	0.94	0.88
	Specificity	0.95	0.96	0.98	0.93	0.95	0.98	0.93	0.95	0.98
Data set 7	Sensitivity	0.92	0.97	0.89	0.90	0.96	0.89	0.90	0.96	0.89
	Specificity	0.95	0.95	0.98	0.94	0.93	0.98	0.94	0.93	0.99
Data set 8	Sensitivity	0.95	0.89	0.97	0.93	0.93	0.94	0.94	0.93	0.95
	Specificity	0.91	0.99	0.97	0.94	0.97	0.97	0.94	0.97	0.98
Data set 9	Sensitivity	0.91	0.94	0.97	0.79	0.98	0.89	0.81	0.97	0.91
	Specificity	0.95	0.96	0.97	0.95	0.87	0.98	0.95	0.88	0.98

Quantitative assessments and comparisons for all nine data sets are given in Table 2.1 and in Fig. 2.4. These show that in some cases, the proposed models give
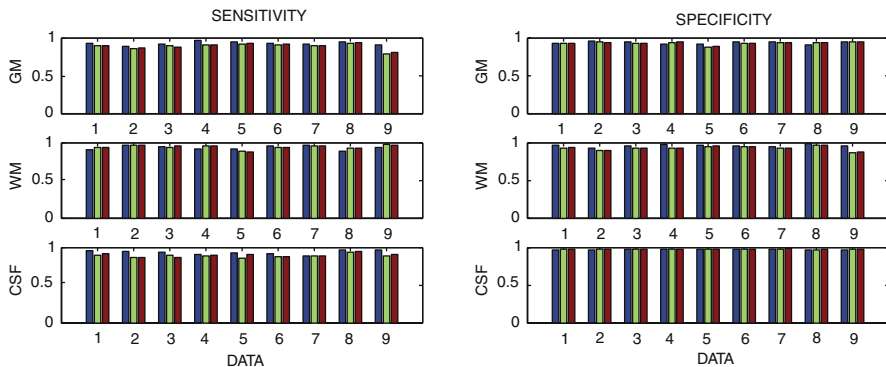
Fig. 2.4 Quantitative assessments for all nine data sets: sensitivity and specificity computed using the manual segmentation (ground truth) for PVC method (*blue*), multilayer model without atlas (*green*), multilayer model with atlas (*red*)

equal or superior results to PVC, and in most cases the results are only slightly inferior to the PVC results. The computational time for the proposed models is smaller than for PVC. In conclusion, we observe that our very simple proposed methods give satisfactory results, almost of the same quality as with the PVC method. Moreover, computational times are smaller using our proposed methods.

Figure 2.5 shows a visual comparison of reconstructed 3D average surfaces. Figure 2.6 shows a segmentation result, where more weight is given to the atlas.
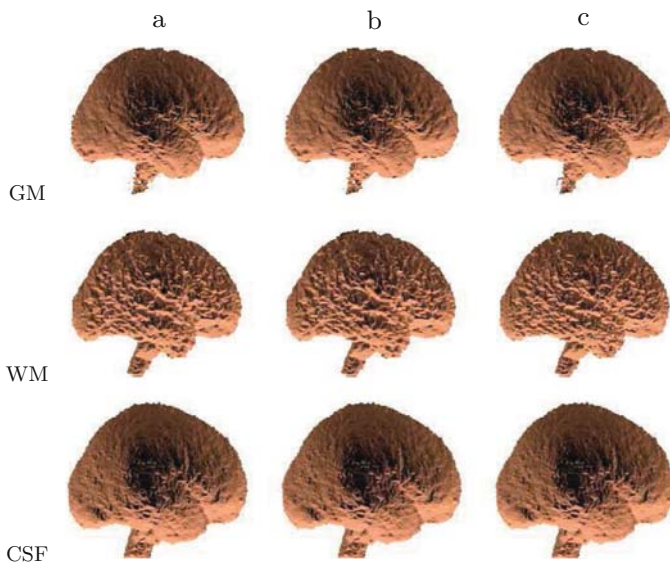

Fig. 2.5 Reconstructed average surfaces. (**a**) Multilayer segmentation with atlas information model, (**b**) multilayer segmentation without prior, (**c**) PVC segmentation

Finally, Fig. 2.7 shows the final level set contours (iso-levels 0 and l of final ϕ) for the data set 1, and Fig. 2.8 shows the numerical energy decrease versus iterations, validating the numerical stability of the algorithms.
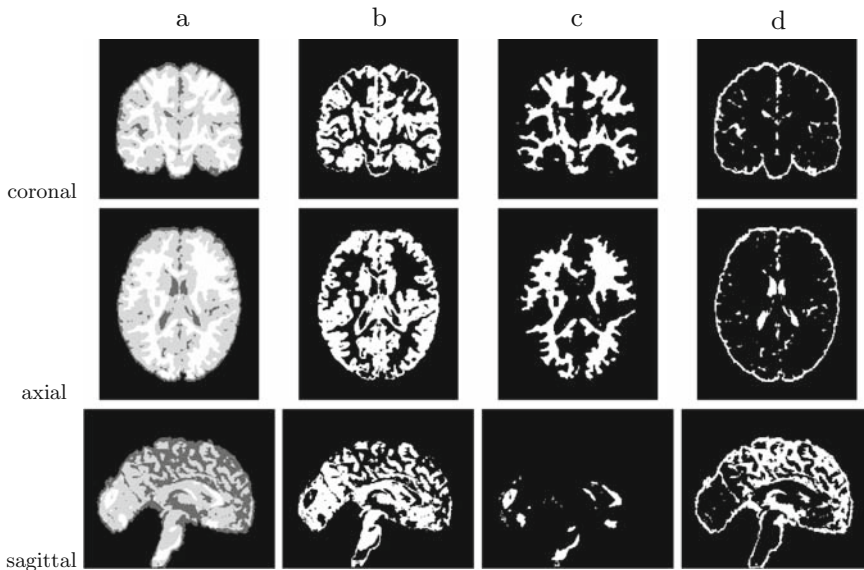

Fig. 2.6 (**a**) Experimental result obtained using the segmentation model with atlas, giving more weight to the atlas information; (**b**) GM; (**c**) WM; (**d**) CSF
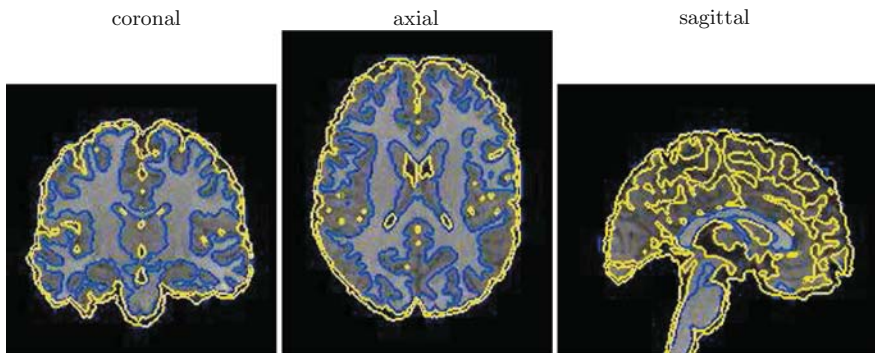

Fig. 2.7 Final detected contours with levels 0 and l for data set 1 using the multilayer segmentation model without prior
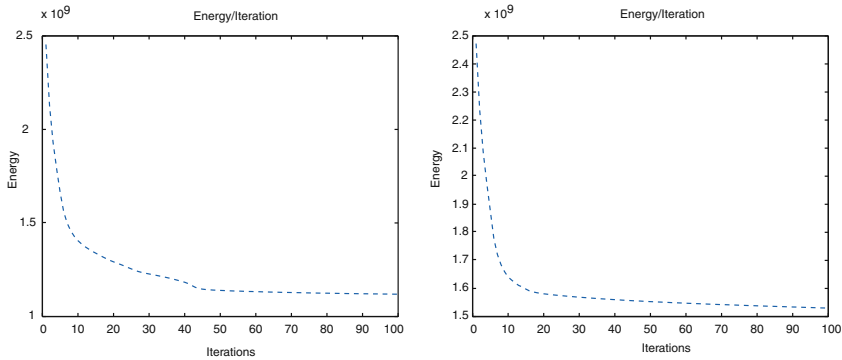
Fig. 2.8 Energy decrease versus iterations for the proposed multilayer segmentation models, validating the numerical stability of the algorithm: multilayer model without atlas (*left*), multilayer model with atlas (*right*)

References

1. Chan, T.F., Vese, L.: An active contour model without edges. LNCS, 1682, 141–151 (1999)
2. Chan, T.F., Vese, L.A.: Active contours without edges. IEEE Transactions on Image Processing, 10(2), 266–277 (2001)
3. Chung, G., Vese, L.A.: Energy minimization based segmentation and denoising using multilayer level set approach. LNCS, 3757, 439–455 (2005)
4. Chung, G., Vese, L.A.: Image segmentation using a multilayer level-set approach. Computing and Visualization in Science, 12(6), 267–285 (2009)
5. Chung, G., Dinov, I., Toga, A., Vese, L.A.: MRI tissue segmentation using a variational multilayer approach. UCLA C.A.M. Report 08-54 (2008)
6. Fischl, B., Salat, D.H., Busa, E., Albert, M., Dieterich, M., Haselgrove, C., van der Kouwe, A., Killiany, R., Kennedy, D., Klaveness, S., Montillo, A., Makris, N., Rosen, B., Dale, A.M.: Whole brain segmentation: automated labeling of neuroanatomical structures in the human brain. Neuron, 33, 341–355 (2002)
7. Han, X., Pham, D.L., Tosun, D., Rettmann, M.E., Xu, C., Prince, J.L.: CRUISE: cortical reconstruction using implicit surface evolution. NeuroImage, 23, 997–1012 (2004)
8. Hornak, J.: The basics of MRI, a hypertext book on magnetic resonance imaging, 1997, and A web resource on NMR spectroscopy. North East Regional Meeting of the American Chemical Society. Postdam, NY (1999)
9. Joshi, M., Cui, J., Doolittle, K., Joshi, S., Van Essen, D., Wang, L., Miller, M.: Brain segmentation and the generation of cortical surfaces. NeuroImage, 9(5), 461–476 (1999)
10. Kollokian, V.: Performance analysis of automatic techniques for tissue classification in magnetic resonance images of human brain. Master Thesis, Concordia University, CS Department, Montreal, Quebec, Canada (1996)
11. Liu, F., Gao, S., Gao, X.: Segmentation of MR images based on maximum a posterior. In: Proceedings of the 23rd Annual EMBS International Conference, Turkey (October 2001)
12. Mazziotta, J., Toga, A., Evans, A., Fox, P., Lancaster, J.: A probabilistic atlas of the human brain: theory and rationale for its development. NeuroImage, 2, 89–101 (1995)

13. Mumford, D., Shah, J.: Optimal approximation by piecewise smooth functions and associated variational problems. CPAM, 42, 577–685 (1989)
14. Osher, S., Sethian, J.A.: Fronts propagation with curvature dependent speed: algorithms based on Hamilton-Jacobi formulations. JCP, 79, 12–49 (1988)
15. Ratnanather, J.T., Priebe, C.E., Miller, M.I.: Semi-automated segmentation of cortical sub-volumes via hierarchical mixture modeling. Proceedings of the SPIE Medical Imaging 2003: Image Processing, 5032, 1602–1612 (2003)
16. Rohlfing, T., Brandt, R., Menzel, R., Russakoff, D.B., Maurer, C.R.: Quo Vadis, Atlas-based segmentation? In: Jasjit S. Suri, David L. Wilson, and Swamy Laxminarayan Handbook of biomedical image analysis, vol. 3. Registration models. Springer, New York (2005)
17. Rousset, O.G., Ma, Y., Evans, A.C.: Correction for partial volume effects in pet: principle and validation. Journal of Nuclear Medicine, 39(5), 904–911 (1998)
18. Rousson, M., Deriche, R.: Adaptive segmentation of vector-valued images. In: Osher, S., Paragios, N. (eds.) Geometric level set methods. Springer, New York, pp. 195–205 (2003)
19. Sled, J., Zijdenbos, A., Evans, A.: A nonparametric method for automatic correction of intensity nonuniformity in MRI data. IEEE Transactions on Medical Imaging, 17(1), 87–97 (1998)
20. Sowell, E.R., Thompson, P.M., Holmes, C.J., Batth, R., Jernigan, T.L., Toga, A.W.: Localizing age-related changes in brain structure between childhood and adolescence using statistical parametric mapping. NeuroImage, 9(6), 587–597 (1999)
21. Talairach, J., Tournoux, P.: Co-planar stereotaxic atlas of the human brain. Georg Thieme Verlag, New York (1988)
22. Tosun, D., Rettmann, M., Han, X., Tao, X., Xu, C., Resnick, S., Pham, D., Prince, J.: Cortical surface segmentation and mapping. NeuroImage, 23, S108–S118 (2004)
23. Tosun, D., Rettmann, M.E., Naiman, D.Q., Resnick, S.M., Kraut, M.A., Prince, J.L.: Cortical reconstruction using implicit surface evolution: accuracy and precision analysis. NeuroImage, 29(3), 838–852 (2006)
24. Tsai, A., Yezzi, A., Willsky, A.S.: Curve evolution implementation of the Mumford-Shah functional for image segmentation, denoising, interpolation, and magnification. IEEE Transactions on Image Processing, 10(8), 1169–1186 (2001)
25. Vese, L., Chan, T.: A multiphase level set framework for image segmentation using the Mumford and Shah model. International Journal of Computer Vision, 50(3), 271–293 (2002)
26. Woods, R., Grafton, S., Holmes, C., Cherry, S., Mazziotta, J.: Automated image registration: I. general methods and intrasubject, intramodality. Journal of Computer Assisted Tomography, 22(1), 139–152 (1998)
27. Zaidi, H., Ruest, T., Schoenahl, F., Montandon, M.: Comparative assessment of statistical brain MR image segmentation algorithms and their impact on partial volume correction in PET. NeuroImage, 32, 1591–1607 (2006)
28. Zhang, Y., Brady, M., Smith, S.: Segmentation of brain MR images through a hidden Markov random field model and the expectation-maximization algorithm. IEEE Transactions on Image Processing, 20(1), 45–57 (2001)

Chapter 3
Mapping Microcalcifications Between 2D Mammograms and 3D MRI Using a Biomechanical Model of the Breast

Vijay Rajagopal, Jae-Hoon Chung, Ralph P. Highnam, Ruth Warren, Poul M.F. Nielsen, and Martyn P. Nash

Abstract We propose a method to localise the 3D positions of microcalcifications found in X-ray mammograms using the 3D breast modelling framework of Chung et al. [1]. The accuracy of the method was first studied using a phantom embedded with X-ray visible beads. The phantom was subjected to mammographic-like compressions and imaged under X-ray to determine the positions of the beads. Using these data as inputs, the proposed modelling framework was used to predict the bead positions in the uncompressed phantom, which were also determined experimentally using bi-plane X-ray. The bead locations were reconstructed to within 2.8, 3.6 and 2.1 mm. The proposed method was demonstrated on a clinical case by successfully reconstructing the 3D positions of microcalcifications identified in X-ray mammograms and mapping them to a 3D MR data set of the same breast, demonstrating its potential to reliably track such features across different imaging modalities.

Keywords Finite Element Method · Biomechanical breast models

1 Introduction

While X-ray mammography is the primary imaging modality for early detection of breast cancer, it is common practice to acquire additional views of the breast using other modalities, such as magnetic resonance imaging (MRI) and ultrasound, during follow-up procedures to more reliably characterise suspicious lesions found in the mammograms. There is significant change in breast shape when acquiring the different images, from a compressed state during X-ray mammography to a pendulous shape when a patient lies prone for MRI. Compounded by the fact that mammograms are projections of a 3D object onto a 2D image, it is very challenging to reliably map information identified on a mammogram (such as the positions of microcalcifications) to other modalities or vice versa.

V. Rajagopal (✉)
Auckland Bioengineering Institute, The University of Auckland, Auckland, New Zealand
e-mail: v.rajagopal@auckland.ac.nz

Biomechanical modelling can enable clinicians to track information between imaging modalities by using predictions of breast deformation during different imaging procedures to map information from one image to another. One such application is in characterising the malignancy of microcalcifications. Microcalcifications cannot be seen in MRI. If microcalcifications are observed in X-ray mammograms, then the radiologist must decide whether they are benign or malignant. Co-location of microcalcifications with angiogenesis (visible in MRI) indicates a much greater probability of malignancy. In this chapter, we demonstrate the use of a customised biomechanical breast model based on the modelling framework of Chung et al. [1] in co-localising microcalcifications from craniocaudal (CC) and mediolateral-oblique (MLO) X-ray mammograms of a patient's breast and mapping this information to a 3D MR image set of the patient's breast.

While biomechanical models have been presented previously for this clinical application [2,3], they are limited by the assumptions that are made in order to simulate the complex nonlinear breast deformations during mammographic compression. Ruiter et al. applied displacement boundary constraints on model surface nodes to align the compressed breast model surface to the skin surface from the x-ray images. However, such modelling assumptions are inappropriate, because it is not possible to determine displacement of the skin within its tangent plane from the images, thus these models may overconstrain the in-plane motion of the skin. Zhang et al. use a step-wise incremental approach to solve the compression problem by applying Dirichlet boundary conditions on the compression plates and assuming that once model nodes come in contact with the compression plates they can only move in the direction of compression. The interaction between breast and rib surface was modelled as a fixed boundary by applying zero-displacement constraints on nodes that represented the back of the breast.

The novelty in using the Chung framework for this clinical application is that it is not necessary to make assumptions regarding the movement of the skin surface during compression. The framework only requires the initial and final positions of the compression plates to simulate the entire compressive deformation using contact mechanics theory. The simulations also permit the breast to slide across the pectoral muscle surface, which is more suitable than using a fixed, zero-displacement, boundary condition imposed in other models in the literature [4, 2, 5]. Further note that the modelling framework of Chung et al. has been quantitatively validated using controlled MR imaging experiments on silicon gel phantoms [6] (models predicted internal marker movement during mammography-like compressions to within 3 mm of the actual movement from MRI) and using clinical MR images of the breasts of volunteers (breast models predicted internal tissue movement in the range of 4–6 mm) [1]. This chapter presents the first quantitative validation of the reliability of the Chung modelling framework in co-locating microcalcifications in X-ray mammograms.

In the following sections, we first propose the process by which a biomechanical model can be used to track microcalcifications from 2D CC and MLO mammograms to the 3D uncompressed breast. The technique will then be illustrated in

two parts. The first part will describe a validation exercise that was conducted on a well-characterised silicon gel phantom to measure the accuracy of the proposed method in co-localising the 3D position of an internal mass from two X-ray images. The second part will show the performance of the validated technique in co-localising the 3D positions of microcalcifications found in a CC and an MLO image of a patient's breast.

2 Methods

2.1 The Modelling Framework

The modelling framework of Chung et al. uses the Galerkin finite element implementation of finite elasticity [7], coupled with the penalty method implementation of contact mechanics [8] to simulate breast compression, assuming frictionless contact between breast and plates. The contact virtual work is defined by

$$\delta W_c = - \int_{S_c^{(1)}} t_N \mathbf{n} [\delta \mathbf{u}^{(1)} - \mathbf{u}^{(2)}] dS_c^{(1)}, \tag{1}$$

where $\delta \mathbf{u}^{(1)}$ and $\delta \mathbf{u}^{(2)}$ are the virtual displacements associated with the slave (breast) and the master (compression plates), respectively. $dS_c^{(1)}$ is the contact surface of the slave and normal vectors, $\mathbf{n}$, are defined on the master surface. The frictionless contact force, t_N, is computed as

$$t_N = \begin{cases} \epsilon_N g_N & \text{if } g_N \geq 0 \\ 0 & \text{otherwise} \end{cases}, \tag{2}$$

where ϵ_N is the penalty parameter and g_N is the gap function (positive indicates penetration).

The interface between breast and rib surface is modelled using a modified version of frictional contact mechanics where the slip function is not computed (only stick condition is applied), but an elastic slip is modelled and varied by a stiffness parameter. The higher the elastic slip stiffness parameter, the greater the enforcement of the stick condition. The reader is directed to [9] for more details regarding the contact mechanics implementation.

Note that we assume the breast tissue to be ideally incompressible by introducing variables related to the intrinsic hydrostatic pressure, which are offset by additional kinematic constraints (in the Galerkin weak form) to maintain isochoric deformations [10].

2.2 Co-localisation of Microcalcifications

We use biomechanical models to co-localise the 3D positions of microcalcifications from a pair of CC and MLO mammograms, using the following steps illustrated in Fig. 3.1. The process starts with an individual-specific biomechanical model that has been created from 3D data of the breast shape, such as MRI, using techniques based on [11]. The steps are as follows:

1. Use a 3D biomechanical model to simulate the compressed configurations of the breast for each mammogram that is taken.
2. Generate 2D projections of the compressed models to provide skin contours (represented by the outer surfaces of the models) for the two mammographic views. The 2D projection is a superposition of a straight column of points perpendicular to the image plane.
3. Match the model contours to the mammograms (this involves rigid realignment of the model with the images).
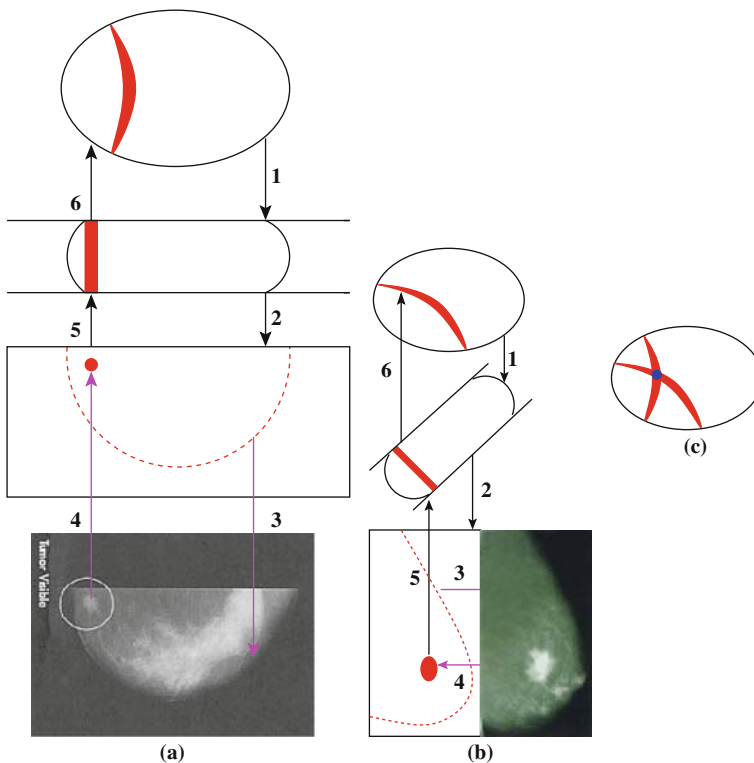
Fig. 3.1 Process of using a biomechanical model to localise the 3D position of a microcalcification identified in a pair of (**a**) CC and (**b**) MLO mammograms. Refer to text for explanation of each step

4. Transfer the locations of microcalcifications identified on the X-ray mammograms to the projections of the compressed models.
5. For each microcalcification, mark the associated 3D material points in the direction of the compression to form a tube of candidate points within the compressed breast model. A subset of the candidate points within each tube will be the 3D position of the microcalcification.
6. For each compressed model, track the tubes of candidate material points back to the common uncompressed breast model. Note that this only involves inverting the geometric transformation that was calculated in Step 1, so is not a non-tractable inverse problem.

The 3D position of a microcalcification corresponds to the location where the tracked tubes of candidate material points from the CC and MLO views intersect in the uncompressed model. Only true intersections (as opposed to also considering two tubes of points that are close to each other as intersections) were considered to identify the microcalcifications. Note that the performance of this process depends on the accuracy with which the model predicts the surface and internal tissue configurations of the breast in the two mammographic views.

3 Validation Using a Gel Phantom

The accuracy of the proposed method depends critically on the reliability of the biomechanical models to predict the mechanics of the breast. The breast consists of different types of tissue (skin, fibrous tissue, fat) and is subject to non-uniform loading and boundary conditions during compression, thus many model complexities must be accounted for to reliably model breast deformations. To estimate the achievable accuracy of the proposed method, we thus considered it better to perform initial experiments on a gel phantom that could be reliably represented. Note that the intention to use this phantom was not to precisely represent breast shape and deformations, but to be able to test and validate the methods using an object that could be reliably modelled.

A validation study was conducted to obtain a quantitative measure of the accuracy of the proposed method in localising the 3D position of objects found in a pair of X-rays taken from different compression directions (to mimic mammographic compressions). A phantom of known geometry (based on a custom-built mould shown in Fig. 3.2) was created using a two-component Sylgard 527 gel (Dow Corning). Four metal beads (visible under X-ray) were placed into the gel while it was curing. Due to the viscosity of the gel, the beads slowly sank towards the bottom of the mould, stopping once the gel solidified. Two X-ray images were taken of the gel phantom in the uncompressed state at 90° relative to each other (see Fig. 3.2). These images were used to calculate the 3D location of the metal beads inside the gel phantom.
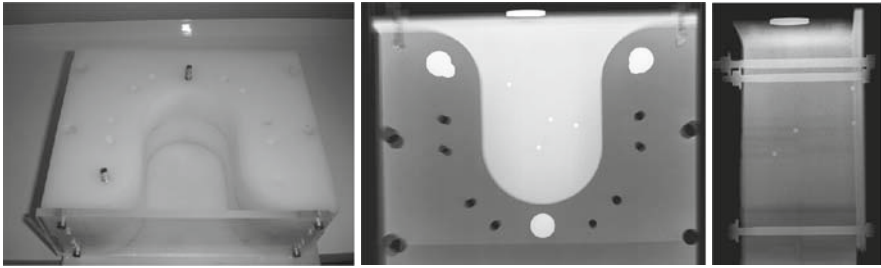
Fig. 3.2 The uncompressed gel phantom. *Left*: Custom-built teflon mould used to create gel phantom. *Middle*, *right*: Two X-ray images of the phantom in the mould showing the outline and metal beads (*bright spots*) embedded in the uncompressed phantom

Two compression loads (compressing by 37.5% of original thickness, similar to clinical mammography compression loads) were then applied to the phantom (using acrylic plates), during which it was X-ray imaged (see Fig. 3.3) in the direction of compression to mimic the mammography process. A biomechanical model of the uncompressed gel phantom was created (using prior knowledge of the mould geometry), describing it as a homogeneous material with the mechanical behaviour described by the neo-Hookean constitutive relation, $W = c_1(I_1 - 3)$. The constitutive
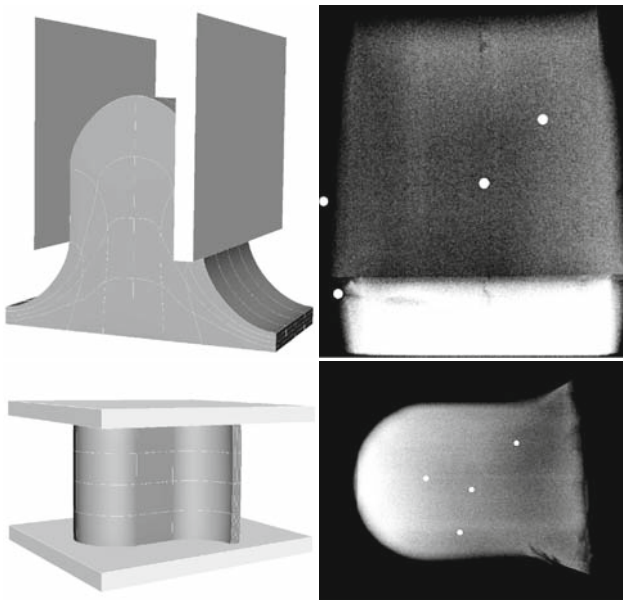
Fig. 3.3 The gel phantom in the two compressed states. Model and X-ray image pairs illustrating the CC-like (*top pair*) and ML-like (*bottom pair*) compressions that were applied to the gel phantom to image the metal beads embedded within the gel

parameter c_1 is related to the stiffness of the gel and I_1 is a measure of the strain in the gel (the first invariant of Lagrangian deformation tensor). The phantom was constructed in such a way that the base of the gel was firmly fixed to a base plate when curing was complete. To mimic this in the model, fixed displacement boundary conditions were applied at the base of the gel during CC-like compression. For ML-like compression, the gel was removed from the base plate and the fixed displacement constraints were removed. As shown in previous validation studies [6], such a biomechanical model of the gel phantom can reliably reproduce gel deformations, predicting surface shapes with root-mean-squared errors of less than 2 mm and predicting internal marker locations with errors of less than 3 mm.

The two X-ray images of the compressed phantom were then used with the biomechanical model to determine the 3D positions of the metal beads using the method proposed in this chapter. The predicted 3D locations of the metal beads were compared to their actual locations (determined from bi-plane images of the uncompressed phantom) to assess the performance of the proposed method. Only three out of the four beads were used in this validation study, because one bead sank to the base of the phantom which was outside the compressed region.

3.1 Results

Figure 3.4 shows the process of tracking the metal beads from the compressed to uncompressed configurations. The beads were displaced in the order of 12–15 mm during both compressions. The Euclidean distances between the experimentally estimated locations of the three beads and their corresponding model predicted locations (intersection points between CC and ML trajectories of material points) were 2.8, 3.6 and 2.1 mm.

4 Application to X-Ray Mammography

The proposed method was also tested in identifying the 3D location of microcalcifications found on a pair of CC and MLO mammograms of a patient's breast. MR images of the same breast were acquired with the patient lying in the prone position and were used to create a personalised biomechanical breast model (Fig. 3.5). Previous experience with mammography breast compression simulations [12] has shown that the effect of gravitational loads is negligible in comparison to the compression loads. Hence the model created from the prone MR image set was used as the uncompressed state before mammography compression was applied. The breast was assumed to be homogeneous and its mechanical behaviour was assumed to be characterised by the neo-Hookean constitutive relation (based on [11, 1]).

Following Chung et al. [1], the breast was assumed to slide along the surfaces of the pectoral muscles and ribs. Thus, the breast-to-rib interface and the interactions
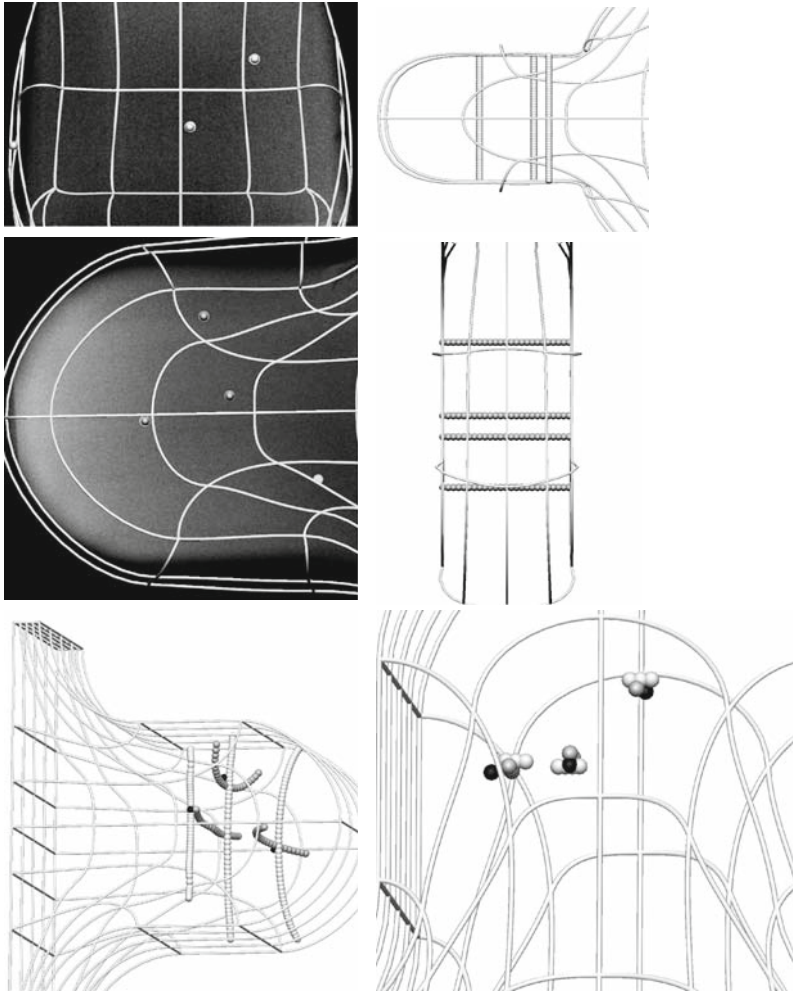
Fig. 3.4 3D localisation of metal beads in a gel phantom. The *top row* illustrates the process of transferring the bead locations from the images of the compressed phantom onto the biomechanical model, identifying all possible material points in the direction of CC-like projection (*left pair*) and ML-like projection (*right pair*). The *bottom row* shows the uncompressed geometry embedded with tracked tubes of candidate points, together with the actual 3D locations of the three metal beads (in *black*). The intersection between the tracked tubes of points are the predicted locations of the metal beads

of the breast with the compression plates were represented using contact mechanics constraints. The contact between these bodies was assumed to be frictionless. This is because of a lack of information on (and the difficulty of measuring) the amount of friction during the imaging procedure. The images were acquired in a clinic, independent of this study.
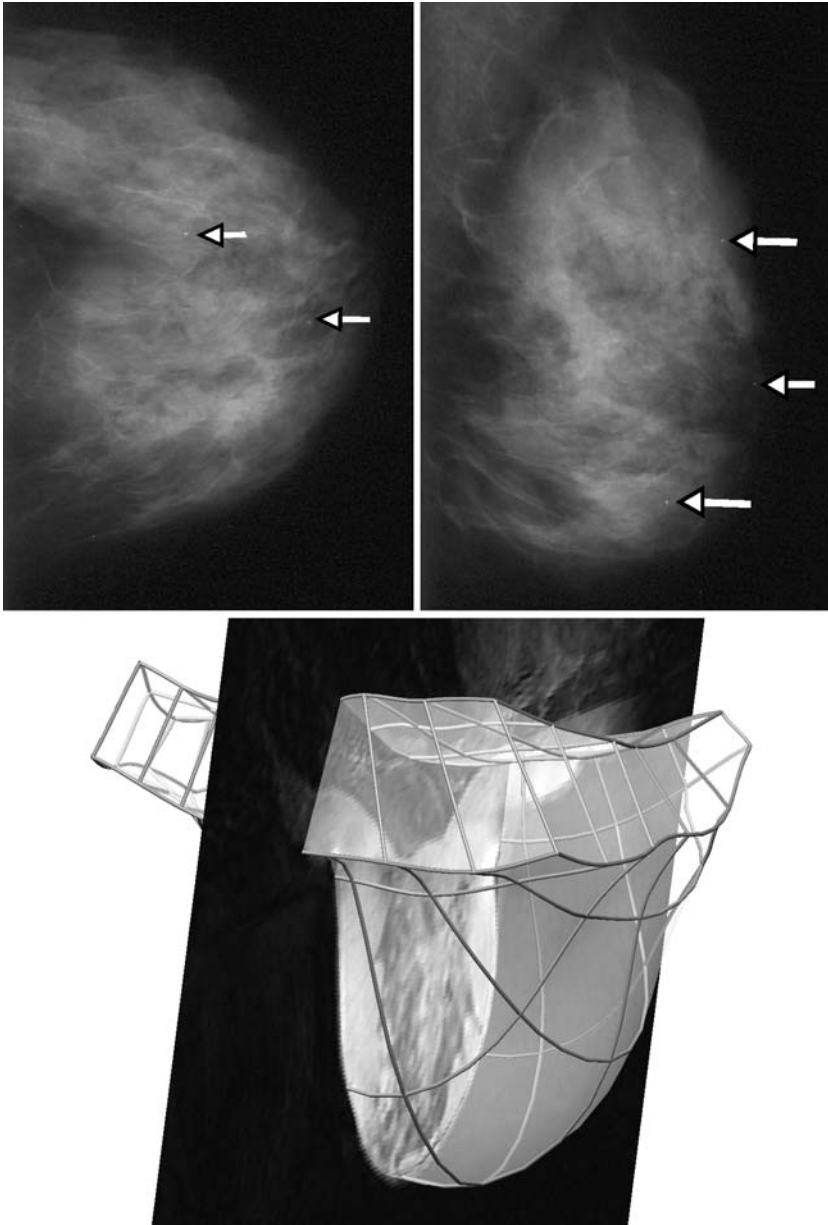
Fig. 3.5 Craniocaudal (*top left*) and mediolateral-oblique (*top right*) X-ray images of a patient's breast with *arrows* indicating microcalcifications that were tracked using the proposed method. A finite element model (*bottom*) of the same breast was fitted to 3D MR data

Breast deformations under CC and MLO compressions were simulated using the compression plate separation as the only input. Microcalcifications found in the CC and MLO images were tracked using the proposed method to the uncompressed configuration of the breast in order to determine the 3D location of the microcalcifications in the breast and to map this information to the 3D MR image set.

4.1 Results

Figure 3.6 illustrates the 3D localisation of the microcalcifications found in the CC and MLO images of the breast to the uncompressed 3D model and thus the MR image set. The two trajectories of material points from the CC view intersected with two out of the three trajectories in the MLO view, thus solving the problem of identity across the two views of the breast.

5 Discussion

Experiments using the gel phantom show that the proposed method can localise the 3D position of an object found in 2D X-ray to within 4 mm. Considering this result together with a demonstration of the method using a patient case study shows the potential of this technique in tracking microcalcifications across different medical images. Note that whilst it was not possible to quantitatively estimate the modelling accuracy for this patient study, the fact that the trajectories of material points from the CC and MLO images intersected for the two microcalcifications provides confidence in model predictions and tracking reliability in the clinical setting. The model could also be used to simulate other orientations of the breast in order to map the microcalcification positions to images from other modalities. For example, the model could map the microcalcification positions to ultrasound images by simulating the supine orientation of the breast.

Fig. 3.6 3D localisation of microcalcifications in a patient case study. *Top row*: The process of transferring microcalcifications found on the CC image onto the biomechanical model. *Second row*: The process of transferring microcalcifications found on the MLO image onto the biomechanical model. *Third row*: All possible material points are identified in the direction of the projections and these tubes of candidate material points are tracked to the uncompressed state. *Third row left*: The simulated MLO compression with the three tubes of material points from the MLO image (*black*) and the two tubes of points from the CC image (*silver*) that have been tracked to the uncompressed shape. Two of the three *black tubes* intersect with the two silver tubes, thus giving the positions of the two microcalcifications found in the CC image. *Third row right:* The 3D locations of the two identified microcalcifications (*black*) are tracked to the uncompressed state and superimposed on the MR image set (*bottom row*)
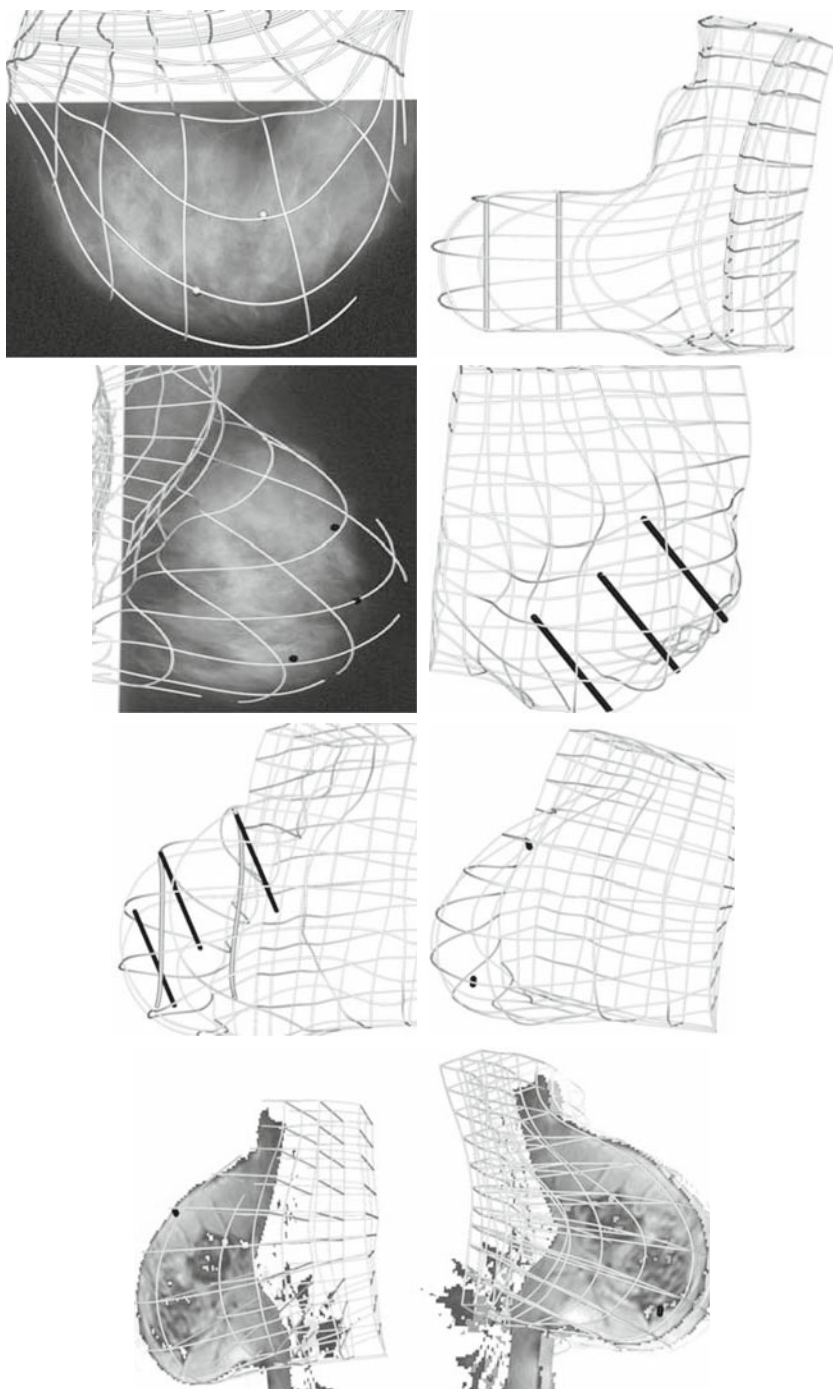
Fig. 3.6   (continued)

One of the main features that sets this modelling apart from previous studies is the fact that very few kinematic constraints were required to solve the compression problems because the problem was solved with contact mechanics theory. This overcomes the issue of incorrectly specifying motion of material points at the skin surface, as has been the case for some previously published models. Whilst the breast was assumed to be homogeneous and isotropic in this study, studies using larger numbers of clinical cases need to be conducted to quantify any improvements in prediction accuracy if a heterogeneous model were used.

This study has demonstrated the potential for biomechanical modelling to assist with breast image fusion by tracking microcalcification locations between CC and MLO images and also to a 3D MR image set. Reliably assimilating information from different imaging views and modalities into a common 3D visualisation environment will provide an additional tool to help clinicians increase the specificity and sensitivity of breast cancer detection.

References

1. Chung, J., Rajagopal, V., Nielsen, P., Nash, M.: Modelling mammographic compression of the breast. Lecture Notes in Computer Science, 5242, 758–765 (2008)
2. Zhang, Y., Qiu, Y., Goldgof, D., Sarkar, S., Li, L.: 3D finite element modeling of nonrigid breast deformation for feature registration in X-ray and MR images. In: Proceedings of the Eigth IEEE Workshop on Applications of Computer Vision, IEEE, p.38 (2007)
3. Ruiter, N., Stotzka, R.: Model-based registration of X-ray mammograms and MR images of the female breast. IEEE Transactions on Nuclear Science, 53, 204–211 (2006)
4. Pathmanathan, P., Gavaghan, D., Whitely, J., Chapman, S., Brady, J.: Predicting tumor location by modelling the deformation of the breast. IEEE Transactions on Biomedical Engineering, 55, 2471–2480 (2008)
5. Samani, A., Bishop, J., Yaffe, M., Plewes, D.: Biomechanical 3D finite element modeling of the human breast using MRI data. IEEE Transactions on Medical Imaging, 20, 271–279 (2001)
6. Chung, J., Rajagopal, V., Nielsen, P., Nash, M.: A biomechanical model of mammographic compressions. Biomechanics and Modeling in Mechanobiology, 7, 43–52 (2008)
7. Zienkiewicz, O., Taylor, R.: The finite element method: solid mechanics, 5 Ed, Vol. 2. Butterworth-Heinemann, Oxford (2000)
8. Laursen, T.: Computational contact and impact mechanics. Springer, Berlin (2002)
9. Chung, J., Rajagopal, V., Laursen, T., Nielsen, P., Nash, M.: Frictional contact mechanics methods for soft materials: application to tracking breast cancers. Journal of Biomechanics, 41, 69–77 (2008)
10. Malvern, L.: Introduction to the mechanics of a continuous medium. Prentice-Hall, Englewood cliffs, NJ (1969)
11. Rajagopal, V., Lee, A., Chung, J., Warren, R., Highnam, R., Nash, M., Nielsen, P.: Creating individual-specific biomechanical models of the breast for medical image analysis. Academic Radiology, 15, 1425–1436 (2008)
12. Chung, J.: Modelling mammographic mechanics. PhD thesis, University of Auckland (2007)

Chapter 4
Accuracy of Non-linear FE Modelling for Surgical Simulation: Study Using Soft Tissue Phantom

Jiajie Ma, Adam Wittek, Surya Singh, Grand Roman Joldes, Toshikatsu Washio, Kiyoyuki Chinzei, and Karol Miller

Abstract In this chapter, we evaluated the accuracy of non-linear FE modelling in application to surgical simulation. We compared experiment and FE modelling of indentation of the soft tissue phantom. The evaluation was done in terms of soft tissue phantom deformation and the forces acting on the indenter. The soft tissue phantom deformation was measured by tracking 3D motions of X-ray opaque markers placed in the direct neighbourhood under the indenter with a custom-built bi-plane X-ray image intensifiers (XRII) system. The modelling of soft tissue phantom indentation was conducted using the ABAQUS/standard finite element solver. Specific constitutive properties of the soft tissue phantom determined through semi-confined uniaxial compression tests were used in the model. The model accurately predicted the indentation force–displacement relations and marker displacements. The agreement between modelling and experimental results verifies the reliability of our FE modelling techniques and confirms the predictive power of these techniques in surgical simulation.

Keywords Surgical simulation · Non-linear FE modeling · Accuracy · Soft tissue phantom · Bi-plane XRII system

1 Introduction

Development of surgical simulation systems requires accurate modelling of soft organs and their interactions with surgical instruments in typical surgical procedures such as needle insertion, incision and dissection. Phenomenological models and FE models are by far the most popular approaches commonly used in surgical simulation. Phenomenological models rely on fitting various functions to experimentally

J. Ma (✉)

Intelligent Systems for Medicine Laboratory, School of Mechanical Engineering, The University of Western Australia, Crawley-Perth 6009, WA, Australia
e-mail: majiajie@mech.uwa.edu.au

obtained force–displacement curves to model the interactions between the surgical instruments and soft tissue. For instance, phenomenological models have been utilized to simulate needle insertion into soft tissue in which the needle forces are described as functions of insertion depth and relative velocity between the needle and soft tissue [1–4]. Its application made it possible to build interactive simulators with real-time kinesthetic and visual feedback [4]. However, the results predicted by such models are valid only for the specific surgical instruments and boundary conditions of the organs used in the experiments from which the models were derived. This implies that their predictive power is very limited.

Applying appropriate methods of computational solid mechanics to predict the forces acting on surgical instruments and soft tissue deformation during surgery eliminates this drawback. In practice, FE method has been used for such predictions; see e.g. [5–9]. With notable exception of Wittek et al. [8], previous studies generally used linear FE procedures for surgical simulation. However, it should be noted that the key assumptions of linear elasticity regarding the infinitesimally small deformations and linear stress–strain relations of soft tissue are violated in a typical surgical procedure. This is because the surgical procedures generally induce large local deformation and can lead to rigid body motion of the entire organ [7–9]. Moreover, it is well documented that soft tissues typically exhibit distinct non-linear constitutive behaviour [10–18]. Therefore, in surgical simulations, non-linear FE procedures that take into account both geometric (i.e. finite deformations) and constitutive non-linearities must be used.

Non-linear FE procedures implemented in the commercial finite element code LS-DYNA have been used by Wittek et al. [8] to predict the instrument forces and soft tissue deformations during needle insertion and indentation into the swine brain. However, the modelled force was approximately 25% larger in indentation and approximately 30% lower in needle insertion compared to the experimental measurement. These inaccuracies can be attributed to the fact that when modelling such complex phenomenon as indentation or needle insertion in the actual organs, it is very difficult to distinguish between the inaccuracies due to numerical techniques used (e.g. the reliability of finite element models degenerates when the elements become severely distorted due to large deformations) and modelling uncertainties regarding soft tissue properties and boundary conditions of organs. Generic properties are not sufficient for patient-specific computations in surgery simulations because of large variability inherent to biotissue [17, 19]. Despite recent progress in elastography using ultrasound [20] and magnetic resonance [21, 22], commonly accepted methods of measuring patient-specific properties of the brain have not been established yet. Appropriate formulation of boundary conditions for an organ also poses significant challenges [9, 17]. For instance, there are very limited data about the mechanical properties of the brain meningeal layers and interaction between these layers that can be used to formulate boundary conditions for the brain.

Therefore, in this chapter, we propose to evaluate the reliability and accuracy of non-linear FE modelling in surgical simulation through its application in modelling of indentation of the soft tissue phantom. Replacing the actual organ with the soft tissue phantom allowed us to conduct experiments under accurately controlled

conditions and eliminate the uncertainties due to boundary conditions and the problems of determining patient-specific constitutive properties for the soft tissue. The evaluation of the FE model accuracy was conducted in terms of its ability to predict the forces acting on the surgical instrument (indenter) and the soft tissue phantom deformation due to these forces. Deformation within the soft tissue phantom was determined by tracking motions of implanted X-ray opaque markers. To facilitate the construction of this marker pattern, the soft tissue phantom was constructed layer by layer.

The subsequent sections of this chapter present the following topics: Section 2 describes the experiment setup and determination of the marker displacements. Section 3 deals with the non-linear FE modelling of soft tissue phantom indentation. Section 4 compares the experimental and modelling results. The discussion and conclusions are in Section 5.

2 Experiment

2.1 Soft Tissue Phantom Preparation

The cylindrical shape soft tissue phantom (see Fig. 4.1, height of 46 mm, diameter of 64 mm and layer thickness of 9 mm) was made of *Sylgard 527* A&B silicone gel (Dow Corning Silicones, Midland, MI, USA) which has been used to simulate mechanical response of brain tissue [23, 24] and to validate methods for the characterization of soft tissue properties [25]. X-ray opaque markers (steel beads with a diameter of 0.3 mm) were planted within the soft tissue phantom to capture the deformation. The markers were planted following a pattern designed to minimize
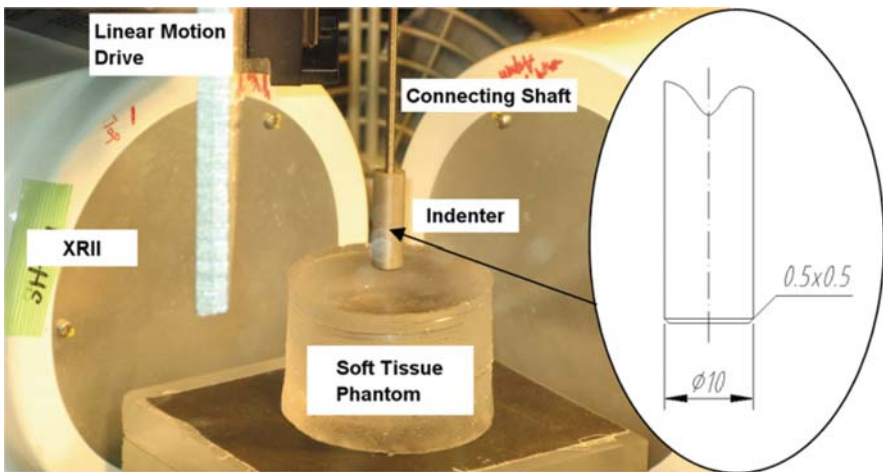
Fig. 4.1 Experiment setup of soft tissue phantom (height of 46 mm, diameter of 64 mm and layer thickness of 9 mm) indentation and indenter geometry

occlusion between markers during imaging while sufficiently covering the entire soft tissue phantom.

The *Sylgard 527* gel is prepared by mixing two parts (e.g. *Sylgard 527* A and B) at the ratio of 1:1. However, as only a small amount of gel was used for each layer, it is difficult to ensure this mixing ratio for every layer. Therefore, it was expected that different gel layers may exhibit different mechanical properties. To facilitate determination of the specific material constants for each layer, cylindrical samples (height of ∼24 mm and diameter of ∼30 mm) were made from the batches of gel used in the soft tissue phantom layers.

2.2 Experiment Apparatus

2.2.1 Experiment Setup

Indentations of the soft tissue phantom were performed using a custom-built apparatus consisting of a linear motion drive with a load cell and a stationary platform as illustrated in Fig. 4.1. The bottom surface of the soft tissue phantom was rigidly constrained to the stationary platform. The indenter was attached to the load cell by a connecting shaft. Only the forces acting in the longitudinal direction of the indenter were measured and analysed because the indenter was much stiffer than the soft tissue phantom and no indenter or shaft deflection was observed in the experiment.

As illustrated in Fig. 4.1, solid cylindrical aluminium indenter with a diameter of 10 mm and chamfer of 0.5×0.5 mm was used. The indentation speed was kept constant at 1 mm/s and the maximum indentation depth (the indenter displacement measured from the start of contact between the indenter and soft tissue phantom until the indenter reaches the farthest point of indentation) was approximately 10 mm. The displacement of the indenter was measured by a laser range scanner. The indentation forces and indenter displacement were acquired at a sampling rate of 30 Hz.

2.2.2 Bi-plane X-Ray Image Intensifiers System for Motion Tracking

Figure 4.2 shows the custom-built bi-plane X-ray image intensifiers (XRII) system used to track the motions of the X-ray opaque markers planted within the soft tissue phantom. It consists of two sets of X-ray sources and X-ray image intensifiers (type E5881J-P1, Toshiba Electron Tubes & Devices, Otawara, Japan) and an imaging acquisition unit (National Instruments, Austin, TX, USA). The two XRIIs were positioned so that their imaging planes were orthogonal to each other, allowing synchronized bi-plane real-time imaging of the marker and indenter motions during indentation experiments. The X-ray images were captured by the image acquisition unit at 30 frames per second and a resolution of 640×480 pixels.

We performed calibration and distortion correction to the X-ray images. The distortion model was adapted from Gronenschild [26, 27]. We found that the spiral distortion is negligible in our images, therefore it is not included in the distortion
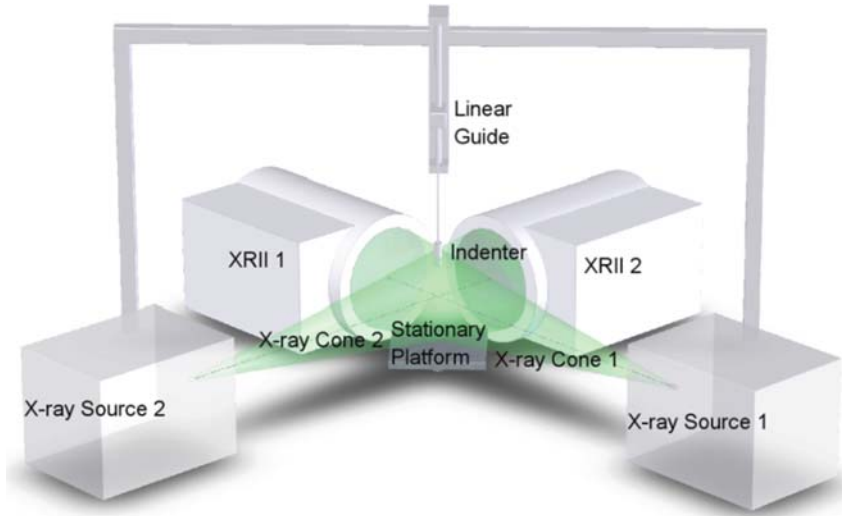
Fig. 4.2 Setup of the custom-built bi-plane XRII system

model. Following Navab et al. and Mitschke et al. [28, 29], the projection geometry of the XRII was approximated by a pinhole camera model. After distortion correction and calibration, the maximum inaccuracy of determining the 3D position of an object point from the X-ray images was determined to be 2.1 and 1.2 pixels in the left and right views, respectively.

The marker motions were tracked along the X-ray image sequence with an in-house code implemented in Matlab (The Math Works, Natick, MA, USA). We incorporated functions of the Camera Calibration Toolbox for Matlab [30] to remove the image distortions according to the estimated distortion coefficients. The positions of the markers were extracted from the images using phase congruency corner detector [31, 32]. Our tracking code determines the positions of the markers up to a sub-pixel level by fitting parabolae to the neighbourhoods of the markers. To evaluate the uncertainty of the results obtained using our tracking code, we applied it to determine the marker positions in 50 image frames in which the markers were kept stationary. In such circumstances, the uncertainty induced by our tacking code (indicated by the standard deviation of determining a particular marker's positions) is negligible (under 0.01 pixels) compared to the uncertainty induced by distortion correction and calibration which is 2.1 and 1.2 pixels in the left and right views, respectively. Therefore the accuracy of determining marker positions from X-ray images mainly depends on the accuracy of calibration and distortion correction.

We used the triangulation functions of the Camera Calibration Toolbox for Matlab [16] to compute the 3D positions of the markers from their positions in two perpendicular views determined by our tracking code. From the accuracy of calibration and distortion correction, the maximum uncertainty in determining the marker position was calculated at 0.36 mm.

2.3 Determining the Material Constants

Miller and Chinzei [16] used Ogden-type hyperviscoelastic material model to describe the constitutive behaviour of very soft tissue. However, as we found that the *Sylgard 527* gel does not exhibit significant strain-rate dependency at low strain rate used in this study, the Ogden-type hyperelastic constitutive law was used [33].

$$W = \frac{2\mu}{\alpha^2} \left(\lambda_1^\alpha + \lambda_2^\alpha + \lambda_3^\alpha - 3 \right) \tag{1}$$

where W is a potential function, $\lambda_i S$ are principle stretches, μ is the relaxed shear modulus and α is a material coefficient. We noticed that small difference in the mixing ratio of the two parts could result in significant difference in the mechanical properties of the cured *Sylgard 527* gel. Therefore, the cylindrical samples made along with the layers were tested by semi-confined uniaxial compression to determine the specific material constants for the layers. In the tests, the top and bottom surfaces of the gel samples were rigidly constrained in horizontal direction to the surfaces of the supporting base and loading head as shown in Fig. 4.3. Following Morriss et al. [34], the specific material constants of the gel samples were determined by calibrating the model of the semi-confined uniaxial compression tests of the gel samples using ABAQUS (Providence, RI, USA) finite element solver. Figure 4.3 shows the typical average force–displacement relations obtained from experiment and the corresponding modelling results. The Ogden type hyperelastic material constants (Eq. 1) determined for the soft tissue phantom layers are listed in Table 4.1.
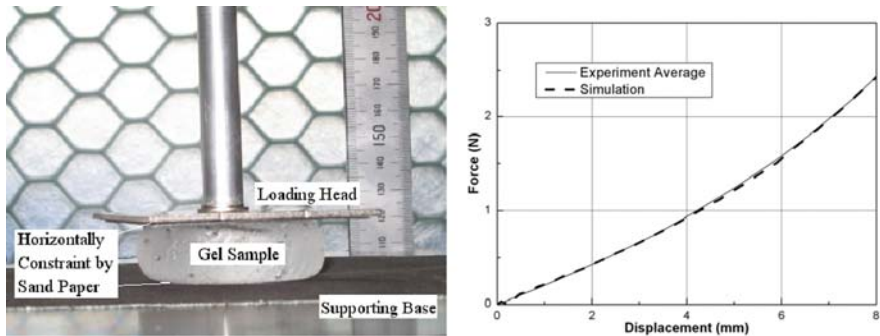
Fig. 4.3 The gel samples were tested by semi-confined uniaxial compression (*left*). The material constants were determined by calibrating the model of the compression test setup to the experiment average force–displacement relations using ABAQUS finite element solver

Table 4.1 Ogden type hyperelastic material constants for the layers of the soft tissue phantom determined by calibrating the model of the semi-confined uniaxial compression of the gel samples using ABAQUS finite element solver

Layer	$\mu(Pa)$	α
1	2,200	4.2
2	2,750	5
3	2,225	5.1
4	2,750	5
5	2,300	3

3 Modelling

3.1 Finite Element Mesh

The surface defining the geometry of the soft tissue phantom was generated by the Hypermesh (Altair Engineering, Troy, MI, USA) geometry builder module according to the measured dimensions of the soft tissue phantom. The volume taken by each layer was discretized by the Hypermesh automatic mesh generator with second-order tetrahedron elements (type C3D10H in ABAQUS, 10-node quadratic tetrahedron) [35]. These layers were assumed to be rigidly attached to each other because the *Sylgard 527* gel is very sticky. As the *Sylgard 527* gel used to simulate soft tissue in this study is almost incompressible, second-order elements with mixed formulation and constant pressure were selected to prevent volumetric locking [36, 37]. The resulting soft tissue phantom mesh consists of 13,995 nodes and 9,195 elements (Fig. 4.4).
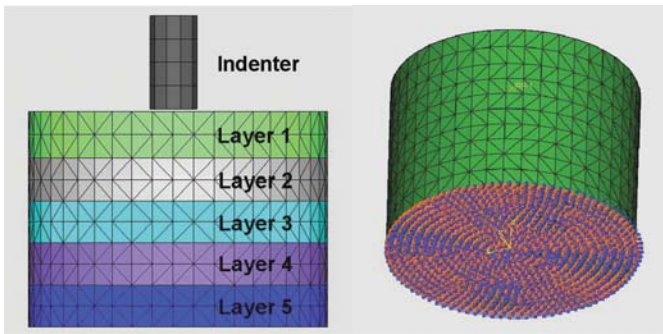
Fig. 4.4 Soft tissue phantom mesh (*left*). The nodes defining the *bottom* surface were rigidly constrained in the model (*right*)

As the aluminium indenter was orders of magnitude stiffer than the soft tissue phantom, it was modelled as a rigid body. Therefore, only the surface of the indenter was included in the model to define the contact with the soft tissue phantom. The indenter surface was discretized by 3-node and 4-node shell elements.

3.2 Contact Formulations, Loading and Boundary Conditions

When modelling needle insertion or indentation into soft organ, previous investigators typically rely on prescribing nodal displacements as the loading to their finite element models [7, 8]. Though it is a robust and straightforward approach, the contact interactions between the side surface of the needle/indenter and the soft tissues are not included. Therefore, to accurately model the interactions between the indenter and soft tissue phantom, we modelled the indentation as contact interactions between a rigid body (the indenter) and a deformable body (soft tissue phantom) using surface-to-surface penalty contact formulations with augmented Lagrange constraint enforcement. When conducting the indentation experiments, we noticed that the *Sylgard 527* gel sticks firmly to the indenter, therefore rough friction (no slip once points are in contact) conditions of ABAQUS were used.

The model was loaded by the motion of the indenter mesh. The loading speed was kept constant at 1 mm/s for 10 s which corresponded to the maximum indentation depth of approximately 10 mm.

In the experiment, the bottom surface of the soft tissue phantom was rigidly constrained by a sand paper glued to the stationary platform (Fig. 4.1). Therefore nodes defining this surface were rigidly constrained in the model (Fig. 4.4).

4 Results

For Ogden type hyperelastic material constants (Eq. 1) shown in Table 4.1, our finite element model accurately predicted the indentation force–displacement relations (Fig. 4.5) and marker displacements (Fig. 4.6). For indentation depth up to 10 mm, the error in indentation force magnitude was less than 5%. Comparison of marker displacement magnitudes at the indentation depth of 10 mm between our model predictions and experimental measurements is shown in Fig. 4.6a. Comparison of
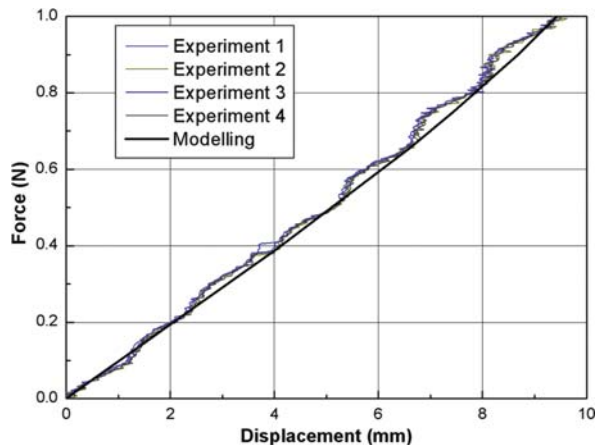
Fig. 4.5 Soft tissue phantom indentation: comparison of modelling and experimental results in force magnitude
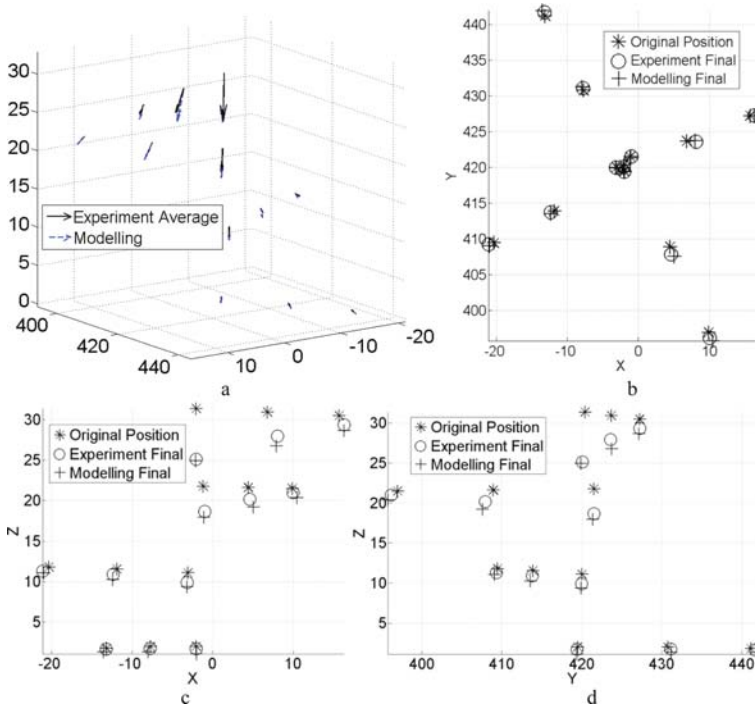
Fig. 4.6 Soft tissue phantom indentation: (**a**) comparison of predicted and measured marker displacements at the indentation depth of 10 mm. (**b–d**) Comparisons of the computed and experimental final positions of the markers at the indentation depth of 10 mm in *XY*, *XZ*, *YZ* plane. Original marker positions are included to indicate the magnitude of displacement

the final positions of the markers in *XY*, *YZ* and *XZ* planes at the same indentation depth are shown in Fig. 4.6b, c, d. Original marker positions are included to indicate the magnitude of displacements. The maximum, minimum and average of differences between the model prediction and experimental measurements in the *X*, *Y*, *Z* directions and the displacement magnitude are summarized in Table 4.2. The average difference was 0.32 mm, which is within the accuracy of determining

Table 4.2 The maximum, minimum and average of the *X*, *Y*, *Z* components and magnitude of the differences between the prediction of our model and the actual marker displacements obtained through experiment

Unit: mm	Maximum	Minimum	Average
Displacement in *X*-direction	0.16	0.01	0.08
Displacement in *Y*-direction	0.52	0.03	0.24
Displacement in *Z*-direction	0.96	0.23	0.48
Magnitude	0.84	0.06	0.47

Fig. 4.7 Soft tissue phantom indentation: the correlation of the predicted and measured magnitude of marker displacements magnitude. *Horizontal axis* – experimentally determined magnitude. *Vertical axis* – magnitude predicted by the model summarized in Fig. 4.4. The data points scatter along a 45° *line*, which indicates that the predicted and measured results are linearly correlated
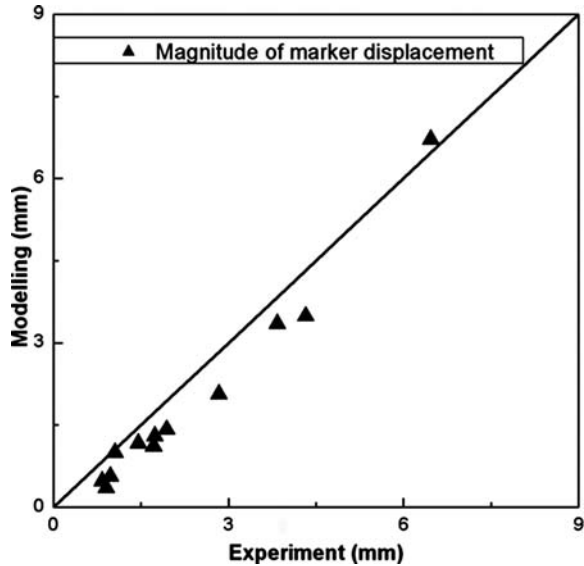
the marker displacements from the X-ray images (see Section 2.2.2). The correlation between the predicted and measured magnitude of the marker displacements is shown in Fig. 4.7. A very good agreement between the predicted and measured displacements is evident in this figure.

5 Discussion and Conclusions

In this chapter, we evaluated the accuracy of non-linear FE modelling in surgical simulation through its application in modelling of indentation of the soft tissue phantom. To distinguish between the inaccuracies due to the modelling techniques itself and modelling uncertainties regarding soft tissue properties and boundary conditions of an organ, we performed indentation experiments on the soft tissue phantom under accurately controlled conditions. To capture the deformations of the soft tissue phantom, we utilized image processing techniques to extract the displacements of the X-ray opaque markers placed in the soft tissue phantom from real-time X-ray images. To account for geometric and material non-linearities, we used non-linear finite element procedures with implicit time integration methods and Ogden type hyperelastic material model. The soft tissue phantom was made layer by layer and the material properties were determined by compressing cylindrical samples made from the same batch of gels used in the layers. The indentation was modelled as contact interactions between a rigid body (the indenter) and a deformable surface (soft tissue phantom). The finite element models accurately predicted the indentation forces (Fig. 4.5) and marker displacements (Fig. 4.6).

We hypothesize that the minor discrepancies between the modelling and experimental results observed here could be attributed to small inaccuracies when determining the phantom and marker pattern geometry. The phantom geometry, including thickness of the gel layers, was measured using a vernier caliper. As the *Sylgard 527* gel is very soft, we estimate that accuracy of these measurements is not better than 1 mm. The markers were manually placed by a tweezers with the reference to a template. Therefore, the accuracy of placing the markers is also less than 1 mm.

The modelling results demonstrate that for accurately controlled conditions and specific material constants, non-linear finite element models can accurately predict the forces acting on surgical instrument (indenter) and soft organ (simulated by the soft tissue phantom) deformation due to these forces despite the complexity of the analysed phenomena related to non-linear constitutive properties, contact interaction between the tool and organ, and very large local deformations of the organ. This confirms the predictive power of the non-linear finite element modelling techniques used in this study. Therefore, the results of this study suggest when conducting surgical simulation using non-linear finite element modelling, the main sources of error can be attributed to limited information about the boundary conditions for the organs and patient-specific constitutive properties rather than to the limitations of the finite element algorithms.

References

1. Simone, C., Okamura, A.M.: Modelling of needle insertion forces for robot-assisted percutaneous therapy. In: 2002 IEEE International Conference on Robotics and Automation, Washington, DC, pp. 2085–2091 (2002)
2. Okamura, A.M., Simone, C., O'Leary, M.D.: Force modelling for needle insertion into soft tissue. IEEE Transactions Biomedical Engineering, 51, 1707–1716 (2004)
3. DiMaio, S.P., Salcudean, S.E.: Needle insertion modelling and simulation. IEEE Transactions on Robotics and Automation, 19(5), 864–875 (2003)
4. DiMaio, S.P., Salcudean, S.E.: Needle steering and motion planning in soft tissues. IEEE Transactions of Biomedical Engineering, 52(6), 1167–1179 (2005)
5. Alterovitz, R., Goldberg, K., et al.: Needle insertion and radioactive seed implantation in human tissues: simulation and sensitivity analysis. In: 2003 IEEE International Conference on Robotics and Automation, Taipei, pp. 1793–1799 (2003)
6. Jordan, P.S., Socrate, S., et al.: Constitutive modelling of porcine liver in indentation using 3D ultrasound imaging. Journal of Mechanical Behaviour of Biomedical Materials, 2(2), 192–201 (2009)
7. Hing, J.T., Brooks, A.D., et al.: A biplanar fluoroscopic approach for the measurement, modelling, and simulation of needle and soft-tissue interaction. Medical Image Analysis, 11(1), 62–78 (2007)
8. Wittek, A., Dutta-Roy, T., et al.: Subject-specific non-linear biomechanical model of needle insertion into the brain. Computational Methods Biomechanical and Biomedical Engineering, 11(2), 135–146 (2008)
9. Wittek, A., Miller, K., et al.: Patient-specific model of brain deformation: Application to medical image registration. Journal of Biomechanics, 40(4), 919–929 (2008)
10. Fung, Y.C.: Biomechanics: Mechanical properties of living tissue. Springer, New York (1993)

11. Bilston, L., Liu, Z., et al.: Large strain behaviour of brain tissue in shear: some experimental data and differential constitutive model. Biorheology, 38, 335–345 (2001)
12. Farshad, M., et al.: Material characterization of the pig kidney in relation with the biomechanical analysis of renal trauma. Journal of Biomechanics, 32(4), 417–425 (1999)
13. Mendis, K., Stalnaker, R., et al.: A constitutive relationship for large deformation finite element modelling of brain tissue. Journal of Biomechanical Engineering, 117, 279–285 (1995)
14. Miller, K., Chinzei, K.: Constitutive modelling of brain tissue: experiment and theory. Journal of Biomechanics, 30(11/12), 1115–1121 (1997)
15. Miller, K., Chinzei, K., et al.: Mechanical properties of brain tissue in-vivo: experiment and computer simulation. Journal of Biomechanics, 33(11), 1369–1376 (2000)
16. Miller, K., Chinzei, K.: Mechanical properties of brain tissue in extension. Journal of Biomechanics, 35(4), 483–490 (2002)
17. Miller, K.: Biomechanics of Brain for Computer Integrated Surgery. Publishing House of Warsaw University of Technology, Warsaw (2002)
18. Miller, K.: Method of testing very soft biological tissues in compression. Journal of Biomechanics, 38(1), 153–158 (2005)
19. Miller, K., Wittek, A. et al.: Modelling brain deformations for computer-integrated neurosurgery. International Journal for Numerical Methods in Biomedical Engineering 26(1), 117–138
20. Salcudean, S., Turgay, E., et al.: Identifying the mechanical properties of tissue by ultrasound strain imaging. Ultrasound in Medicine and Biology, 32(2), 21–35, (2006)
21. Sinkus, R., et al.: Viscoelastic shear properties of in vivo breast lesions measured by MR elastography. Magnetic Resonance Imaging, 23, 159–165 (2005)
22. McCracken, J., et al.: Mechanical transient-based magnetic resonance elastography. Magnetic Resonance in Medicine, 53(3), 628–639 (2005)
23. Brands, D.W.A., Bovendeerd, P.H.M. et al.: The large strain dynamic behaviour of in-vitro porcine brain tissue and a silicone gel model material. Stapp Car Crash Journal, 44, 249–260 (2000)
24. Brands, D.W.A., Bovendeerd, P.H.M.: On the potential importance of non-linear viscoelastic material modelling for numerical prediction of brain tissue response: test and application. Stapp Car Crash Journal, 46, 103–121 (2002)
25. Augenstein, K.F., et al.: Method and apparatus for soft tissue material parameter estimation using tissue tagged Magnetic Resonance Imaging. Journal of Biomechanical Engineering, 127(1), 148–157 (2005)
26. Gronenschild, E.: The accuracy and reproducibility of a global method to correct for geometric image distortion in the X-ray imaging chain. Medical Physics, 24(12), 1875–1888 (1997)
27. Gronenschild, E.: Correction for geometric image distortion in the X-ray imaging chain: local technique versus global technique. Medical Physics, 26(12), 2602–2616 (1999)
28. Navab, N., Bani-Hashemi, A., et al.: 3D reconstruction from matrices in a C-arm based 3D-angiography system. In: The Proceedings of Medical Image Computing and Computer-Assisted Interventation – MICCAI, 1496, 119–129 (1998)
29. Mitschke, M., Navab, N.: Recovering the X-ray projection geometry for three dimensional tomographic reconstruction with additional sensors: attached camera versus external navigation system. Medical Image Analysis, 7(1), 65–78 (2003)
30. Bouguet, J.Y.: Documentation of a complete Camera Calibration Toolbox for Matlab. Available from: http://www.vision.caltech.edu/bouguetj/index.html (c1999–2008)
31. Kovesi, P.D.: Phase congruency: a low-level image invariant. Psychological Research, 64(2), 136–148 (2000)
32. Kovesi, P.D.: MATLAB functions for computer vision and image analysis. Available form: http://www.csse.uwa.edu.au/»pk/Research/MatlabFns/ (c1996–2007)

33. Ogden, R.W.: Large deformation isotropic elasticity – on the correlation of theory and experiment for incompressible rubberlike solids. In: Proceedings of the Royal Society of London. Series A, Mathematical and Physical Sciences, 326(1567), 565–584 (1972)
34. Morriss, L., Wittek, A., Miller, K.: Compression testing of very soft biological tissues using semi-confined configuration – a word of caution. Journal of Biomechanics. 41(1), 235–238 (2008)
35. ABAQUS: ABAQUS/Standard Manual, Version 6.7.1
36. Belytschko, T.: Overview of semi discretization and time integration procedures. In: Belytschko, T., Hughes, T.J.R. (eds.) Computational methods for transient analysis. Elsevier, Amsterdam, pp. 1–65 (1983)
37. Joldes, G., Wittek, A., Miller, K.: Non-locking tetrahedral finite element for surgical simulation. Communication in Numerical Methods in Engineering 25(7), 827–836 (2009)

Chapter 5
Patient-Specific Hemodynamic Analysis for Proximal Protection in Carotid Angioplasty

Harvey Ho, David Ladd, Andrew Holden, and Peter Hunter

Abstract Embolic protective devices (EPD) are used in carotid angioplasty to reduce or prevent embolic debris from entering the brain and causing procedure-related strokes. In this chapter we analyze a proximal protection mechanism of EPD that performs cerebral protection by external and common carotid artery occlusion. The mathematical model we use is a one-dimensional (1D) equation system governing blood flow. This system is applied to a patient-specific arterial tree constructed from a 3D computed tomography angiography (CTA) image. We simulate the blood flow in both normal and procedural conditions. Wherever possible we compare our computation results with laboratory or previously published measurements and our model agrees with these data.

Keywords Carotid angioplasty · Proximal protection · Hemodynamics · Modelling

1 Introduction

The carotid bifurcation is a vascular site where atherosclerotic stenoses are frequently found. Severe carotid stenosis leads to cerebral ischemia and may cause stroke. During the last two decades, carotid angioplasty and stenting (CAS) has emerged as an effective alternative to treat carotid stenosis besides carotid endarterectomy (CEA), especially for patients who are poor candidates for CEA [1–3]. The major drawback of CAS, however, is that manipulation of an atherosclerotic stenosis with guidewires, stents, and particularly angioplasty balloons can result in atheromatous debris embolizing and causing stroke. To alleviate this problem, some emboli protective devices (EPD) have been invented to prevent procedure-generated debris from migrating into the brain. Currently used EPD

H. Ho (✉)
Auckland Bioengineering Institute, The University of Auckland, Auckland, New Zealand
e-mail: harvey.ho@auckland.ac.nz

mechanisms include (1) distal balloon occlusion, (2) distal filter protection, and (3) proximal protection [2]. Each mechanism has its own strengths and weaknesses.

In this chapter we mainly study the proximal protection mechanism, which involves the occlusion of the common and external carotid artery (CCA, ECA) and development of reversed flow from cerebral arteries to internal carotid artery (ICA), so that any particles that are released during CAS will not flow to the brain. The typical proximal protection systems include the Parodi antiembolism system (PAES) [1] and the Mo.Ma device [2,3]. Both systems utilize two independently inflatable balloons, which are delivered to the CCA and ECA via a guiding catheter. The CCA and ECA are blocked after balloon inflation. The ICA, which has an open connection with intracranial arteries, acts as a conduit for the reversed flow which in turn flows through the hollow catheter. The difference between the two devices is that a continuous reversed flow is established in PAES via an arteriovenous shunt (Fig. 5.1c), while Mo.Ma uses intermittent or final aspiration to remove embolic debris [2].
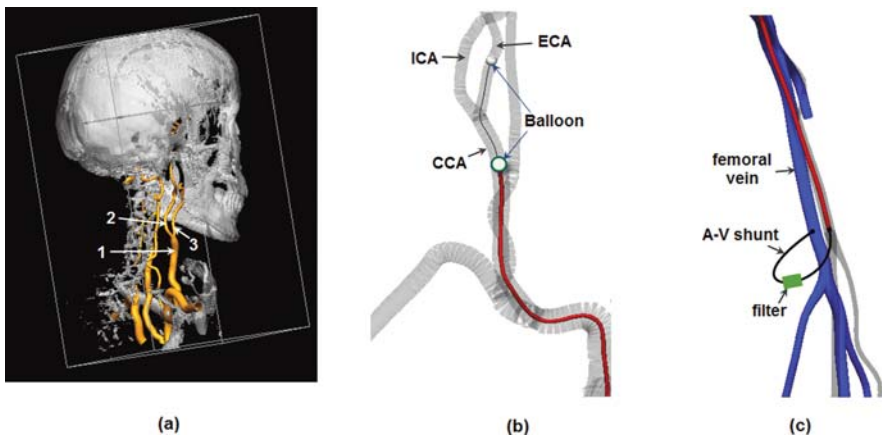
Fig. 5.1 Illustration of proximal protection: (**a**) the location of carotid arteries: 1-CCA, 2-ICA, 3-ECA; (**b**) two balloons are delivered to CCA and ECA, respectively, and (**c**) a shunt connects the catheter to the femoral vein (in PAES)

Since a carotid artery is temporarily blocked in this procedure and the brain is very sensitive to ischemia, it is extremely important to ensure the patency of the contralateral carotid artery. Another prerequisite of the procedure is a complete and functioning circle of Willis (CoW) [1]. Further preoperative considerations include (a) the patient's ability to tolerate the temporary interruption of brain perfusion during the intervention and (b) the impact of reversed flow on the cerebral circulation.

To address these considerations, we present a computational approach to predict the flow pattern variations in the carotid and cerebral arteries during this procedure. The model is based on a reduced formation of the governing equations for blood flow and is applied to a patient-specific arterial tree digitized from a 3D CTA

image. The pre-and post-processing tool used in this work is the open source imaging and visualization software CMGUI. The flow solver employed is a research code developed in-house.

2 Method

2.1 Vascular Model Construction

The CTA data used were of a male adult subject containing $421 \times 378 \times 336$ pixel slices (Fig. 5.2a). The spatial resolution of each image is $0.488 \times 0.488 \times 0.7$ mm. Using CMGUI we manually select 175 key points along the centerline of large blood vessels as *nodes*. The radius at each node is defined as a *field* for that particular node. These nodes are then connected by 1D cubic Hermite elements. A cylindrical approximation is used to represent the major arteries supplying blood to the brain. Figure 5.2 depicts the digitizing process.
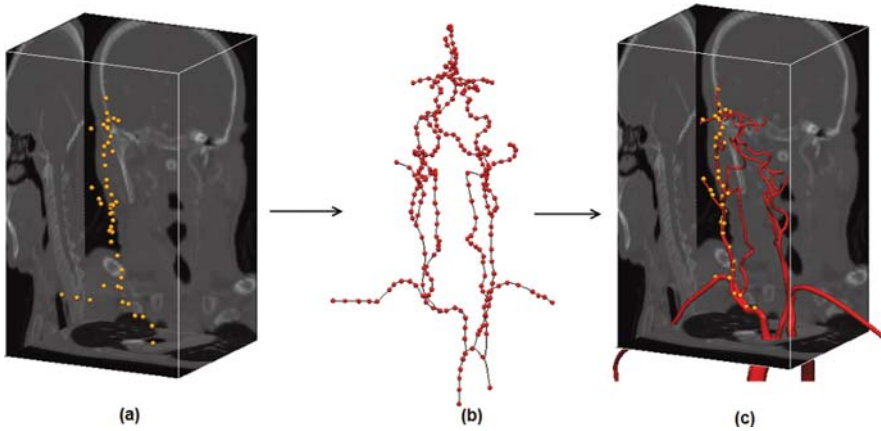
Fig. 5.2 Vascular tree construction pipeline: (**a**) node selection; (**b**) 1D elements construction; (**c**) cylinder simulation incorporating radius information

2.2 Hemodynamics Modeling

Governing equations In large arteries, the blood can be modeled as a Newtonian fluid [4–7]. We further assume that the flow in the circumferential direction is negligible and the radial velocity is small compared to axial velocity, the governing 1D system of blood flow can be written as follows [4]:

$$\frac{\partial R}{\partial t} + V \frac{\partial R}{\partial x} + \frac{R}{2} \frac{\partial V}{\partial x} = 0, \tag{1}$$

$$\frac{\partial V}{\partial t} + (2\alpha - 1)V\frac{\partial V}{\partial x} + 2(\alpha - 1)\frac{V^2}{R}\frac{\partial R}{\partial x} + \frac{1}{\rho}\frac{\partial P}{\partial x} = -2\frac{\upsilon\alpha}{\alpha - 1}\frac{V}{R^2}, \qquad (2)$$

$$P = \frac{2}{3}\frac{Eh_0}{R_0}(\frac{R^2}{R_0^2} - 1), \qquad (3)$$

where P, R, V, ρ, and υ represent pressure, inner vessel radius, velocity, blood density, and viscosity, respectively. The parameter α specifies axial velocity profile [4]. Equation (3) is the wall constitutive equation representing the relationship between the transmural pressure and vessel diameter where E, h_0, and R_0 are the Young's modulus, wall thickness, and unstressed radius, respectively [5].

When solving the governing equations, the density ρ and kinematic viscosity ν of the blood are set as $1.05\,\text{g/cm}^3$ and $3.2\,\text{cm}^2/\text{s}$, respectively. The data for arterial wall elasticity are adopted from [6] which takes the stiffness difference between intracranial and extracranial arteries into account.

Numerical methods: The nonlinear, hyperbolic system (1–3) is solved by a second-order MacCormack numerical scheme [8]. In this scheme, the predicted values of P,R,V are evaluated by a backward difference at first, and their "corrected" values are evaluated by a forward difference. This procedure is repeated at each time step.

The stability analysis dictates that the numerical speed must be faster than the wave speed of the equation [4]. Since the propagation speed of blood pressure in an elastic tube is about 5–10 m/s, for a spatial step of 1 mm, the time step should be 0.1–0.2 ms.

Bifurcation model: To model flow in an arterial tree, a bifurcation model is further incorporated. This model predicts pressure gradient, velocity, and flow distribution across vascular branches, thus in the whole arterial tree. We refer the interested reader to [4] for more mathematical details.

Boundary conditions: The initial velocity and pressure at all vessel segments are set as 0 mm/s and 10.6 kPa (80 mmHg). A physiological pulsatile pressure (80–120 mmHg) is prescribed from the inlet, i.e., the ascending aorta. For the treatment of outlets, we introduce the concept of *resistance segments* (RS) which are short and sharply tapering ($R_{\text{in}}/R_{\text{out}} \approx 2$) elastic tubes attached to individual outlets (per Fig. 5.3a.2, b.2). These segments are used to account for downstream vascular resistance. By prescribing a fixed 80 mmHg pressure to RS outlets, the pressure gradient between the inlet and RSs will drive the blood flow through the arterial tree.

3 Results

3.1 Normal Flow

Numerical simulation It took about 12 min to compute the flow in five cardiac cycles on a personal computer (1.73 GHz, 3 GB RAM, Intel Pentium Dual-Core) and the
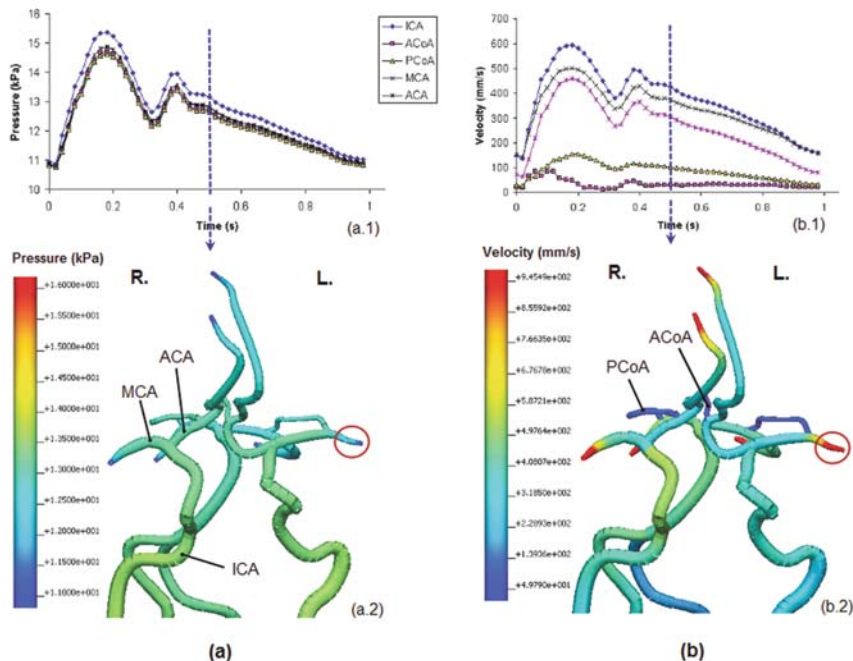
Fig. 5.3 (**a.1**) Pressure profiles of five sites during a cardiac cycle. Note that the mean pressure in ICA is higher since it is the afferent vessel of MCA and ACA; (**a.2**) visualization of the pressure distribution (at 0.5 s); (**b.1**) velocity profiles of the same five sites. Note that the flow in communicating arteries (ACoA and PCoA) is much lower than other cerebral arteries; (**b.2**) visualization of the velocity distribution (at 0.5 s) in arterial tree. The short tapering segment inside the *red circles* represents one of the resistance segments (RS)

flow data in the last cardiac cycle were analyzed. The computation results contain important flow information such as pressure, velocity, and flow rate at discrete points along the arterial tree. Figure. 5.3a,b shows the pressure and velocity distribution in the arteries from ICA to CoW. The pressure and velocity profiles at five typical sites (of arteries ICA, MCA, PCA, ACoA, and PCoA) during a cardiac cycle are shown in Fig. 5.3a.1, b.1, respectively.

Validation A LogicScan 128 ultrasound scanner (TELEMED Ltd., Lithuania) was used to detect the flow velocity at the inner carotid artery from a volunteer subject. The measured waveform, which varies between 55 and 310 mm/s during a cardiac cycle, is shown in Fig. 5.4a. The comparison indicates that the largest velocity (about 31–32 cm/s occurs at systole) of the simulation matches that of the ultrasound data. However, the simulation overestimates the flow velocity at diastole. The pressure waveform of the subclavian artery computed from the 1D model is compared with that measured by Mills et al. using an electronic transducer [9] (see Fig. 5.4b). The two pressure waveforms agree favorably with each other. Hence,
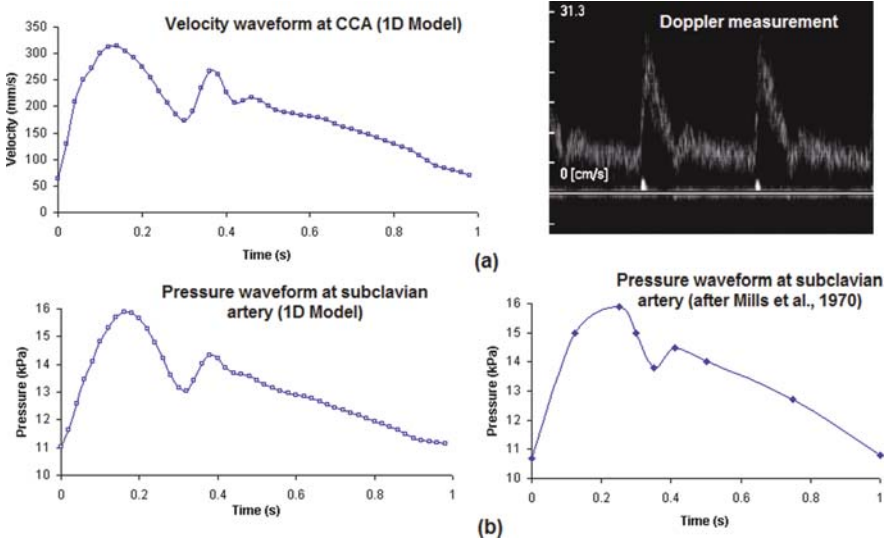
Fig. 5.4 (**a**) *Left*: velocity waveform of CCA from the 1D model; *right*: measurement from an ultrasonic scanner; (**b**) *left*: pressure waveform of subclavian artery from the 1D model; *right*: pressure waveform of subclavian artery after Mills et al. [9]

we consider that the overall simulation result is within the acceptable physiological range of in vivo ultrasonic measurement.

We also compare the computation results in the intracranial arteries with previously published data, e.g., in [6,7,10]. The measurement methods in these literature include non-invasive transcranial Doppler ultrasound [10] and validated computational fluid dynamics (CFD) analysis [6,7]. These data are tabulated in Table 5.1. The comparison indicates that the results from our model are within acceptable physiological ranges of in vivo measurements and also agree with the CFD analysis results published by some other research groups.

3.2 Flow in CAS with Proximal Protection

If we assume that PAES is performed for the right carotid artery and that the right CCA and ECA are occluded, then the corresponding modifications to the arterial tree configuration include (a) removing the right CCA and the right ECA from the arterial tree because there is no flow in them; (b) connecting a virtual catheter to the right ICA to act as a pathway for reversed flow (per Fig. 5.1c). Note that because the right CCA is occluded, the possible sources of blood supply to the reversed flow have to be from (a) the *left* carotid artery via the ACoA (per Fig. 5.4) and (b) the posterior cerebral arteries via posterior communication artery.

The initial conditions for reversed flow are set similarly as that used in normal flow, except the out boundary conditions for the right MCA and ACA (adjusted

Table 5.1 Comparison of unstressed radius (R, mm), flow rate (F, ml/s), and velocity (V, cm/s)

Name of artery	ICA			ACA			MCA			ACoA			PCoA		
	R	F	V	R	F	V	R	F	V	R	F	V	R	F	V
Alastruey et al. [5]	2.0	–	–	1.17	1.16	–	1.43	1.73	–	0.74	0.05	–	0.73	0.01	–
Long et al. [6]	2.36	–	–	1.2	–	–	1.46	–	–	0.58	0.097	–	0.72	0.42	–
Lindegaard et al. [7]	2.25	–	37	1.05	–	55	1.4	–	64	–	–	–	–	–	–
Our model	2.2	4.69	29.4	1.3	1.67	30.0	1.6	3.13	37.1	0.7	0.043	2.7	0.8	0.20	9.7
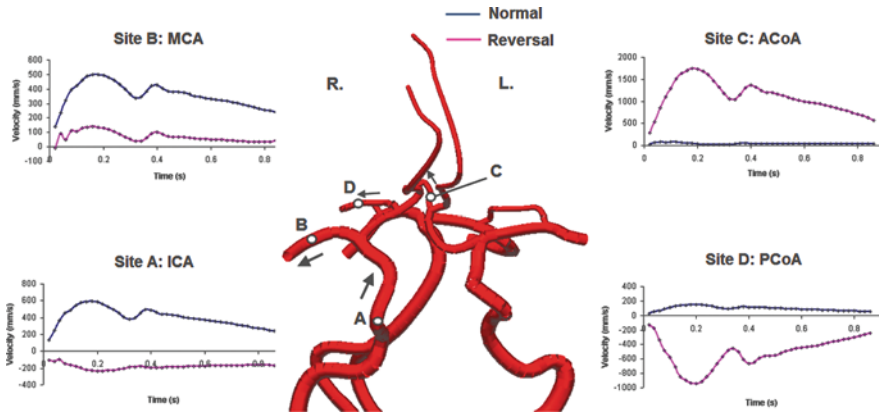
Fig. 5.5 Comparison of flow velocity at four typical sites in normal and reversed flow conditions. The *arrows* indicate positive flow, i.e., normal flow directions. **Site a**: flow in right ICA is reversed at a smaller velocity of average 185 mm/s; **Site b**: positive flow in MCA is still maintained albeit at a much lower velocity; **Site c**: flow at ACoA is drastically increased (from average 20 to 1,250 mm/s) to supply the reversed flow; **Site d**: flow at PCoA is not only reversed but also greatly increased (from average 100-minus to 620 mm/s to) supply reversed flow in the right ICA

to 72 mmHg) to account for the low pressure induced by the open catheter. The pressure profiles during a cardiac cycle at four typical sites, the right ICA, MCA, ACoA, and PCoA, are shown in Figure 5.5 (at Sites a–d). The results indicate that the flow in ACoA increases significantly (from average 20 to 1,200 mm/s) to supply the reversed flow (per Site c of Fig. 5.4). This sharp increase is expected since much of the flow feeding the reversal catheter will be contralateral via this communicating artery. The same phenomenon happens with the right PCoA where the flow is not only reversed but also largely increased (Site d in Fig. 5.4). The ratio between the supply from the ACoA and right PCoA is about 2:1. In other words, the main source for the reversed flow is from the other patent carotid artery.

4 Discussion

The objective of this work was to investigate the hemodynamic factors associated with the proximal embolic protection mechanism of EPD, which works by CCA and ECA occlusion to prevent embolic particles from flowing into the brain and causing stroke. Proximal protection devices have several advantages including non-traversal of the lesion until antegrade flow is ceased, and its potential to capture embolic particles of all sizes. The major problem of this procedure, however, is that possible patient intolerance may occur during the procedure due to cessation of antegrade flow and sometimes even flow reversal [1,3]. Hence, it is extremely important to understand and predict flow variations preoperatively. In this sense, a computational model can aid the process of blood distribution analysis.

In our numerical simulation of the PAES procedure, we found that the main supply to the reversed flow is from the ACoA. This echoes the conclusions made in other carotid stenosis studies, e.g., in [6,7]. We also found that due to the terminal connection with the arterio-venous shunt via ICA → catheter the supply to the ipsilateral MCA reduces substantially. Indeed, our model predicts a reversed flow in this artery at the initial moments of flow reversal. That is to say, the reversal flow channel "steals" blood from its upstream cerebral arteries. This can contribute to patients' intolerance which requires termination of the procedure [1]. However, once the reversed flow has become stable, the blood sources from both ACoA and PCoA can resupply the MCA (in a lower flow rate, per Fig. 5.5, Site **b**).

From computational mechanics' perspective, the authors are aware of possible sources of error in the presented model. The resistance segment (RS) technique is particularly useful in the presented model and attempts to incorporate the fundamental principle that most of the resistance in the system comes from vessels further downstream and which generally cannot feasibly be resolved by CTA or MRI. This technique still requires additional validation with currently used lumped parameter models and additional verification with clinical data. Inconsistencies in the velocity waveform as evident in Fig. 5.4a are also of interest and require further investigation. The strength and promise of this model lies in its ability to predict flow phenomena in a patient-specific cerebral tree in a matter of minutes on a desktop or laptop level computing system, rather than the 100+ fold increase in time and/or computing power as required by 3D models.

It is worth noting that the vascular model of this work is based on a complete and functioning CoW, which are the prerequisites of the proximal protection procedure. However, as pointed out in [6], many anatomical variations of CoW exist and we expect different flow patterns to arise accordingly. Hence, a clinically relevant flow analysis should be patient-specific, i.e., as per patients' actual vascular anatomies. Nevertheless, our computational model serves as an efficient and powerful tool from patient-specific vasculature construction to meaningful hemodynamic analysis.

5 Conclusion

In this work we employed a computational approach to study the proximal embolic protection mechanism used in carotid angioplasty. The initial results from our computational model agree with published flow measurements. Future work includes experimenting with different boundary treatments to improve model accuracy and applying such a model to the circulation research in some relevant clinical studies of the brain or other vascular organs.

References

1. Parodi, J.C., Ferreira, L.M., Sicard, G., Mura, R.L., Fernandez, S.: Cerebral protection during carotid stenting using flow reversal. Journal of Vascular Surgery, 41(3), 416–422 (2005)
2. Reimers, B., Sievert, H., Schuler, G.C., et al.: Proximal endovascular flow blockage for cerebral protection during carotid artery stenting: results from a prospective multicenter registry. Journal of Endovascular Therapy, 12, 156–165 (2005)
3. Cremonesi, A., Manetti, R., Setacci, F., et al.: Protected carotid stenting: clinical advantage and complications of embolic protection devices in 442 consecutive patients. Stroke, 34, 1936–1941 (2003)
4. Smith, N.P., Pullan, A.J., Hunter, P.J.: An anatomically based model of transient coronary blood flow in the heart. SIAM Journal of Applied Mathematics, 62(3), 990–1018 (2000)
5. Barnard, A.C., Hunt, W.A., Timlake, W.P., Varley, E.: A theory of fluid flow in compliant tubes. Biophysical Journal, 6, 718–724 (1966)
6. Alastruey, J., Parker, K., Peiro, J., Byrd, S., Sherwin, S.: Modelling the circle of Willis to assess the effects of anatomical variations and occlusions on cerebral flows. Journal of Biomechanics, 40, 1794–1805 (2007)
7. Long, Q., Luppi, L., Konig, C.S., Rinaldo, V., Das, S.K.: Study of the collateral capacity of the circle of Willis of patients with severe carotid artery stenosis by 3D computational modeling. Journal of Biomechanics, 41(12), 2735–2742 (2008)
8. Anderson, J.D.: Computational fluid dynamics: the basics with applications. McGraw-Hill, Inc., (1995)
9. Mills, C.J., Gabe, I.T., Gault, J.H., et al.: Pressure-flow relationships and vascular impedance in man. Cardiovascular Research, 4(4), 405–417 (1970)
10. Lindegaard, K.F., Nornes, H., Bakke, S.J., Sorteberg, W., Nakstad, P.: Cerebral vasospasm diagnosis by means of angiography and blood velocity measurements. Acta Neurochir (Wien), 100, 12–24 (1989)

Chapter 6
Cortical Surface Motion Estimation for Brain Shift Prediction

Grand Roman Joldes, Adam Wittek, and Karol Miller

Abstract In this chapter we present an algorithm for computing the displacement of the exposed surface of the brain during surgery. The motion of the cortical surface is recovered by registering the preoperative surface extracted from high-resolution MRI images to the intraoperative surface acquired during surgery. The recovered motion can then be used for driving a biomechanical model in order to predict the displacement of the internal brain structures, especially the tumor, which can be presented to the surgeon using an image-guided neurosurgery system. Our algorithm combines an image registration method with curvature information associated with the features of the brain surface to perform the non-rigid surface registration. The extracted displacement field can be used directly for driving a biomechanical model, as it does not include any implausible deformations. It also works in cases when the boundaries of the two registered surfaces are not identical, extracting the displacements only for the overlapping regions of the two surfaces. We tested the accuracy of the proposed algorithm using synthetically generated data as well as surfaces extracted from preoperative and intraoperative MRI images of the brain.

Keywords Non-rigid surface registration · Brain shift · Nonlinear biomechanical models

1 Introduction

Determination of the misalignment between the actual position of pathology and its position determined from preoperative images is one of the key challenges facing the image-guided neurosurgery. A typical example is the craniotomy-induced

G.R. Joldes (✉)
Intelligent Systems of Medicine Laboratory, School of Mechanical Engineering,
The University of Western Australia, Crawley 6009, WA, Australia
e-mail: grandj@mech.uwa.edu.au

brain shift that results in movement of the pathology (tumor) and critical healthy tissues. As the contrast and spatial resolution of the intraoperative images are typically inferior to the preoperative ones [1], the high-quality preoperative data need to be aligned to the intraoperative brain geometry to retain the preoperative image quality during the surgery. Accurate alignment must take into account the brain deformation, which implies non-rigid registration. To ensure the plausibility of the predicted deformation field, many authors have proposed the use of biomechanical models for non-rigid brain registration that take into account the mechanical properties of the anatomical structure depicted in the image [2–4]. Some of these models are driven by externally applied forces (pressure, gravity) [5] that try to simulate the loading conditions, while others are driven by displacements evaluated based on intraoperative images or using external devices [6–13]. The finite element method (FEM) is in most cases the method of choice for finding the solution.

Driving the biomechanical model by using displacements of the surface has the main advantage over the methods involving prescribed forces/pressure that the computed deformation field depends only weakly on the material properties [14]. This is an important advantage given the variability of tissue properties between patients and the difficulty of measuring these properties.

The preoperative brain surface can be segmented from high-resolution preoperative MRI images. Various methods have been proposed for measuring the intraoperative position of the brain surface in the area of the craniotomy, such as using a laser range scanner [15] or a stereo vision system [13, 16, 17]. After the intraoperative and preoperative coordinate systems have been aligned, the next step is the estimation of the displacements of the mesh nodes located in the area of the craniotomy, which involves the non-rigid registration of the intraoperative and the preoperative brain surface.

There are several challenges involved in performing the displacement estimation:

- The mesh nodes are not located on the preoperative brain surface – because the convolutions of the brain surface are usually aggressively smoothed before generating the mesh.
- The brain surface is very convoluted.
- The boundaries of the preoperative and intraoperative surfaces are irregular and mismatched – an alignment of the boundaries cannot be performed.

The usual method used for performing the surface registration is the iterative closest point method (ICP) [13, 16, 17]. This approach is constrained to a rigid transformation and does not capture the often non-rigid tissue motion. Miga et al. has shown in [15] that combining the data obtained using a laser range scanner with a feature-rich texture as acquired by a color CCD camera can lead to better registration results compared to the traditional point-based approaches. The difficulty of that approach is to establish the correspondence between the different intensity distributions in the two images.

In this chapter we propose a displacement estimation algorithm that can overcome the above-mentioned problems, calculating a plausible non-rigid deformation

field. The algorithm is presented in the next section, validation results are presented in Section 3, and discussions and conclusions are presented in Section 4.

2 Cortical Surface Displacement Estimation

2.1 Algorithm Description

We consider that the brain surface in the preoperative position (PS) has been aligned (brought to the same coordinate system) with the brain surface in the intraoperative position (IS). In the same coordinate system, the nodes of the brain mesh corresponding to the preoperative surface (PN) have been identified. As stated before, these nodes may not lay on the preoperative surface, but should be close to it. Our purpose is to estimate the displacements of the nodes PN between the two surfaces PS and IS.

Using point-based methods, the two surfaces are considered as being two clouds of points and therefore the information related to the geometry and features of the surfaces is lost. Moreover, the fact that the surfaces are very feature rich can lead to inaccuracies in the recovered displacements as well as to implausible deformation field estimation.

We propose to use the geometry of the brain surface in the registration process. Even if the brain surface undergoes non-rigid deformation, the main features on the surface (the sulcal pattern) preserve their basic geometry. We incorporate this geometry information into the registration algorithm by using the Gaussian curvature [18] for characterizing it.

Without any loss of generality we suppose that the brain surface is viewed from the positive z axis. This axis would normally coincide with the camera axis, offering the largest exposure of the surface to the camera. The two positions of the surface can therefore be represented as two triangular surface meshes containing the points $z_{PS} = z_{PS}(x_{PS}, y_{PS})$ and $z_{IS} = z_{IS}(x_{IS}, y_{IS})$, while the displaced brain mesh nodes corresponding to PS can be represented as $z_{PN} = z_{PN}(x_{PN}, y_{PN})$. The main steps of the cortical surface displacement estimation algorithm are as follows:

1. Create a uniform grid in the plane xOy over a rectangular region that includes the points (x_{PS}, y_{PS}) and (x_{IS}, y_{IS})
2. Calculate the Gaussian curvature for PS and IS using finite differences over the uniform grid. The z values of the surface at the grid points are calculated using interpolation. A small degree of smoothing is introduced in order to eliminate the high-frequency irregularities in the mesh.
3. Generate a grayscale curvature image for each surface. Each pixel of the image corresponds to a grid point and the color of each pixel is a scaled value of the curvature at the corresponding grid point. For each image we also generate a mask that identifies the region of interest in the image (the pixels corresponding to the surface projection).

4. Perform a non-rigid registration of the two curvature images, using an elastic and consistent image registration algorithm based on elastic deformations represented by B-splines [19]. After this step a B-spline mapping BS between the projections in the xOy plane corresponding to the two surfaces is obtained.
5. Find the position of the mesh points PN on the smoothed preoperative surface SPS. The smoothing of the surface will make it resemble the mesh surface by eliminating the sulcal patterns. The position of the mesh points on SPS is given by the z value of this surface at the projection of the mesh points on the xOy plane: $z_{SPS} = z_{SPS}(x_{PN}, y_{PN})$.
6. Find the mapping of points (x_{PN}, y_{PN}) on the projection of the intraoperative surface using the B-spline mapping $(x_{PNI}, y_{PNI}) = BS(x_{PN}, y_{PN})$
7. Find the corresponding points on the smoothed intraoperative surface SIS. The smoothing of the intraoperative surface is done using the same parameters as for SPS. These points are given by $z_{SIS} = z_{SIS}(x_{PNI}, y_{PNI})$.
8. Calculate the displacements of the mesh nodes as

$$(dx, dy, dz) = (x_{PNI}, y_{PNI}, z_{SIS}) - (x_{PN}, y_{PN}, z_{SPS})$$

Steps 1–3 transform the 3D surface registration problem into a 2D image registration problem, which can be solved using existing algorithms (Step 4). During the generation of the biomechanical model, the brain surface is usually smoothed, in order to facilitate the mesh creation. This means that the displacements applied to the model should be smoothed as well, and this smoothing process is included in Steps 5–7 of the registration algorithm. From the registration point of view, these steps are not needed, but they are essential for our practical application.

2.2 Preoperative Surface Extraction

The preoperative surface is usually extracted from high-resolution preoperative images such as MRI. We performed the surface extraction in the area of the craniotomy using the following procedure:

- Supersample the MRI image in order to reduce aliasing – this will lead to a smoother surface after segmentation. We used the same voxel size in all directions in order to avoid the staircase effect given by irregular voxels. For example, an original image with voxel size of $0.5 \times 0.5 \times 1$ mm^3 was supersampled to an image with voxel size of $0.5 \times 0.5 \times 0.5$ mm^3.
- Segment the resulting image to extract the brain surface in the area of the craniotomy. We used an intensity (threshold)-based segmentation algorithm with manual correction of the resulting mask.
- Generate the brain surface based on the segmentation. This has been done in Slicer (www.slicer.org), using only a small degree of smoothing, in order to preserve the sulcal pattern. The surface is obtained as a triangular mesh.

- Because we need the surface as $z_{PS} = z_{PS}(x_{PS}, y_{PS})$, a visible surface determination algorithm is applied in order to eliminate the nodes obscured by other triangles in the Oz direction.

2.3 Implementation and Parameter Selection

All steps of the algorithm, except the image registration algorithm (Step 4), have been implemented in Matlab [20]. For the image registration step we used the Java implementation of the algorithm available as a plug-in (bUnwarpJ – http://biocomp.cnb.uam.es/~iarganda/bUnwarpJ/) for the image processing and analyzing software ImageJ (http://rsb.info.nih.gov/ij/). The purpose of this implementation is to study and validate the algorithm, with no concern about the computation efficiency. For use in a clinical setting, an implementation in a compiled language (such as C) would be needed.

The smoothing of the mesh (Steps 2, 5, and 7) is done using the cubic smoothing spline function available in Matlab (csaps). The smoothing parameter was $p = 0.1$ for Step 2 and $p = 0.001$ for Steps 5 and 7 ($p = 1$ means no smoothing). These smoothing parameters seem to give good results for all the analyzed cases.

The effect of the grid density and smoothing on the curvature images is presented in Fig. 6.1. Without smoothing, the curvature map is dominated by the high curvatures of the sulci, and increasing the grid density leads to worse image quality (Fig. 6.1c, f). When smoothing is used, the image quality increases with the grid density (Fig. 6.1b, e). We used a grid size of 500×500 to generate the images. For the surface presented in Fig. 6.1, which is about 100×100 mm in size, this
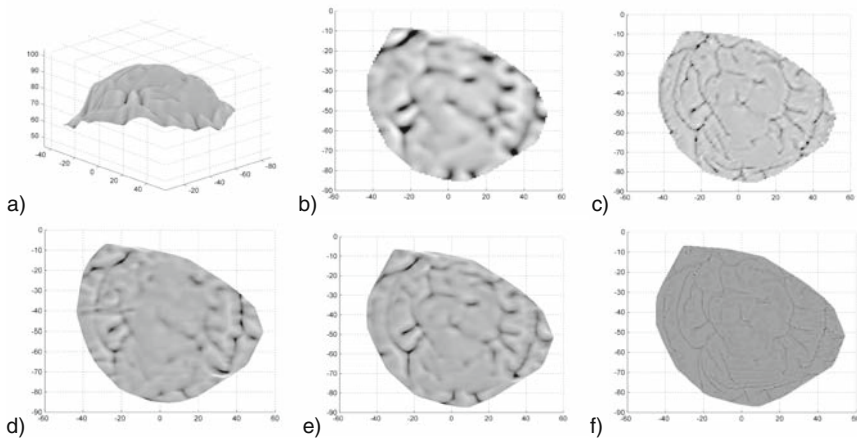
Fig. 6.1 Effects of grid size and smoothing on the curvature images. (**a**) Preoperative surface. (**b**) Preoperative curvature image, 100×100, $p = 0.1$. (**c**) Preoperative curvature image, 100×100, no smoothing. (**d**) Intraoperative curvature image, 500×500, $p = 0.1$. (**e**) Preoperative curvature image, 500×500, $p = 0.1$. (**f**) Preoperative curvature image, 300×300, no smoothing

corresponds to a pixel size of 0.2×0.2 mm^2, which is much smaller than the voxel dimensions in the MRI image. In Fig. 6.1d we present the curvature map of the corresponding intraoperative surface, segmented from an intraoperative MRI. It is obvious that the sulcal pattern is not as clear as in the preoperative image (Fig. 6.1e), because of the lower spatial resolution of the intraoperative MRI ($0.86 \times 0.86 \times 2.5$ mm^3 in this case), but it is still visible and the correspondence to the preoperative curvature map can be easily noticed.

The elastic image registration (Step 4) is performed in ImageJ using the default parameters, based on the curvature images and the corresponding masks. The algorithm performs very well without the need of any human intervention and without the need of selecting any landmarks on the images. The result of this step is a text file containing the coefficients of the B-spline function that maps the preoperative curvature image to the intraoperative curvature image. An example of a deformation field obtained is presented in Fig. 6.2.
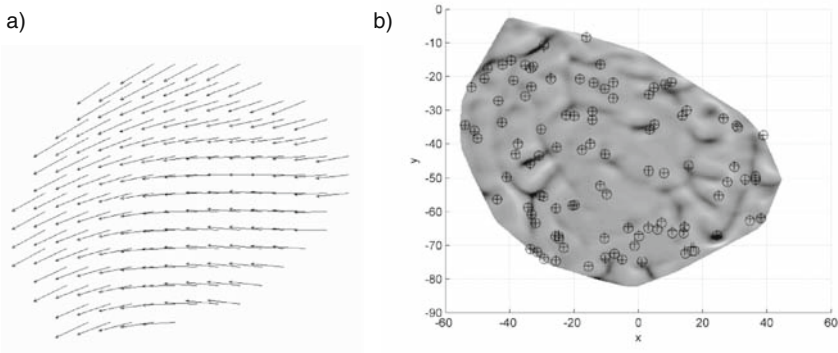
Fig. 6.2 Results of the elastic image registration of the curvature maps using synthetically generated data. (**a**) Deformation field. (**b**) Errors for 200 randomly selected nodes – actual position of the nodes is marked with a *circle* and the computed position is marked with a *plus*. The mean error is 0.29 mm, with a standard deviation of 0.23

3 Validation Results

In order to validate the proposed algorithm, we performed two types of experiments. The purpose of the first experiment was to verify how accurately the algorithm can recover the displacements based on the curvature maps. In this experiment we used synthetically generated test data, created by adding a known displacement field to a segmented brain surface (presented in Fig. 6.1a).

The displacement field was created by adding a known displacement to each node of the surface in the Oz direction (following a sinusoidal curve) and by rotating (around the Ox axis) and translating the resulting surface. The resulting displacement field (projected on the xOy plane) is presented in Fig. 6.2a. We applied Steps

1–4 of the algorithm on the original and deformed surfaces, and compared the computed position of the deformed surface nodes with their known position. The results are presented in Fig. 6.2. The displacement field in the xOy plane was recovered based on the curvature maps, with a mean error of 0.29 mm (standard deviation 0.23, maximum 1.6). By analyzing the distribution of the error on the surface, we found out that the highest error values (>1 mm) occur in localized areas around the edge of the surface.

In the first experiment we could not validate Steps 5–8 of the algorithm, which include some smoothing of the surfaces, as these steps are only needed when the algorithm is used together with a biomechanical model. We tested these steps on brain surfaces extracted from preoperative and intraoperative MRI images, for four craniotomy-induced deformation cases. In this experiment we used the recovered surface displacements in the craniotomy area to load biomechanical models of the brain. The obtained volumetric deformation field was then used to find the intraoperative position of the brain surface (extracted from the preoperative images using intensity-based segmentation). We can obtain a qualitative validation of the method by superimposing this surface on the intraoperative MRIs and comparing it with the contour of the brain in the craniotomy area. Quantitative results could not be obtained for these experiments, as the ground truth (the real position of the intraoperative surface) cannot be accurately extracted from the intraoperative MRI images.

Because the brain surface follows very closely the surface of the biomechanical model (except the fact it is not as smooth), the performance and material properties of the biomechanical model does not have a big influence on the obtained surface registration results. The nonlinear biomechanical models and finite element algorithms we use lead to very good deep structure registration results, their performances being demonstrated in our previous papers [10, 21, 22]. Representative results are presented in Fig. 6.3. A very good match of the computed brain surface to the brain MRI image can be observed.

Although the implementation has been done using Matlab and Java (ImageJ), which are basically interpreted languages, the algorithm performed very fast, the overall computation time being in order of seconds (less than a minute). From our experience, an implementation in a compiled language (such as C) would perform several times faster.

4 Discussion and Conclusions

We presented a new algorithm for extracting the cortical surface displacements in the craniotomy area. The geometrical information about the brain surface is captured using the curvature map of the sulcal pattern. The curvature maps of the preoperative and intraoperative brain surfaces are registered using an elastic and consistent image registration algorithm. This registration algorithm, together with smoothing of the registered surfaces, ensures smooth and realistic displacement field estimation. The validation experiments prove the very good performance of the algorithm.
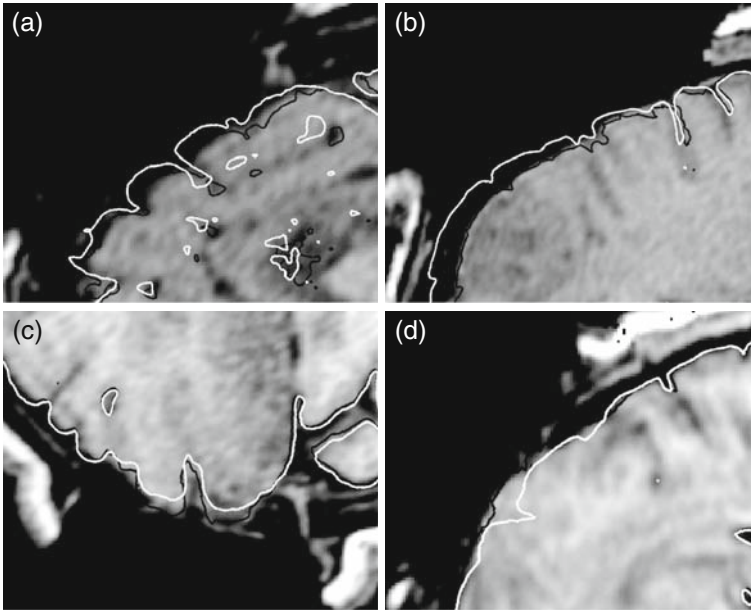
Fig. 6.3 Computed deformations of the brain surface using biomechanical models for four craniotomy-induced displacements cases. The preoperative brain surface (*white*) and the computed intraoperative brain surface (*black*) are superimposed on the intraoperative MRI

The registration algorithm is able to handle brain surfaces with irregular non-matching boundaries. In the analyzed cases, the registration has been performed without any human intervention. In case the surfaces are not rigidly aligned, some human intervention might be required (to specify the correspondence between at least three points for an initial rigid registration).

The results obtained using synthetically generated data, as well as real surfaces segmented from preoperative and intraoperative MRIs, demonstrate the registration accuracy of the algorithm.

The algorithm performed very fast, although it was implemented using interpreted languages (Matlab, Java). An implementation in a compiled language will further increase its performance.

References

1. Warfield, S.K., Haker, S.J., Talos, I.-F., Kemper, C.A., Weisenfeld, N., Mewes, U.J., Goldberg-Zimring, D., Zou, K.H., Westin, C.-F., Wells, W.M., Tempany, C.M.C., Golby, A., Black,

P.M., Jolesz, F.A., Kikinis, R.: Capturing intraoperative deformations: research experience at Brigham and Women's hospital. Medical Image Analysis, 9, 145–162 (2005)

2. Warfield, S.K., Talos, F., Tei, A., Bharatha, A., Nabavi, A., Ferrant, M., Black, P.M., Jolesz, F.A., Kikinis, R.: Real-time registration of volumetric brain MRI by biomechanical simulation of deformation during image guided surgery. Computing and Visualization in Science, 5, 3–11 (2002)

3. Archip, N., Clatz, O., Whalen, S., Kacher, D., Fedorov, A., Kot, A., Chrisochoides, N., Jolesz, F., Golby, A., Black, P.M., Warfield, S.K.: Non-rigid alignment of pre-operative MRI, fMRI, and DT-MRI with intra-operative MRI for enhanced visualization and navigation in image-guided neurosurgery. NeuroImage, 35, 609–624 (2007)

4. Hu, J., Jin, X., Lee, J.B., Zhang, L., Chaudhary, V., Guthikonda, M., Yang, K.H., King, A.I.: Intraoperative brain shift prediction using a 3D inhomogeneous patient-specific finite element model. Journal of Neurosurgery, 106, 164–169 (2007)

5. Clatz, O., Delingette, H., Bardinet, E., Dormont, D., Ayache, N.: Patient specific biome-chanical model of the brain: application to Parkinson's disease procedure. In: Ayache, N., Delingette, H. (eds.) International symposium on surgery simulation and soft tissue modeling (IS4TM'03), Vol. 2673. Springer-Verlag, Juan-les-Pins, France, pp. 321–331 (2003)

6. Ferrant, M., Nabavi, A., Macq, B., Black, P.M., Jolesz, F.A., Kikinis, R., Warfield, S.K.: Serial registration of intraoperative MR images of the brain. Medical Image Analysis, 6, 337–359 (2002)

7. Hagemann, A., Rohr, K., Stiehl, H.S.: Coupling of fluid and elastic models for biomechanical simulations of brain deformations using FEM. Medical Image Analysis, 6, 375–388 (2002)

8. Hagemann, A., Rohr, K., Stiehl, H.S., Spetzger, U., Gilsbach, J.M.: Biomechanical modeling of the human head for physically based, nonri gid image registration. IEEE Transaction on Medical Imaging, 18, 875–884 (1999)

9. Warfield, S.K., Ferrant, M., Gallez, X., Nabavi, A., Jolesz, F.A., Kikinis, R.: Real-time biome-chanical simulation of volumetric brain deformation for image guided neurosurgery. SC 2000: High Performance Networking and Computing Conference, Vol. 230, Dallas, USA, pp. 1–16 (2000)

10. Wittek, A., Miller, K., Kikinis, R., Warfield, S.K.: Patient-specific model of brain deformation: application to medical image registration. Journal of Biomechanics, 40, 919–929 (2007)

11. Miller, K., Wittek, A.: Neuroimage registration as displacement – zero traction problem of solid mechanics. Computational Biomechanics for Medicine Workshop, Medical Image Computing and Computer-Assisted Intervention MICCAI 2006, Copenhagen, Denmark (2006)

12. Wittek, A., Kikinis, R., Warfield, S.K., Miller, K.: Brain shift computation using a fully non-linear biomechanical model. 8th International Conference on Medical Image Computing and Computer Assisted Surgery MICCAI 2005, Palm Springs, California, USA (2005)

13. Hai, S., Lunn, K.E., Hany, F., Ziji, W., Roberts, D.W., Alex, H., Paulsen, K.D.: Stereopsis-guided brain shift compensation. IEEE Transactions on Medical Imaging, 24, 1039–1052 (2005)

14. Wittek, A., Hawkins, T., Miller, K.: On the unimportance of constitutive models in computing brain deformation for image-guided surgery. Biomechanics and Modeling in Mechanobiology (2008) DOI: 10.1007/s10237-10008-10118-10231

15. Miga, M.I., Sinha, T.K., Cash, D.M., Galloway, R.I., Weil, R.J.: Cortical surface registration for image-guided neurosurgery using laser-range scanning. IEEE Transactions on Medical Imaging, 22, 973–985 (2003)

16. Sun, H., Farid, H., Rick, K., Hartov, A., Roberts, D.W., Paulsen, K.D.: Estimating cortical surface motion using stereopsis for brain deformation models. Medical Image Computing and Computer-Assisted Intervention – MICCAI 2003, Vol. 2878/2003. Springer Berlin, Heidelberg, pp. 794–801 (2003)

17. Skrinjar, O., Nabavi, A., Duncan, J.: Model-driven brain shift compensation. Medical Image Analysis, 6, 361–373 (2002)

18. Gray, A.: The Gaussian and mean curvatures. Modern differential geometry of curves and surfaces with mathematica. CRC Press, Boca Raton, FL pp. 373–380 (1997)
19. Arganda-Carreras, I., Sorzano, C.O.S., Marabini, R., Carazo, J.M., Ortiz-de-Solorzano, C., Kybic, J.: Consistent and elastic registration of histological sections using vector-spline regularization. Lecture Notes in Computer Science, 4241, 85–95 (2006)
20. Nakamura, S.: Numerical analysis and graphic visualization with Matlab. Prentice Hall PTR, Upper Saddle River (1996)
21. Joldes, G.R., Wittek, A., Miller, K.: Suite of finite element algorithms for accurate computation of soft tissue deformation for surgical simulation. Medical Image Analysis (2008) DOI: 10.1016/j.media.2008.1012.1001
22. Miller, K., Wittek, A., Joldes, G.R., Horton, A., Roy, T.D., Berger, J., Morriss, L.: Modelling brain deformations for computer-integrated neurosurgery. Communications in Numerical Methods in Engineering, 26(1), 117–138 (2009)

Chapter 7
Method for Validating Breast Compression Models Using Normalised Cross-Correlation

Angela W.C. Lee, Vijay Rajagopal, Jae-Hoon Chung, Poul M.F. Nielsen, and Martyn P. Nash

Abstract To diagnose and manage breast cancer, X-ray mammography, ultrasound, and magnetic resonance (MR) imaging are used to image the breasts. In this chapter, we present a method for validating finite element (FE) biomechanical models across the entire breast volume. A computational framework was used to generate personalised FE models of the breast to predict the deformations of the breasts under compression. A Fourier-based correlation technique was used to compare localised mismatches between 3D model-warped images and clinical MR images. This technique is illustrated by matching model-simulated compressed images with MR data for a compressed breast phantom and the compressed breasts of two volunteers. The results from this analysis indicate regions of the biomechanical model that do not align well, and thus require improvement. A validated biomechanical image registration tool of this kind will help clinicians to more accurately localise breast cancers, enabling more reliable diagnoses.

Keywords Finite Element Method · Biomechanical breast models · Non-rigid registration

1 Introduction

Breast cancer is the leading cause of cancer mortality for women worldwide. Studies have shown that early detection through X-ray mammographic screening programs can reduce the mortality rate for women afflicted with the disease [1]. Other modalities, such as magnetic resonance imaging (MRI) and ultrasound, are used in conjunction with X-ray mammography for the diagnosis and management of breast cancer. Image acquisition under each of these modalities occurs with the breasts placed in markedly different positions and subject to different loading conditions. For example, during mammography the breast is compressed between two

A.W.C. Lee (✉)
Auckland Bioengineering Institute, The University of Auckland, Auckland, New Zealand
e-mail: angela.lee@auckland.ac.nz

plates to improve image contrast; with MRI scans, patients typically lie in a prone position; whereas the patient is in a supine position during ultrasound imaging [2].

Non-rigid registration algorithms have already been developed and applied to the various breast images to aid clinicians in their interpretation [3, 4]. Some methods use biomechanical models to predict the deformation of breast and track the locations of tumours in the breast as the loading conditions are altered [5–10]. Approaches to quantitatively validate these models typically assess their ability to predict the displacement of manually identified internal landmarks [5–10] by comparing the deformation of the breast skin surface through the use of fiducial skin markers [5] or by projecting the actual skin surface onto the model [9, 10].

In this chapter, we present a technique that uses 3D image data across the entire breast volume to quantitatively assess biomechanical model predictions on a localised basis. The 3D image comparison technique that we have developed is similar to the 2D non-rigid registration algorithm technique proposed by Periaswamy et al. [11], where a hierarchical scheme was used to find the translational and rotational parameters for small regions within the images. The reference image was then warped to the target image using thin-plate splines with the transformation parameters.

The biomechanical breast model used in this chapter is based on the modelling framework proposed by Chung et al. [9]. We simulate breast deformation using contact mechanics constraints, with kinematic inputs being the initial and final positions of the compression plates. To validate the biomechanical model, magnetic resonance (MR) images were acquired before and during compressions. The clinical images of the uncompressed breast were warped using individual-specific biomechanical models and compared against the ground truth clinical images of the breast under compression using the image comparison algorithm we developed.

2 Methods

2.1 Magnetic Resonance Imaging of Breast Compression

Two volunteers were recruited and a 1.5T Siemens MR scanner was used to acquire T_2-weighted images of the left breasts before and during latero-medial compression using a breast coil. The volunteers were asked to lie in a prone position with the breast hanging pendulous in the breast coil. The breasts were then compressed in the medio-lateral direction using the pads integrated in the breast coil. During compression the pads at the medial edge were held immobile, while the lateral pads were translated towards the sternum. T_2 weighting was used with iPAT turned on for a faster acquisition time. The image dimensions were 512×512 pixels with a 350×350 mm field of view with approximately 60 slices with 2.5 mm slice thickness. For volunteer 1, the breast was compressed by 32% of the initial width of the breast, and for volunteer 2 the breast was imaged under 19 and 38% compression.

A CIRS triple modality biopsy training breast phantom, containing 12 internal masses, was used to validate our image comparison methods. In comparison to the

breast MR images the MR images of the breast phantom were less noisy, as there were no breathing or motion artefacts. The breast phantom was imaged before and during a 38% compression with a T_1-weighted FL3D pulse sequence. The slice thickness used for the phantom was 0.75 mm.

2.2 Image Warping Using Finite Element Models

MRI data for the uncompressed volunteers' breasts and the breast phantom were segmented and used to create customised finite element (FE) models. The FE software, CMISS, was used to predict the large deformations due to compression loads using finite deformation elasticity coupled with contact constraints [9]. Biomechanical models were used to non-rigidly warp the MR images of the uncompressed bodies to simulate compression [12]. To assess the predictive ability of the biomechanical model, the simulated images were compared with MR images of the compressed objects. The breast phantom was modelled as an isotropic, homogeneous, and incompressible material. The entire breast phantom was compressed, with no attachment points to external bodies. Therefore, the interaction between the breast phantom and the compression plates was modelled using frictional contact constraints as the boundary condition [13].

Assumptions of homogeneity, isotropy, and incompressibility were also applied to the breast models. The breast tissues were allowed to slide along the ribs to mimic the loose attachment of the breast tissues to the rib surface. The interaction between the breast tissues and the compression plates was modelled as frictionless contact. For more detail about the modelling techniques, please refer to Chung et al. [9].

2.3 Image Analysis and Comparison

In this chapter, we present a fast Fourier transform (FFT)-based algorithm for comparing the 3D model-warped images with the 3D clinical images. The method presented here is similar to an approach used by Periaswamy et al. [11] to non-rigidly register medical images by optimising a similarity measure to determine the rigid translation and rotation of each region. These parameters were combined with thin-plate spline warping at each iteration to non-rigidly register two images.

Our technique uses normalised cross-correlation (NCC) to find the global rigid translation between the two images. A cosine-tapered windowing function was applied to the images to reduce wrap-around errors in the frequency domain. We found that high-frequency noise in the images had a detrimental effect on this comparison measure. To counter this, we low-pass filtered and reduced the resolution of the images. The coarsest resolution was used for the initial translation, while the higher resolution images were used for the subsequent iterations, with the final iteration using the unblurred images. An FFT-based cross-correlation technique was used to find the 3D rigid translation between the images (see Fig. 7.1).
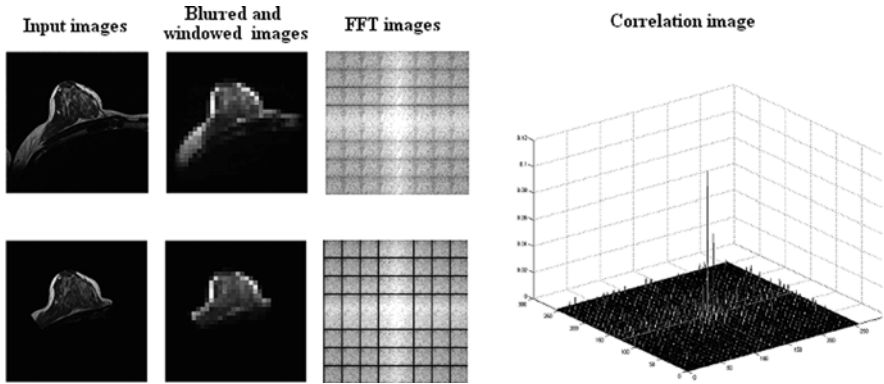
Fig. 7.1 Determine optimal rigid translation between two 3D images. The two input images were blurred and windowed, before being put into the frequency domain to find the optimal cross-correlation between the images

We used a hierarchical approach, where the simulated images were subdivided into overlapping sub-regions and compared with a corresponding sub-region in the clinical image. The shift that maximised the cross-correlation for each step was used as an initial translation for the next iteration of the algorithm. The sub-region size was iteratively reduced and the resolution was increased and this coarse-to-fine registration continued until the region size was diminished to an approximately 5 × 5 × 5 mm volume (see Fig. 7.2). The outputs from this comparison algorithm were error vectors for each overlapping sub-region and the corresponding normalised cross-correlation values (see Figs. 7.1 and 7.2).
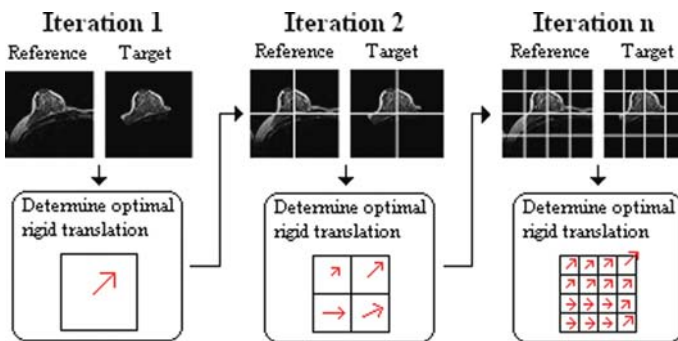
Fig. 7.2 The optimal rigid translations are found for the regions at each iteration and were used as the initial translations for each of the regions for the subsequent iteration

3 Results

3.1 Validation of Comparison Method Using a Breast-Shaped Phantom

The method was applied to MR images of the breast phantom. Images of the uncompressed phantom were warped using the biomechanical model to a 38% compression (Fig. 7.3). These images were then resampled to allow direct comparison with the images of the compressed phantom. The final output of the hierarchical comparison was a 3D map of the error vectors between $5.5 \times 5.5 \times 6$ mm regions for the model-warped and clinical 3D images.
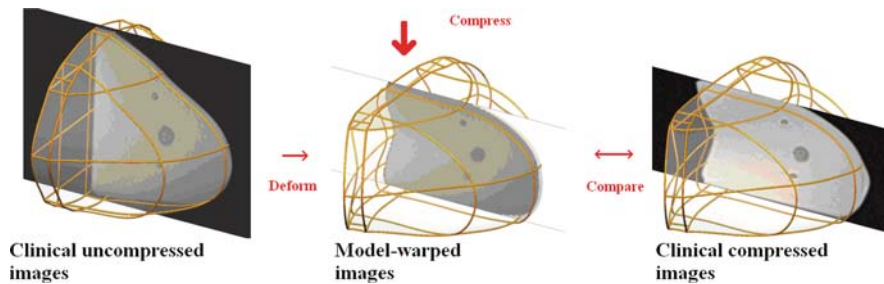
Fig. 7.3 MR images of the uncompressed phantom were embedded into the unloaded FE model and were warped according to the model deformations. The model-warped images were then compared with the clinical images of the compressed phantom

An independent measure of the error of the FE model was estimated by manually tracking the landmarks of the breast phantom. Locations of the 12 internal masses were predicted in the compressed state using the biomechanical model (see Fig. 7.4). The error of the FE model was then estimated by comparing the 12 predictions with the clinical images of the compressed phantom. To assess the validity of our comparison measure, we compared the manually tracked error vectors with those computed by the algorithm. The RMS error for manually tracking the lesions was found to be 2.3 mm, while the equivalent RMS error measure from the image comparison method was 1.8 mm. The mean and standard deviation of the magnitude of the difference between the corresponding error vectors (from the two methods) was 1.5 ± 0.7 mm.

3.2 Application to Breast Biomechanical Modelling

In Fig. 7.5, images of the uncompressed breast were warped using an FE model to simulate 32% compression for volunteer 1. In Figs. 7.6 and 7.7 the volunteer 2 model was used to simulate images of the breast under 19 and 38% compression, respectively. The validity of the model predictions were then tested by comparing the model-warped images with clinical images of the breasts under compression
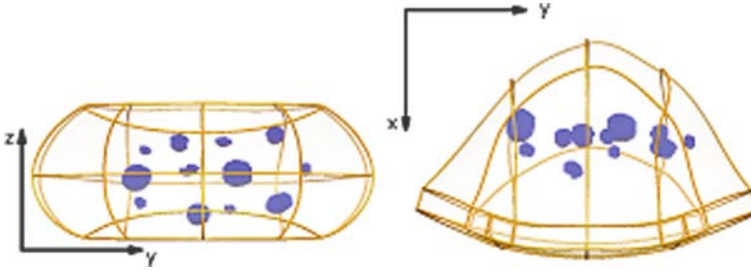
Fig. 7.4 The breast phantom contained 12 internal masses. The locations of these lesions when the phantom was compressed were predicted using the biomechanical model
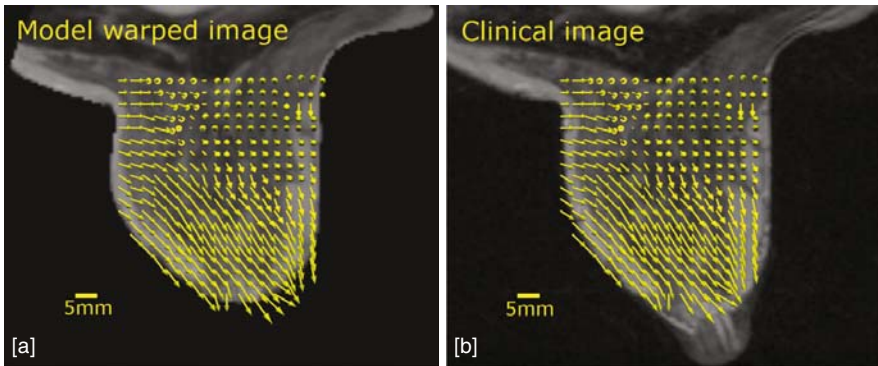
Fig. 7.5 The error vector field for comparing the model-warped images against the clinical images for 32% compression for volunteer 1 was overlaid on a 2D slice of (**a**) the model-warped image and (**b**) the clinical image. The RMS error for our comparison measure was 4.4 mm
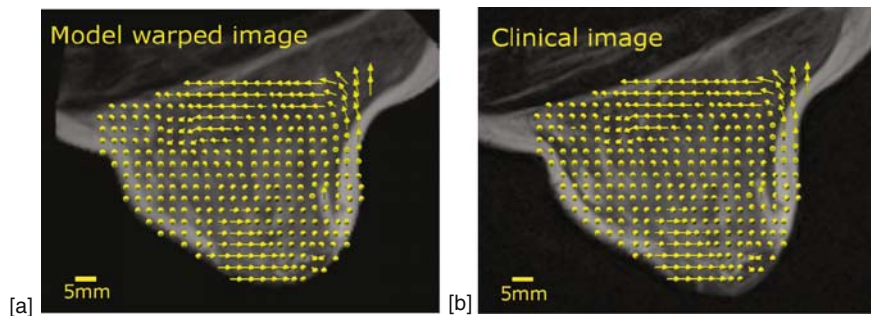
Fig. 7.6 The error vector field for comparing the model-warped images with the clinical images for 19% compression for volunteer 2 was overlaid on a 2D slice of (**a**) the model-warped image and (**b**) the clinical image. The RMS error for our comparison measure was 3.9 mm

using our algorithm. A quantitative measure of the error of the FE models cases was established by calculating the RMS differences. The 32% compression for volunteer 1 was predicted with an overall RMS error of 4.4 mm, while for volunteer 2 the RMS errors were 3.9 and 4.1 mm for 19 and 38% compression, respectively.
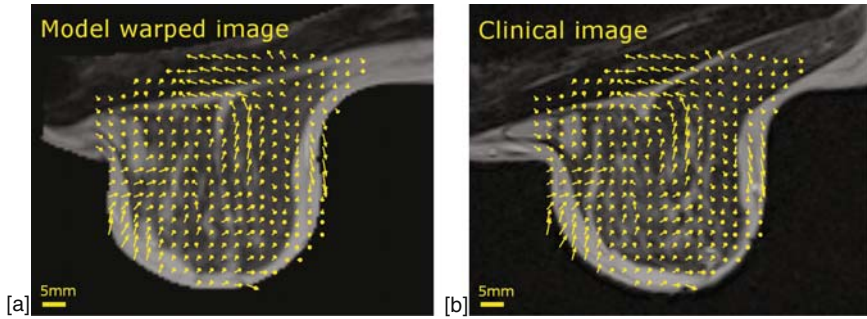
Fig. 7.7 The error vector field for comparing the model-warped images with the clinical images for 38% compression for volunteer 2 was overlaid on a 2D slice of (**a**) the model-warped image and (**b**) the clinical image. The RMS error for our comparison measure was 4.1 mm

4   Discussion

A biomechanics modelling framework was used to simulate the deformations of breast tissues under compression loading conditions [9]. In order to validate these modelling techniques, we compared the model simulations with clinical image data. We presented a Fourier-based comparison method for 3D images and have applied it to assess the ability of FE models to simulate compression of a phantom and breasts of two volunteers to provide insight into how to improve the biomechanical models.

A block matching approach was used, where the optimal rigid translation between two blocks is found using normalised cross-correlation (NCC). In this chapter, the optimal NCC was determined using the Fourier domain as this provides a more efficient calculation compared with the spatial domain due to the size of the images. The NCC algorithm is generally only appropriate for the comparison of images from the same modality. The MR images that we have compared were obtained with the same imaging sequence and therefore had similar intensity distributions over the breast.

We have applied the technique to MR images in order to validate the FE models. However, breast tissues are also imaged using mammograms and ultrasound, and these modalities display quite different information about the breast tissues. In order to compare images from different modalities, it may be more appropriate to incorporate other similarity measures, such as normalised mutual information, into the comparison algorithm.

In Section 3.1, we created a FE model for a breast phantom and used it to simulate 38% compression. Images of the uncompressed breast phantom were embedded into this model and warped according to the predictions. To validate the image comparison method, the locations of 12 internal landmarks in the breast phantom were manually tracked. The main advantage of the new method is that it can automatically determine the accuracy over the entire 3D volume, whereas feature tracking is reliant on clearly identifiable landmarks, which are typically limited to a relatively small number, and their identification can be operator subjective. An independent measure of the accuracy of the FE method was determined by comparing the centroids of the

12 predicted masses with those of the actual lesions in the clinical images. This measure of accuracy was then compared with the image comparison technique proposed in this chapter. The mean and standard deviation of the difference vector magnitude was 1.5 ± 0.7 mm. This is a relatively small difference between the two measures of accuracy as the resolution of our images is $0.68 \times 0.68 \times 0.75$ mm. This indicates that the image comparison method we have proposed reliably quantifies the accuracy of the FE model.

The RMS errors for the two different accuracy measures of the FE model were around 2 mm; these measures indicate that the biomechanical model of the breast phantom requires further work to accurately model compression loading. Nevertheless, due to the inaccuracies in modelling the compression of the breast phantom, we were able to validate the image comparison measure described in this chapter by comparing it against feature tracking. The assumptions about the boundary conditions and the material properties of the breast phantom will need to be tested. We modelled the breast phantom using frictional contact constraints with the plates based on observations that the phantom does not slip on the compression plates.

Biomechanical breast models were created for the breasts of two volunteers. For the 32% compression for volunteer 1 (Fig. 7.5), it can be seen that, in order for the model-warped images to best match the clinical images, the 3D model-warped image needs to deform in a downwards-right direction. For the volunteer 2 compressions (Fig. 7.6), it can be seen that for 19% compression the model-warped image generally matches the clinical image (overall RMS error: 3.9 mm). When compression was increased to 38% the error between the two image sets increased slightly, giving an RMS value of 4.1 mm (see Fig. 7.7).

The mismatch between the biomechanical breast models and the clinical data indicates that some modelling assumptions may be inappropriate. We have modelled the breast tissues as homogeneous, incompressible, and isotropic materials. However, breasts are composed of a variety of tissues, such as skin, fat, and fibro-glandular tissues. Thus, we need to explore incorporating mechanical heterogeneity into the model, hence develop techniques to isolate the various types of tissues in the breasts and to determine the material properties of these regions. Also, the contact between the breast tissues and the compression plates is not frictionless; therefore we also need to further investigate these boundary constraints.

While the biomechanical models presented in this chapter do not accurately model the deformations of the breast under compression, the physically realistic constraints inherent in the models may provide a more robust estimate of the initial state for non-rigid registration algorithms. The comparison measure could be extended to perform non-rigid registration by further warping the model-warped images based on the error vector field. In addition, we plan to use the results from our analysis to guide the development of reliable biophysically based breast models that can accurately co-locate features across multiple imaging views and modalities in order to improve clinicians' detection and diagnosis of breast cancer.

References

1. World Health Statistics 2008. Breast cancer: mortality and screening. World Health Organization (WHO), Geneva (2008)
2. Dronkers, D., Hendriks, J., Holland, R., Rosenbusch, G.: The practice of mammography: pathology, technique, interpretation, adjunct modalities. Thieme, Stuttgart (2002)
3. Rueckert, D., Sonoda, L., Hayes, C., Hill, D., Leach, M., Hawkes, D.: Nonrigid registration using free-form deformations: application to breast MR images. IEEE Transactions on Medical Imaging, 18(8), 712–721 (1999)
4. Sivaramakrishna, R.: 3D Breast image registration – a review. Technology in Cancer Research and Treatment, 4(1), 39–48 (2005)
5. Azar, F., Metaxas, D., Schnall, M.: A finite element model of the breast for predicting mechanical deformations during biopsy procedures. In: IEEE Workshop on Mathematical Methods in Biomedical Image Analysis. Los Alamita, CA, pp. 38–45 (2000)
6. Qui, Y., Goldgof, D., Li, L., Sarkar, S., Zhang, Y., Anton, S.: Correspondence recovery in 2-view mammography. In: ISBI 2004. IEEE International Symposium on Biomedical Imaging: Nano to Macro, Arlington, VA, pp. 197–200 (2004)
7. Tanner, C., Schnabel, J., Hill, D., Hawkes, D., Leach, M., Hose, R.: Factors influencing the accuracy of biomechanical breast models. Medical Physics, 33(6), 1758–1769 (2006)
8. Ruiter, N., Stotzka, R., Muller, T., Gemmeke, H., Reichenbach, J., Kaiser, W.: Model-based registration of X-ray mammograms and MR images of the female breast. IEEE Transaction on Nuclear Science, 53(1), 204–211 (2006)
9. Chung, J., Rajagopal, V., Nielsen, P., Nash, M.: Modelling mammographic compression of the breast. In: MICCAI 08. LNCS 5242, pp. 758–765 (2008)
10. Rajagopal, V., Lee, A., Chung, J., Warren, R., Highnam, R., Nash, M., Nielsen, P.: Creating individual-specific biomechanical models of the breast for medical image analysis. Academic Radiology, 15(11), 1425–1436 (2008)
11. Periaswamy, S., Weaver, J., Healy, D., Kostelec, P.: Automated multiscale elastic image registration using correlation. In: SPIE Medical Imaging 3661. pp. 828–838 (1999)
12. Lee, A., Rajagopal, V., Chung, J., Bier, P., Nielsen, P., Nash, M.: Biomechanical modelling for breast image registration. In: SPIE Medical Imaging 6918, 69180U-1 (2008)
13. Chung, J.: Modelling mammographic mechanics. PhD Thesis, University of Auckland (2008)

Chapter 8
Can Vascular Dynamics Cause Normal Pressure Hydrocephalus?

Tonmoy Dutta-Roy, Adam Wittek, and Karol Miller

Abstract This study investigated the hypothesis that changes in the brain vasculature system can explain the mechanics of normal pressure hydrocephalus (NPH) growth. A generic 3-D mesh of a healthy human brain was created. We used a fully non-linear (geometric, constitutive and boundary conditions) 3-D model of the brain parenchyma. The brain parenchyma was modelled as a nearly incompressible, single-phase continuum. A hyperelastic constitutive law and finite deformation theory described the deformations within the brain parenchyma. The brain vasculature system was modelled biomechanically by modifying the relaxed shear modulus according to the cardiac cycle to produce a time varying shear modulus. As no study currently exists on the effects of vasculature on brain parenchyma material properties, a parametric investigation was conducted by varying the brain parenchyma relaxed shear modulus. It is widely believed that no more than 1 mm of Hg (133.416 Pa) transmantle pressure difference is associated with NPH. Hence, we loaded the brain parenchyma with 1 mm of Hg transmantle pressure difference to investigate this suggestion. Fully non-linear, implicit, quasi-static finite element procedures in the time domain were used to obtain the deformation of the brain parenchyma and the ventricles. The results of the simulations showed that 1 mm of Hg (133.416 Pa) did not produce the clinical condition of NPH, even with brain vasculature effects taken into account. We conclude from our work that it is highly unlikely for a phenomenon, such as the brain vasculature effects due to the cardiac cycle, which occurs many times a minute to be able to influence an event such as NPH which presents itself over a time scale of hours to days. We further suggest that the hypothesis of a purely mechanical basis for NPH growth needs to be revised.

Keywords Normal pressure hydrocephalus · Vascular · Brain · Biomechanics

T. Dutta-Roy (✉)
School of Mechanical Engineering, The University of Western Australia, Crawley, WA 6009, Australia
e-mail: tduttar@mech.uwa.edu.au

1 Introduction

A lot of effort is made to understand the phenomenon of normal pressure hydro-cephalus (NPH), but it continues to perplex clinicians. Enhanced diagnosis method-ologies for NPH have evolved but these methods offer limited understanding of NPH growth mechanics. NPH generally occurs in individuals over the age of 60 and clinically presents itself in a classical triad of symptoms: ataxia of the gait, urinary incontinence and dementia. The MRI of the NPH patient shows enlarged ventricular volume with lack of sulcal enlargement. It is estimated that NPH occurs in 5–10% of the population above 60.

It is widely believed that NPH has biomechanical causes [1–9]. The bulk flow theory for development of NPH [1] was investigated using mathematical mod-els [1–9], but these models are unable to co-relate their findings with clinical observations [10]. Clinical techniques used to enhance the diagnosis of NPH [11–15] indicated that there is abnormal vasculature dynamics in patients with NPH. Therefore, in our current work, we used a biomechanical approach to model the brain vasculature system and investigated the suggestion that changes in the brain vasculature system contributed to NPH growth.

In Section 2, we discuss the biomechanical model and detail the mechanistic model of vasculature dynamics. The results of our calculations are summarised in Section 3 followed by discussion and conclusions in Section 4.

2 Biomechanical Model

2.1 Brain Mesh and Material Properties

Figure 8.1 shows the brain mesh for a healthy human brain. The reader is referred to our previous work [10] for detailed description of the brain mesh. We used a hyperelastic [16] constitutive model for the brain parenchyma [8, 10, 17]:

$$W = \frac{2\mu_\infty}{\alpha^2}(\lambda_1^\alpha + \lambda_2^\alpha + \lambda_3^\alpha - 3) + \frac{1}{D_1}(J^{el} - 1)^2. \tag{1}$$

where W is the potential function, μ_∞ is the relaxed shear modulus, α is the material coefficient which can assume any real value without any restrictions, λ_i's are the principal stretches, J^{el} is the elastic volume ratio and D_1 is the material coefficient related to the initial bulk modulus (K_0). The brain parenchyma material parameters are summarised in Table 8.1 [8, 10, 17].

We used a fully non-linear (geometric, constitutive and boundary conditions) 3-D model of the brain parenchyma. It is widely believed that no more than 1 mm of Hg transmantle pressure difference [6, 18] is associated with NPH. Therefore, we loaded the brain parenchyma with 1 mm of Hg transmantle pressure dif-ference [6, 18] to investigate this suggestion. We showed in our previous work
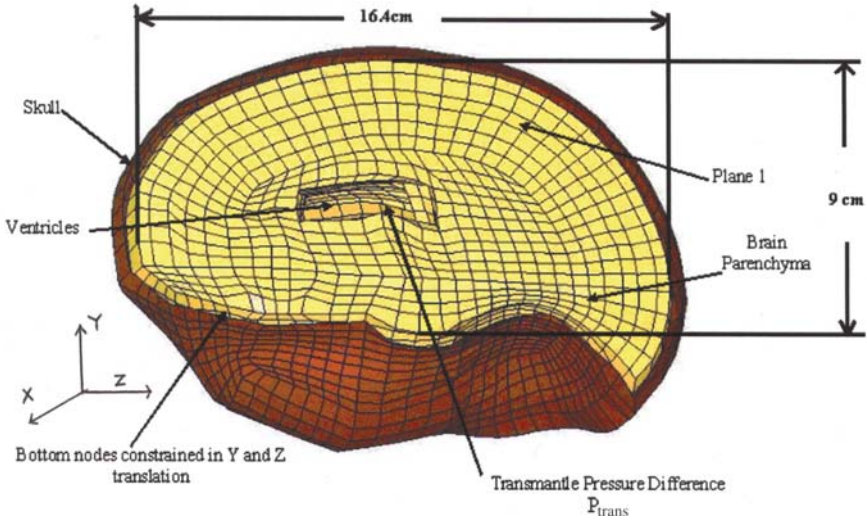
Fig. 8.1 Brain geometry, pressure loading and applied boundary conditions for the brain (3D mesh)

Table 8.1 Material properties for the brain parenchyma (μ_∞ adapted [8, 10,17]; E_∞ (relaxed Young's modulus) and K_∞ (relaxed bulk modulus) are calculated from standard formulae)

Poisson's ratio (υ)	μ_∞ (Pa)	E_∞ (Pa)	K_∞ (Pa)	α
0.49	155.77	464.19	7,736.5	−4.7

[10] that under equal transmantle pressure difference load, there were no significant differences between the computed ventricular volumes for biphasic [19] and nearly incompressible, single-phase model of the brain parenchyma. Consequently, in our current work, we model the brain parenchyma as nearly incompressible, single-phase continua [Poisson's ratio (υ) = 0.49].

2.2 Brain Model Boundary Conditions

Due to approximate symmetry of the brain about the mid-sagittal axis, we used half of the brain in our simulations. Nodes on Plane 1 (Fig. 8.1) had symmetric boundary conditions in the YZ plane (no motion allowed for X translation) applied to them. As the brain was resting in the skull, we constrained all nodes at the bottom of the brain in Y and Z translation (Fig. 8.1). Following Wittek et al. [20], we constrained the nodes on the outer surface of the brain by a frictionless, finite sliding, node-to-surface penalty contact between the brain and the skull. We accounted for subarachnoids' space by introducing a 3 mm gap between the brain outer surface and the skull [20].

2.3 Brain Parenchyma Vasculature Model

Czosnyka and Pickard [13] and Czosnyka et al. [14] indicated that abnormal vasculature dynamics is present in patients with NPH. We investigated the suggestion that changes in the brain vasculature system contributed to NPH growth. During systolic part of the cardiac cycle, the heart pumps in blood through the vascular tree whereas in the diastolic part, the blood recedes through it. As a result, the brain parenchyma is stiffer during systolic part as compared to the diastolic part. We implemented this effect of the brain vasculature by a time varying shear modulus.

Ogden type, hyperelastic constitutive model of the brain parenchyma [10, 17, 21] was implemented using the HYPERELASTIC function [22]. It does not provide for variation of the shear modulus with time. However, it allows for variation of shear modulus as a function of the field variable associated with temperature [22]. This property of the HYPERELASTIC function [22] was used to implement a time varying shear modulus. We first changed the temperature field variable with time using a fully coupled thermal-stress analysis (COUPLED TEMPERATURE DISPLACEMENT procedure) [22]. The thermal conductivity, expansion and heat flux going into and out of the brain parenchyma were set to zero. Hence, no thermal stresses were generated as the temperature field variable was changed with time and the thermo-elastic response of the brain parenchyma was negligible. As a result of the fully coupled thermal-stress analysis, a time varying temperature field distribution was set up. Thereafter, we specified the brain parenchyma material properties (shear and bulk modulus) for each value of the temperature field distribution (Table 8.2) using the HYPERELASTIC function [22]. As the temperature field increased with time and the shear modulus varied with temperature, a time varying

Table 8.2 Time varying shear modulus function and computed ventricular volumes under 1 mm of Hg transmantle pressure difference [6, 10, 18]: μ_∞=155.77 Pa is the relaxed shear modulus [8, 10], ω is the heart rate frequency (72 beats/min or 7.5 rad/s)

Time varying shear modulus (The relaxed shear modulus (μ_∞) was modified according to the cardiac cycle taken from Linninger et al. [15])	Computed ventricular volume (cm^3)	Load application time period (s)
Case 1: $\mu_\infty = \mu_\infty + \mu_\infty[1.3 + \sin(\omega t - \frac{\pi}{2}) - \frac{1}{2}\cos(2\omega t - \frac{\pi}{2})]$	32.7	600
Case 2: $\mu_\infty = \mu_\infty + \mu_\infty[1.3 + \sin(\omega t - \frac{\pi}{2}) - \frac{1}{2}\cos(2\omega t - \frac{\pi}{2})]$	32.6	60
Case 3: $\mu_\infty = \mu_\infty + 0.5\mu_\infty[1.3 + \sin(\omega t - \frac{\pi}{2}) - \frac{1}{2}\cos(2\omega t - \frac{\pi}{2})]$	34	60
Case 4: $\mu_\infty = \mu_\infty + 0.25\mu_\infty[\sin(\omega t - \frac{\pi}{2}) - \frac{1}{2}\cos(2\omega t - \frac{\pi}{2})]$	43.7	60
Case 5: $\mu_\infty = \mu_\infty + 0.5\mu_\infty[\sin(\omega t - \frac{\pi}{2}) - \frac{1}{2}\cos(2\omega t - \frac{\pi}{2})]$	59.5	60
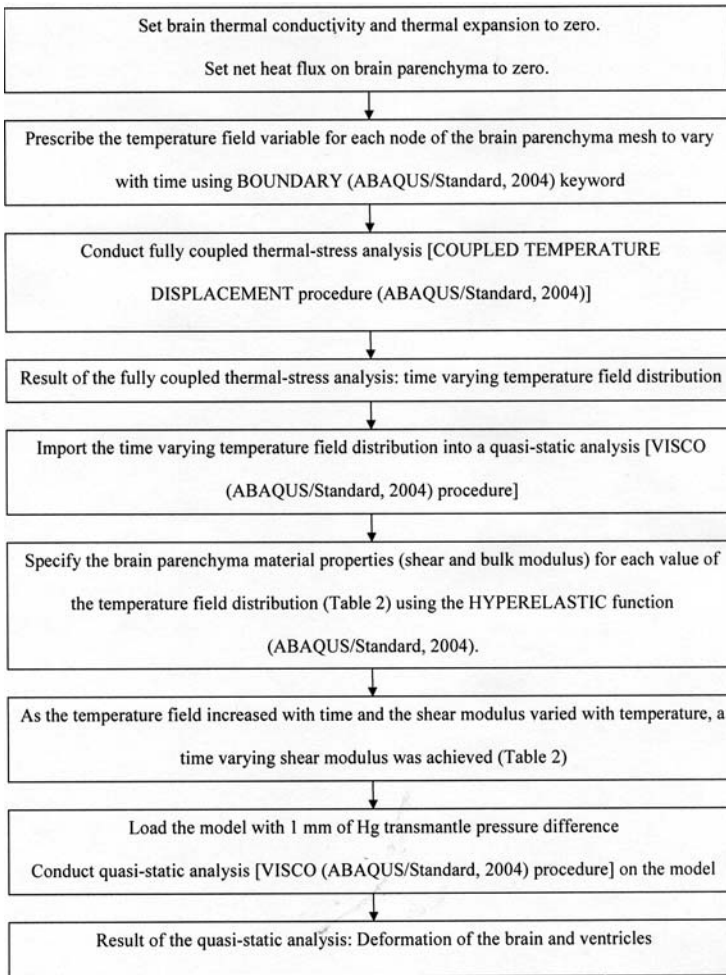
Fig. 8.2 Methodology used for implementing time varying shear modulus

shear modulus was achieved with this technique. The method is summarised as a block diagram in Fig. 8.2.

As no study currently exists on the effects of vasculature on brain parenchyma material properties, a parametric investigation was conducted by varying the brain parenchyma relaxed shear modulus. The relaxed shear modulus (μ_∞) was modified according to the cardiac cycle (taken from Linninger et al. [15]) (Table 8.2) and a time varying shear modulus (Fig. 8.3) was produced. Material strain rate effects are absent for the hyperelastic material law we used for the brain parenchyma. But, in our work, the relaxed shear modulus (μ_∞) was varied with time (Table 8.2). Thus, a quasi-static solution was needed and the VISCO (ABAQUS/Standard) [22]
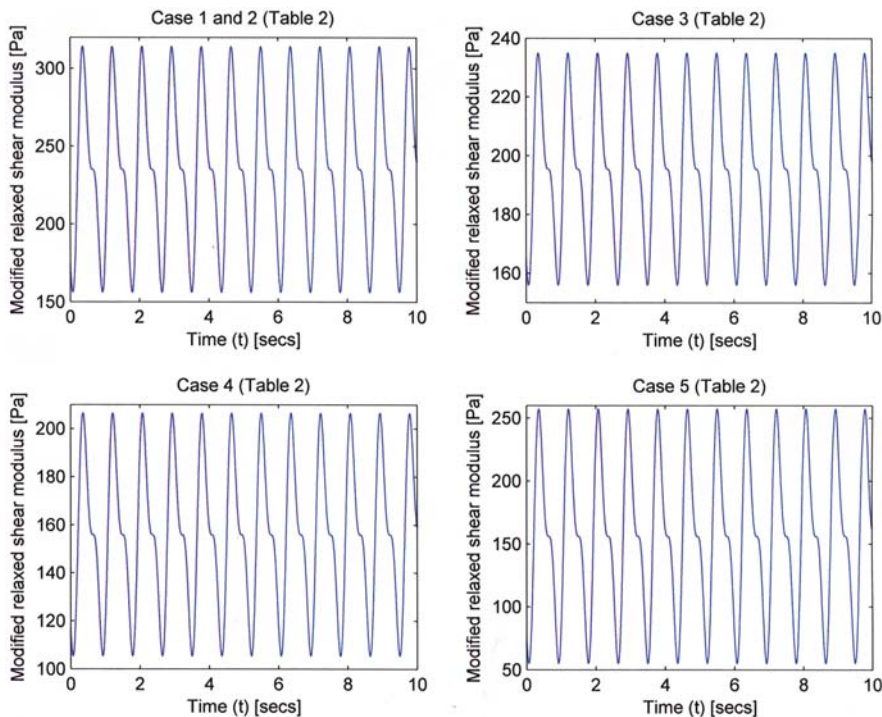
Fig. 8.3 Sinusoidal time varying shear modulus (Table 8.2 [15])

procedure was used to solve the model of NPH. As mentioned earlier, we loaded the brain parenchyma with 1 mm of Hg transmantle pressure difference [6, 10, 18] and the load was applied over the time periods summarised in Table 8.2.

NPH generally develops over 4 days [2]. However, computing our model over the time period taken for development of NPH would require enormous computational resources. As strain rate dependency was not included in our model, the results of our computations should not differ if we apply the pressure load over 4 days, 100 min or 60 s. To confirm this, we applied the load over 600 and 60 s for Cases 1 and 2. For Cases 1 and 2 (Table 8.2), there was practically no difference between computed ventricular volumes. Hence for Cases 3–5 (Table 8.2), the transmantle pressure difference load was applied over 60 s.

3 Results

Computed ventricular volumes for time varying shear modulus are presented in Table 8.2. NPH develops when the ventricular volume increased from 14 cm^3 to

more than 58 cm^3 [23]. One millimetre of Hg transmantle pressure difference cannot produce NPH for Cases 1–4 (Table 8.2), even with brain vasculature effects taken into account. For Case 5, NPH was produced.

4 Discussions and Conclusions

For Cases 1–4 (Table 8.2), 1 mm of Hg transmantle pressure difference load did not produce NPH even with brain vasculature effects taken into account. The period of the cardiac cycle is multiple orders of magnitude smaller than the time taken for clinical development of NPH (hour to days). Even after applying the transmantle pressure difference load quickly, over a smaller time scale (60 s), we could not produce NPH (Table 8.2, Case 1–4). However, for Case 5 (Table 8.2), as the modified relaxed shear modulus varied sinusoidally, it decreased to a low value (55 Pa) for short time period. This combined with increasing transmantle pressure difference load produced NPH. If a biological phenomenon exists which reduces the brain parenchyma material parameters to a low value (e.g. 55 Pa), even for a short period of time, then development of NPH is plausible.

In conclusion, our work showed that the transmantle pressure difference of up to 1 mm of Hg (133.416 Pa) could not produce the clinical condition of NPH, even with brain vasculature effects taken into account. Following our results, we argue that it is highly unlikely for a phenomenon which occurs many times a minute (in our case: brain vasculature effects due to the cardiac cycle), to be able to influence an event such as NPH which presents itself over a time scale of hours to days. The results presented in our current work taken together with our previous paper [10] add strength to the suggestion that the hypothesis of a purely mechanical basis for NPH growth needs to be revised.

References

1. Hakim, S.: Biomechanics of hydrocephalus. Acta Neurologica LatinoAmericana, 1(Suppl 1), 169–194 (1971)
2. Nagashima, T., Tamaki, N., Matsumoto, S., Horwitz, B., Seguchi, Y.: Biomechanics of hydrocephalus: a new theoretical model. Neurosurgery, 21(6), 898–904 (1987)
3. Tada, Y., Matsumoto, R., Nishimura, Y.: Mechanical modelling of the brain and simulation of the biomechanism of hydrocephalus. JSME International Journal I-Solid Mechanics 33(2), 269–275 (1990)
4. Kaczmarek, M., Subramaniam, R.P., Neff, S.R.: The hydromechanics of hydrocephalus: steady-state solutions for cylindrical geometry. Bulletin of Mathematical Biology, 59(2), 295–323 (1997)
5. Tenti, G., Sivaloganathan, S., Drake, J.M.:. Brain biomechanics: steady-state consolidation theory of hydrocephalus. Canadian Applied Math Quarterly, 7, 93–110 (1999)

6. Penn, R.D., Max, C.L., Linninger, A.A., Miesel, K., Lu, S.N., Stylos, L.: Pressure gradients in the brain in an experimental model of hydrocephalus. Journal of Neurosurgery, 102, 1069–1075 (2005)
7. Tenti, G., Drake, J.M., Sivaloganathan, S.: Brain biomechanics: mathematical modelling of hydrocephalus. Neurological Research, 22, 19–24 (2000)
8. Taylor, Z., Miller, K.: Reassessment of brain elasticity for analysis of biomechanisms of hydrocephalus. Journal of Biomechanics, 37, 1263–1269 (2004)
9. Momjian, S., Bichsel, D.: Non linear poroplastic model of ventricular dilation in hydrocephalus. Journal of Neurosurgery, 109(1), 100–107 (2008)
10. Dutta-Roy, T., Wittek, A., Miller, K.: Biomechanical modelling of normal pressure hydrocephalus. Journal of Biomechanics, 41(10), 2263–2271 (2008)
11. Shulman, K., Marmarou, A.: Analysis of intracranial pressure in hydrocephalus. Developmental Medicine and Child Neurology, Suppl 16, 11–16 (1968)
12. Marmarou, A., Shulman, K., Rosende, R.M.: A non-linear analysis of CSF system and intracranial pressure dynamics. Journal of Neurosurgery, 48, 332–344 (1978)
13. Czosnyka, M., Pickard, J.D.: Monitoring and interpretation of intracranial pressure. Journal of Neurology, Neurosurgery Psychiatry, 75, 813–821 (2004)
14. Czosnyka, M., Czosnyka, Z., Momjian, S., Pickard, J.D.: Cerebrospinal fluid dynamics. Physiological Measurement, 25(5), R51–R76 (2004)
15. Linninger, A.A., Tsakiris, C., Zhu, D.C., Xenos, M., Roycewicz, P., Danziger, Z., Penn, R.: Pulsatile cerebrospinal fluid dynamics in the human brain. IEEE Transactions Bio-medical Engineering, 52(4), 557–565 (2005)
16. Ogden, R.W.: Non-linear elastic deformations. Ellis Horwood Ltd., Chichester, Great Britain (1984)
17. Miller, K., Chinzei, K.: Mechanical properties of brain tissue in tension. Journal of Biomechanics, 35, 483–490 (2002)
18. Czosnyka, M.: Personal Communication (2006)
19. Cheng, S., Bilston, L.E.: Unconfined compression of white matter. Journal of Biomechanics, 40, 117–124 (2007)
20. Wittek, A., Miller, K., Kikinis, R., Warfield, S.K.: Patient-specific model of brain deformation: application to medical image registration. Journal of Biomechanics, 40, 919–929.
21. Miller, K., Chinzei, K.: Constitutive modelling of brain tissue: experiment and theory. Journal of Biomechanics, 30, 1115–1121 (1997)
22. ABAQUS/Standard: Version 6.5.4, Hibbit, Karlsson & Sorenson, Inc. (2004)
23. Matsumae, M., Kikinis, R., Mórocz, I., Lorenzo, A.V., Albert, M.S., Black, P.M., Jolesz, F.A.: Intracranial compartment volumes in patients with enlarged ventricles assessed by magnetic resonance-based image processing. Journal of Neurosurgery, 84, 972–981 (1996)

Part II
Computational Biomechanics of Tissues of Musculoskeletal System

Chapter 9
Computational Modelling of Human Gait: Muscle Coordination of Walking and Running

Marcus Pandy

Abstract Walking is a task that most people perform with ease. Although seemingly simple, it is an extraordinarily complex skill that takes years to develop. The various actions of the leg muscles are exquisitely timed to provide support against gravity, maintain forward progression, and control balance from step to step. Many experiments have been undertaken to better understand the biomechanics of gait, yet little is currently known about the way individual muscles coordinate body movement, primarily because experiments provide very limited information on muscle function. This applies even for walking at the preferred speed, and virtually nothing is known about individual muscle function under other conditions, such as walking and running at different speeds.

Biomechanical computer modelling has risen to new heights in recent years, mainly because of the belief that this approach can yield new insights into how the neuromuscular and musculoskeletal systems interact during daily physical activity. Recent advances in imaging technology, numerical modelling techniques, and computing power have enabled elaborate models of the body to be built for the purpose of studying tissue function in vivo. In this presentation, I review how the structure of the neuromusculoskeletal system is commonly represented in a multi-joint model of movement; how musculoskeletal modelling may be combined with optimization and nonlinear control theory to simulate the dynamics of human gait; and how model output can be analysed to describe and explain leg-muscle function during locomotion.

Keywords Biomechanics · Gait · Muscle coordination

M. Pandy (✉)
Department of Mechanical Engineering, University of Melbourne, Melbourne, Australia
e-mail: pandym@unimelb.edu.au

Chapter 10
Influence of Smoothing on Voxel-Based Mesh Accuracy in Micro-Finite Element

Thibaut Bardyn, Mauricio Reyes, Xabier Larrea, and Philippe Büchler

Abstract The interest in automatic volume meshing for finite element analysis (FEA) has grown more since the appearance of microfocus CT (μCT), due to its high resolution, which allows for the assessment of mechanical behaviour at a high precision. Nevertheless, the basic meshing approach of generating one hexahedron per voxel produces jagged edges. To prevent this effect, smoothing algorithms have been introduced to enhance the topology of the mesh. However, whether smoothing also improves the accuracy of voxel-based meshes in clinical applications is still under question. There is a trade-off between smoothing and quality of elements in the mesh. Distorted elements may be produced by excessive smoothing and reduce accuracy of the mesh. In the present work, influence of smoothing on the accuracy of voxel-based meshes in micro-FE was assessed. An accurate 3D model of a trabecular structure with known apparent mechanical properties was used as a reference model. Virtual CT scans of this reference model (with resolutions of 16, 32 and 64 μm) were then created and used to build voxel-based meshes of the microarchitecture. Effects of smoothing on the apparent mechanical properties of the voxel-based meshes as compared to the reference model were evaluated. Apparent Young's moduli of the smooth voxel-based mesh were significantly closer to those of the reference model for the 16 and 32 μm resolutions. Improvements were not significant for the 64 μm, due to loss of trabecular connectivity in the model. This study shows that smoothing offers a real benefit to voxel-based meshes used in micro-FE. It might also broaden voxel-based meshing to other biomechanical domains where it was not used previously due to lack of accuracy. As an example, this work will be used in the framework of the European project ContraCancrum, which aims at providing a patient-specific simulation of tumour development in brain and lungs for oncologists. For this type of clinical application, such a fast, automatic, and accurate generation of the mesh is of great benefit.

T. Bardyn (✉)
Institute for Surgical Technology & Biomechanics, University of Bern, Bern, Switzerland
e-mail: thibaut.bardyn@istb.unibe.ch

1 Introduction

The high impact of osteoporosis on medical costs has made it a major branch of biomechanics. The development of new technology such as the micro-CT and, subsequently, of high-resolution finite element studies has increased the understanding of this condition. The effects of new treatments on microscopic bone properties or prediction of fracture can be assessed with these methods for example.

However, the creation of the highly complex meshes used in the finite element analysis is a challenge. The voxel-based method is the easiest way to build such a mesh. In brief, it consists of associating a voxel representing bone with a cubic element in the mesh. Although these models are fast and automatic, the surfaces generated are composed of jagged edges. This is problematic for simulations, since stress concentrations may appear at sharp corners. Consequently the accuracy of these models can be low as compared to other methods [1].

One solution to improve the aspect of these models is to smooth its external surface. Smoothing of voxel-based FE meshes has been shown to improve accuracy in the simple case of a sphere [2]. However, the effect of this smoothing in real biomechanical applications, such as retrieval of bone structural properties, has never been tested.

Therefore, the aim of this work is to assess the effect of smoothing on the accuracy of voxel-based mesh as compared to a reference model.

2 Methods

The influence of the degree of smoothing on the accuracy of finite element was evaluated by measuring the apparent Young's modulus of a trabecular structure. Results obtained with a reference model were compared to voxel-based models with different degrees of smoothing.

2.1 Creation of the Reference Model

A trabecular bone specimen from a human vertebra was scanned in the axial plane with a high-resolution scanner (Scanco μCT40, Scanco Medical AG, Switzerland). The voxels had a dimension of 8 μm in every direction. The CT scan obtained was segmented (Amira, Visage Imaging GmbH, Germany) and an accurate 3D model with 1,286,444 triangles was generated. The triangular surface mesh of the trabecular bone was then processed further in a CAD program and fitted with a
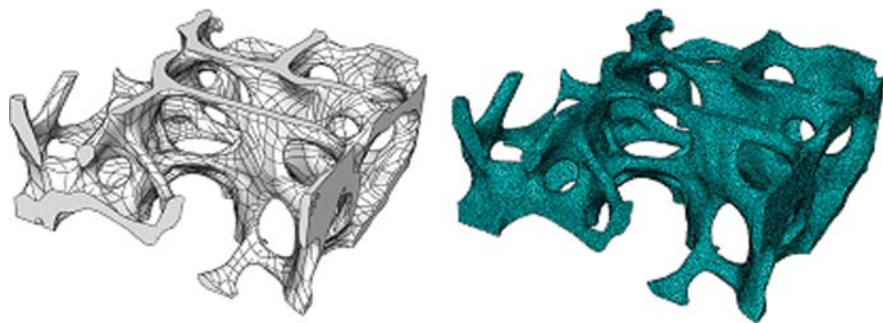
Fig. 10.1 (*Left*) NURBS and (*right*) quadratic tetrahedral element mesh used as reference model for the study

set of higher-order mathematical surfaces, e.g. NURBS (Non-Uniform Rational B-Splines). The smooth model of the trabecular structure obtained was considered as the reference geometry (Fig. 10.1).

The NURBS model obtained was imported into a commercial finite element software (ABAQUS, Simulia, USA) and a volumetric finite element mesh with quadratic tetrahedral elements was generated. To assess the accuracy of this reference model, a convergence study with different mesh densities was performed. Total strain energy of the mesh under an axial loading was evaluated and compared. Meshes with a number of elements ranging from 28,537 to 919,780 were tested. Following this convergence study, a mesh with 559,814 quadratic tetrahedral elements was chosen as the reference model.

2.2 Creation of the Voxel-Based Mesh

In order to compare the reference model with voxel-based meshes, a virtual CT scan of the NURBS geometry was created using Amira. Resolution of the virtual CT scan was similar to the original one (8 μm voxel size). The CT scan was resampled at voxel sizes of 16, 32, and 64 μm, producing voxel-based meshes of 231,071, 29,169, and 3,529 elements, respectively. These resolutions are typically used for in vivo micro-CT.

2.3 Smoothing

The outer surface of the mesh was extracted and smoothed according to the geometric signal processing approach presented in [3]. Let the column vector x be the vector of either the first, second, or third coordinates of the vertices. The Laplacian operator is defined on this graph signal by

$$\Delta x_i = \sum_{j \in i^*} w_{ij} \left(x_j - x_i \right) \tag{1}$$

with i^* being the neighbourhood of the vertex i and w_{ij} the weights of the operator. The Laplacian operator can be written under a matrix form

$$\Delta x = -Kx \tag{2}$$

with $K = I - W$, $W = (w_{ij})$, and with its elements equal to zero if j is not a neighbour of i. The eigenvectors e^j of the matrix K define the natural vibration mode of the graph and form a basis of a n-dimensional space in which the signal x can be decomposed as

$$x = \sum_{i=1}^{n} \hat{x}_j e_j \tag{3}$$

This formulation is equivalent to the discrete Fourier transform of the signal x. The smoothing of the surface is then performed by applying a low-pass filter with transfer function $f(K)$:

$$x' = f(K)\, x = \sum_{i=1}^{n} (k_i)\, x_i \cdot e_i \tag{4}$$

with $0 \le k_1 \le k_2 \le \cdots \le k_n \le 2$ being the eigenvalues of the matrix K. The window sync low-pass filtering transfer function is then approximated using Chebyshev polynomials:

$$T_n(w) = \begin{cases} 1 & n = 0 \\ w & n = 1 \\ 2wT_{n-1}(w) - T_{n-2}(w) & n > 1 \end{cases} \tag{5}$$

The advantages of using this approximation are that the terms of the polynomial are orthogonal, it needs small storage capacities (i.e. three-term storage), it is numerically stable, and it can be defined for volume preservation purposes.

Smoothing was performed up to a passband frequency of $k = 0.03$. Further smoothing induced negative volume elements.

2.4 Prism Division

Extensive smoothing creates distorted elements with large or very small dihedral angles on the surface of the mesh. To improve the quality of the mesh, hexahedral elements bearing a large angle between faces were divided into prism elements
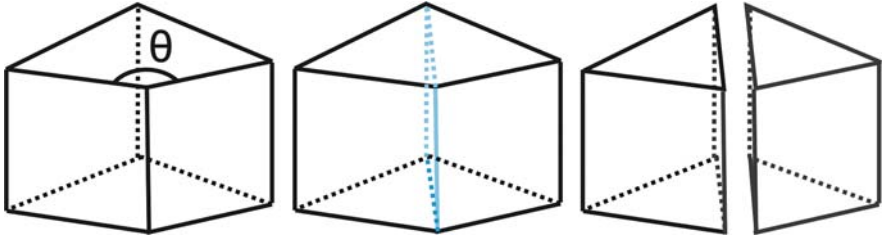
Fig. 10.2 Correction of elements featuring large angles (here represented by θ). The elements are divided into two prism elements along the plane that passes through the "large angle" edge

(Fig. 10.2). If the angle was superior to a certain value, then the edge at the intersection of the two faces was used for the division. The element was divided by the "virtual" plane that joined this edge with its opposite in the element. Improvements were measured by counting the number of distorted elements having interior angles between isoparametric lines less than 45° and greater than 130°. Since it produced the best improvements (trade-off between increase in the number of elements and improvement in general mesh quality), a threshold angle of 130° was chosen for the splitting.

2.5 Finite Element Study

Once the smoothing was performed on the voxel-based mesh, the apparent Young's modulus was calculated in the three directions X, Y, Z, with Z the axis perpendicular to the axial plane of the vertebra. A 1% strain was applied on the top of the structure while the bottom was constrained in the direction of displacement. No other faces were constrained. The apparent Young's modulus E was calculated according to the formula

$$E = \frac{Fl}{\Delta u A} \tag{6}$$

with Δu the applied displacement at the top of the structure, F the reaction force at the moving nodes, l and A, respectively, the length and the area as measured by the external dimensions of the specimen. For all models, element material properties were assumed homogeneous and isotropic with a Young's modulus of 10 GPa and a Poisson ratio of 0.3.

3 Results

Increasing the degree of smoothing improves the mechanical properties of the voxel-based mesh as compared to the reference model (Fig. 10.3). Smoothing significantly improved the apparent Young's modulus of the voxel-based meshes for the 16 and
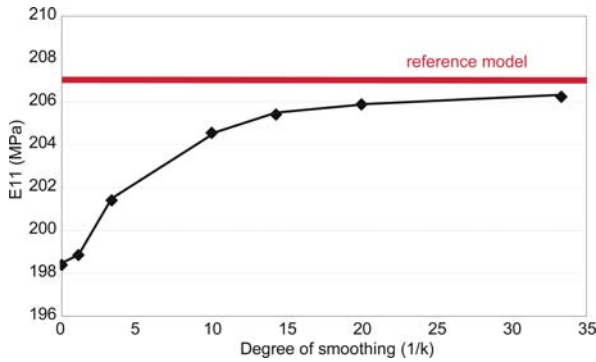
Fig. 10.3 Evolution of the apparent Young's modulus in the X direction for the 16 μm model with different degrees of smoothing

Table 10.1 Error (in percentage of reference value) for apparent Young's modulus between reference model and voxel-based meshes without smoothing and with maximum smoothing. Smoothing was stopped when negative volume elements were created

	16 μm			32 μm			64 μm		
	E_{11}	E_{22}	E_{33}	E_{11}	E_{22}	E_{33}	E_{11}	E_{22}	E_{33}
No smoothing	4.15	3.41	5.74	8.02	15.63	10.71	12.10	33.99	23.19
$k = 0.03$	0.36	0.97	2.17	1.32	8.67	5.19	12.25	32.37	21.44

32 μm resolutions (Table 10.1). Improvements were not significant for the 64 μm resolution. This is due to loss of trabecular connection in the model (Fig. 10.4). Visually, reduction of stress concentration can be observed on the edges of the model (Fig. 10.5). The volume of the model was preserved during the smoothing
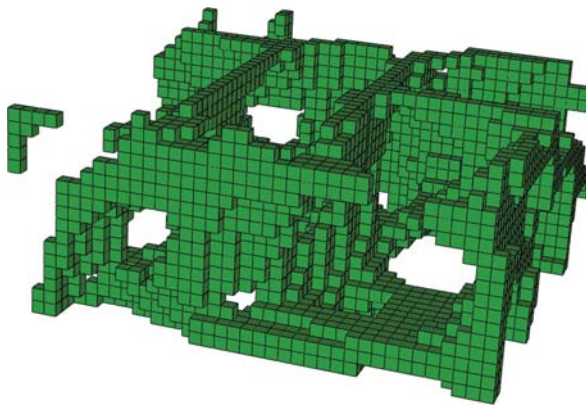
Fig. 10.4 Loss of trabecular connection for the 64 μm model. This phenomenon explains the large error found for the apparent Young's modulus at this resolution
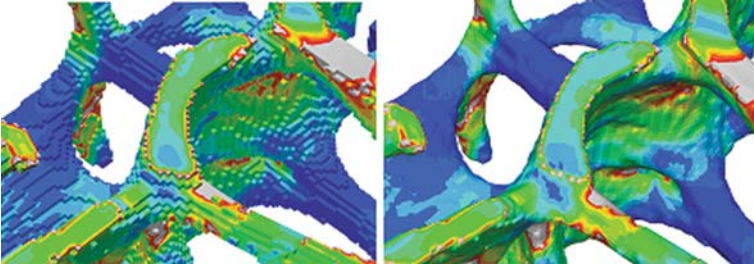
Fig. 10.5 Details of the Mises stress in the trabecular structure generated (*left*) without smoothing and (*right*) with smoothing

and changed only by 0.02% (for $k = 0.03$ and the 16 μm model). In average, creation of the mesh and smoothing took 3 min for the 16 μm model on a regular 2.4 GHz processor with 2.00 GB of RAM.

As expected [4], the Young's modulus in the Z direction ($\approx$572 MPa) was found to be superior to the Young's modulus in the directions parallel to the axial plane of the vertebra ($\approx$260 and 257 MPa, respectively).

Prism division significantly decreased the number of distorted elements (Table 10.2). However, results in terms of accuracy were not significantly changed with this improvement with an average difference of 0.19% $\pm$ 0.17 as compared to the model without prism division. For $k = 0.03$, the number of elements in the 16 μm model was increased by 20% when prism division was used.

Table 10.2 Comparison of the number of distorted elements generated by smoothing with and without prism division. Elements were considered distorted when the interior angles between isoparametric lines was inferior to 45° and superior to 130°

	Number of distorted elements without prism division	Number of distorted elements with prism division
$k = 0.1$	2,449	1
$k = 0.07$	8,173	1
$k = 0.05$	13,569	0
$k = 0.03$	18,901	1

4 Discussion

Voxel-based meshing is the method of choice for micro-FE due to its speed and low complexity. However, it does not represent smooth anatomy with accuracy [1]. Smoothing algorithms have been proposed to improve these meshes [2] but their influence on real anatomical models has never been assessed. Therefore, in this study, the effect of smoothing on the mechanical properties of a voxel-based mesh of bone was tested.

The apparent Young's modulus was significantly improved by smoothing and converged to the reference value. This is in accordance with previous studies on simple models that showed that the accuracy of the finite element meshes was improved by smoothing [1, 2]. With smoothing, voxel-based meshes can reach an accuracy equivalent to more complex tetrahedron models. Results achieved with the smooth 32 μm model were comparable to those obtained with the non-smooth 16 μm. This would suggest that smoothing allows one to reduce the resolution of images and consequently to significantly reduce the number of elements in the mesh. However, the effect of smoothing is relevant only for image resolutions where the connection of the trabeculae is kept intact. In our case, loss of connection happened at a resolution of 64 μm and explains the large errors found for the Y and Z directions [5]. In these cases, smoothing does not correct errors due to unconnected areas. The high dependence on image resolution is one clear limitation of the voxel-based meshes [6]. One solution that was proposed in the literature was to change the threshold used for the segmentation of the CT scan and to compensate for the loss of connected areas by thickening the remaining structure [5]. This was not possible in the present study since virtual CT scans were used. The combination of smoothing and change in the segmentation threshold should be assessed in a future study.

Splitting the distorted elements into prisms significantly improved the quality of the mesh at limited computational costs. Therefore, it was possible to smooth the mesh without concern for the quality of the elements. In existing voxel mesh software (Simpleware, Simpleware Ltd, UK) every element on the surface is unconditionally split into tetrahedra. In our case, elements which are to be split or corrected are discriminated. Hence, the augmentation of elements after division is significantly lower since it only represents a small proportion of elements in the mesh. Moreover, division into prisms generates fewer elements than division into tetrahedra. The fact that improving element quality did not have an influence on result of the analysis may be due to the global aspect of the apparent Young's modulus. Local analyses such as surface strain measurements would clearly be more influenced by element quality [6].

Smoothing was limited to a certain degree, due to generation of negative volume elements. Regularization algorithms that would move interior nodes in order to improve element quality and take smoothing further are currently under investigation. One simple solution to this could also be to remove elements with negative volume (as long as their number is small). However, the question arises: What effect will extensive smoothing have on the accuracy of the model, since it might induce the loss of important geometrical features? In that case, a limit would have to be defined for the smoothing. Future work will also consist of comparing mechanical properties of the mesh with more virtual models but also with real experimental data.

This study shows that smoothing has a real application in voxel-based meshes used in micro-FE. Smooth voxel-based meshes could be used in other applications such as statistical shape models of full bones, for example, where fast and automatic generation of an accurate mesh is of great benefit. Use of voxel-based mesh in these situations has been assessed but did not lead to significant results [6]. Addition of

smoothing would greatly improve the accuracy of these models and allow their use in various domains. For this reason, this algorithm will be used in the European project ContraCancrum which aims to develop an oncosimulator for clinicians. Fast, automatic, and robust algorithms such as presented in this study are particularly adapted for this type of clinical applications.

References

1. Camacho, D.L.A., Hopper, R.H., Lin, G.M., Myers, B.S.: An improved method for finite element mesh generation of geometrically complex structures with application to the skullbase. Journal of Biomechanics, 30, 1067–1070 (1997)
2. Boyd, S.K., Müller, R.: Smooth surface meshing for automated finite element model generation from 3D image data. Journal of Biomechanics, 39, 1287–1295 (2006)
3. Taubin, G., Zhang, T., Golub, G.: Optimal surface smoothing as filter design. Proceedings of the 4th European Conference on Computer Vision. 1064, 283–292 (1996)
4. Liebschner, M.A.K., Kopperdahl, D.L., Rosenberg, W.S., Keaveny, T.M.: Finite element modeling of the human thoracolumbar spine. Spine, 28, 559–565 (2003)
5. Ulrich, D., van Rietbergen, B., Weinans, H., Rüegsegger, P.: Finite element analysis of trabecular bone structure: a comparison of image-based meshing techniques. Journal of Biomechanics, 31, 1187–1192 (1998)
6. Viceconti, M., Bellingeri, L., Cristofolini, L., Toni, A.: A comparative study on different methods of automatic mesh generation of human femurs. Medical Engineering and Physics, 20, 1–10 (1998)

Chapter 11
Biomaterial Surface Characteristics Modulate the Outcome of Bone Regeneration Around Endosseous Oral Implants: In Silico Modeling and Simulation

Nadya Amor, Liesbet Geris, Jos Vander Sloten, and Hans Van Oosterwyck

Abstract Experimental investigations have demonstrated the importance of platelets and their activation for bone regeneration around oral implants. This study aimed to numerically demonstrate the key role of activated platelets which is controlled by implant surface characteristics. The cellular activities involved in the process of peri-implant endosseous healing can be represented by migration, proliferation, differentiation, removal, extracellular matrix synthesis and degradation, and growth factor production/release and decay. These activities are described by a system of highly coupled non-linear partial differential equations of taxis–diffusion–reaction type. Moreover, cell–biomaterial interactions were treated by including surface-specific model parameters. A well-designed in vivo model that looked at healing around oral implants with different surface properties was selected from literature to validate the results. Numerical simulations agreed well with the experimentally observed healing response and demonstrated that platelet-related model parameters, which were dependent on implant surface characteristics, modulate the pattern of healing.

Keywords Mathematical modeling · Numerical simulation · Blood platelet · Bone regeneration · Biomaterial · Peri-implant endosseous healing

1 Introduction

Biomaterial surface characteristics play an important role in orchestrating the sequence of events during peri-implant bone regeneration, such as in the case of endosseous oral implants [1]. Experimental investigations on blood–biomaterial interactions have demonstrated the importance of platelets and their activation on a biomaterial surface, being influenced by implant surface characteristics [2, 3]. Platelets, once activated, release local factors that contribute to the wound healing

N. Amor (✉)
Division of Biomechanics and Engineering Design, Department of Mechanical Engineering, Katholieke Universiteit Leuven, Heverlee 3001, Leuven, Belgium
e-mail: nadya.amor@gmail.com

response [3, 4]. These factors play a crucial role in determining which cells are recruited and how the early phases of differentiation occur [5].

Numerous in vivo studies using a wide range of animal models and titanium implants with different designs [6–9] have been carried out to provide a clear comprehension of the healing process. The crucial aim of these experimental investigations was to see whether bone apposition could be enhanced on the implant surfaces. A higher amount of bone-to-implant contact has been observed on "microrough" sandblasted/acid-etched versus "smooth" turned implant surfaces [8]. This amount could further be increased by chemically modifying sandblasted/acid-etched implant surfaces [6, 9]. The combination of both surface composition and microroughness has been shown to considerably influence the amount of bone-to-implant contact.

In vitro examinations have been widely used to investigate the response to biomaterial surfaces for various cell types such as fibroblasts [10], epithelium [11] and osteoblast-like cells (MG63) [12, 13]. It has been demonstrated that MG63 cells exhibit reduced cell proliferation, but increased osteogenic differentiation (such as increased osteocalcin expression) and growth factor production (such as latent TGF-β) when grown on microrough versus smooth titanium substrates [13].

Mathematical modeling can contribute to an integrated understanding of the phenomena that occur during peri-implant endosseous healing. In our previous work [14] we demonstrated that a mathematical model developed for bone fracture healing [15, 16] was able to represent some aspects of peri-implant endosseous healing as described by Davies [17, 18] as long as cartilage formation was not predicted. This model incorporated cellular activities, such as mesenchymal cell migration, proliferation, differentiation, degradation and synthesis of fibrous tissue extracellular matrix and bone extracellular matrix, and osteogenic growth factor diffusion, production, and decay. In this study, this model will be extended by including the effect of activated platelets and the influence of biomaterial surface characteristics on cell behavior.

The first objective of the current study is to see whether the extended model can predict relative differences between two different implant surfaces for a specific in vivo model of peri-implant healing. Hence, a well-designed experimental animal model [8] that looked at the healing around titanium implants with different surface roughnesses is selected and serves to validate the predicted results. As cell–biomaterial interactions are concerned, the model parameters that reflect this influence are identified and modulated based on a well-designed algorithm. The second objective of this study is to perform a sensitivity analysis of the model parameters and the initial condition that are related to the activated platelets.

2 Materials and Methods

2.1 Mathematical Model Formulation

In the process of peri-implant endosseous healing, cells are involved in a complicated feedback control system that includes numerous growth factors and a lengthy

list of signaling molecules [19]. The major activities of the cells can concisely be represented by migration, proliferation, differentiation, removal (or apoptosis), extracellular matrix synthesis and degradation, and growth factor production, release, and decay. The elaborated mathematical model that incorporates such cellular activities formulated by functional forms and/or constants is explained in detail in [14]. Briefly, the extended version of this mathematical model is represented by a system of six coupled non-linear partial differential equations of taxis–diffusion–reaction type governing the change of activated platelet density (platelets ml^{-1}), the densities of two tissue-forming cells (cells ml^{-1}), namely mesenchymal stem cells and osteoblasts, the densities of bone extracellular matrix and fibrous extracellular matrix (g ml^{-1}), and the concentration of one generic osteogenic growth factor (ng ml^{-1}). The rates of change of these dependent variables in a compact form are as follows:

$$\frac{\partial c_m\left(t,\overrightarrow{x}\right)}{\partial t} = \nabla.\left[D_{cm}\left(\overrightarrow{c}\right)\nabla c_m - c_m\sum_{i=1}^{5}f_i\left(\overrightarrow{c}\right)\nabla c_i\right] + f_0\left(c_m,\overrightarrow{c}\right), \quad (1)$$

$$\frac{\partial\overrightarrow{c}\left(t,\overrightarrow{x}\right)}{\partial t} = D\Delta\overrightarrow{c} + \overrightarrow{g}\left(c_m,\overrightarrow{c}\right), \quad (2)$$

where time t and coordinates $\overrightarrow{x}$ are the independent variables and $c_m\left(t,\overrightarrow{x}\right)$ represents the density of the mesenchymal stem cells. $\overrightarrow{c}\left(t,\overrightarrow{x}\right)$ represents a vector of five densities or concentrations, namely activated platelets and osteoblast densities, fibrous tissue extracellular matrix density, bone extracellular matrix density, and osteogenic growth factor concentration. $D_{cm}\left(c_m,\overrightarrow{c}\right)$ and D are the diffusion coefficients, $f_i\left(\overrightarrow{c}\right)$ the taxis coefficients (haptotaxis and chemotaxis), and $f_0\left(c_m,\overrightarrow{c}\right)$ and $\overrightarrow{g}\left(c_m,\overrightarrow{c}\right)$ represent the reaction terms. More particularly, the differential equations that represent the evolution of activated platelets and of the osteogenic growth factor are as follows:

$$\frac{\partial c_{ap}}{\partial t} = -\overbrace{\lambda_{cap}\,c_{ap}}^{\text{degradation}}, \quad (3)$$

$$\frac{\partial g_b}{\partial t} = \overbrace{\nabla\left[D_{gb}\nabla g_b\right]}^{\text{diffusion}} + \overbrace{E_{gcb}\,c_b}^{\text{production}} + \overbrace{E_{gcap}\,c_{ap}}^{\text{release}} - \overbrace{d_{gb}\,g_b}^{\text{decay}}, \quad (4)$$

where activated platelets (c_{ap}) are modeled by a degradation process represented by a constant degradation rate (λ_{cap}). The change of the osteogenic growth factor (g_b) is represented by a diffusion process with a constant diffusion coefficient (D_{gb}), a production (E_{gcb}) by osteoblasts (c_b) which depends of the osteogenic growth factor concentration, a release from the activated platelets (c_{ap}) with a constant release rate (E_{gcap}) and, finally, a decay modeled by a constant decay rate (d_{gb}).

2.2 Experimental Model and Geometry of the Wound Compartment

In the experimental model [8], solid screw implants made from commercially pure titanium (Institut Straumann AG) and designed with a U-shaped circumferential trough within the thread region (Fig. 11.1a) presented two different surface configurations: turned ("smooth") and sandblasted/acid-etched (SLA, "microrough") with three-dimensional surface roughness S_a of 0.35 ± 0.17 μm and 2.29 ± 0.59 μm, respectively. They were installed in the alveolar bone of the dog mandible. The primary mechanical stability of the implant was ensured leading to direct bone formation either by *distance osteogenesis* only for the smooth implant surface (turned) or by both *distance* and *contact osteogenesis* for the microrough implant surface (SLA). The early phases of the healing process around these implants were then investigated and assessed within the experimental wound chamber (Fig. 11.1a) for different time points ranging from day 0 (2 h) till 12 weeks. Details about the experimental setup can be found in Berglundh et al. [7] and Abrahamsson et al. [8].
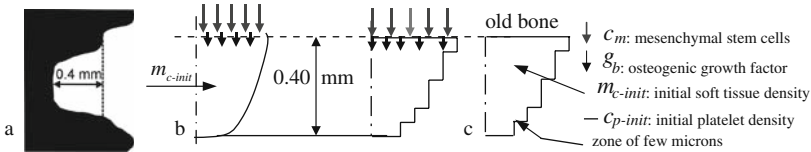
Fig. 11.1 Wound compartment (**a**, reproduced from [8]), idealized (**b**) and further simplified (**c**, used for the simulations) geometrical domain, showing initial and boundary conditions. The thick zone of 5 μm in which the surface-specific parameter values were applied is shown as well (**c**)

A geometrical domain representative of the wound compartment (Fig. 11.1b, c), with a depth of 400 μm, was derived from the experimental wound chamber in which the mathematical model was numerically solved (see Section 2.4).

2.3 Derivation of Surface-Specific Model Parameters

In order to account for the effect of biomaterial surface characteristics (in this case surface roughness) on cell response, model parameter values were modulated in a 5 μm thick zone at the implant surface compared to the rest of the wound compartment (Fig. 11.1c, right). This was done based on in vitro data from Lincks and coworkers [20]. Their study compared the response of osteoblast-like cells (MG63) to microrough versus smooth titanium substrates [20], having roughnesses similar to the surfaces used in [8]. It was found that cell proliferation, as analyzed by assessing cell number and [3][H]-thymidine incorporation decreased for microrough versus smooth titanium substrates. At the same time, osteogenic differentiation (examined by measuring alkaline phosphatase-specific activity and osteocalcin expression), matrix synthesis (collagen and proteoglycan synthesis), and local factor production

(prostaglandin E_2 and latent transforming growth factor-β) were found to increase on microrough versus smooth titanium substrates.

Based on these in vitro findings, two sets of surface-specific model parameter values (one for smooth and one for microrough) can be defined. In addition, a set of parameter values has to be identified for the rest of the wound compartment. In order to do so, the following algorithm is proposed:

Step 1: *Evaluation of the model parameters in the entire wound domain for a smooth implant surface*. These can be obtained by fitting the simulations results to the in vivo data of [8], obtained for the smooth (turned) implant surface. In addition, it is assumed that the smooth implant surface will not substantially affect cell behavior, therefore leading to

$$(params_i)_{wound-smooth} = (params_i)_{impl-smooth} . \tag{5}$$

Step 2: *Evaluation of the model parameters in the entire wound domain for a microrough implant surface*. The values determined in Step 1 were assigned to the model parameters far from the microrough implant surface where the influence of surface microroughness on cell response was assumed to be negligible:

$$(params_i)_{wound-\mu rough} = (params_i)_{wound-smooth} . \tag{6}$$

Step 3: *Evaluation of the model parameters in the vicinity of a microrough implant surface.* Based on the in vitro data that compare cell response on substrates with the same (micro)roughness, these parameters can be obtained by

$$(params_i)_{impl-\mu rough} = \alpha_i (params_i)_{impl-smooth} , \tag{7}$$

where the subscript i is the number of the surface-specific parameters of the model. The coefficients α_i are obtained from the in vitro data and represent the ratios of the rates of cell proliferation (cell number), differentiation (osteocalcin expression), extracellular matrix synthesis (collagen synthesis), and local factor production (latent TGF-β) for the microrough titanium substrate with respect to the corresponding rates for the smooth titanium substrate.

2.4 Numerical Simulations

Numerical simulations of peri-implant endosseous healing were performed using a custom finite volume code paying special attention to the requirements of the model,

such as mass conservation and non-negativity of the dependent variables. Details of the numerical implementation can be found elsewhere [21]. For symmetry reasons, only one half of the compartment geometry was taken for the numerical simulations (Fig. 11.1b, left). As the code requires the domain to be constructed of rectangular shapes, it was further simplified (Fig. 11.1b, right). A thick zone of 5 µm defined near the implant surface is shown in Fig. 11.1b, right.

Definition of the initial and boundary conditions. Initially, the wound domain was assumed to be filled with a fibrous tissue extracellular matrix ($m_{c-init} = 0.1$ g ml^{-1} as in [15]) that replaces the cleared hematoma [22]. Activated platelets, with an initial density that varies with the implant surface characteristics [2, 3], were further assumed to exist near the implant surface (Fig. 11.1c), whereas all other densities and concentration were set to zero. For the boundary conditions, migrating mesenchymal cells ($c_m = 7 \times 10^2$ cells ml^{-1}) and a source of osteogenic growth factor ($g_b = 0.9$ ng ml^{-1}) were assumed to be released from the existing alveolar bone [17] (Fig. 11.1b) during a period of time that was considered as a model parameter.

3 Results

Initially, the first simulations of the healing process around the turned implant surface were carried out by taking the model parameter values from [14]. As these parameter values did not lead to a good correspondence with the experimental findings, a fitting of the experimental model of Abrahamsson [8] was required. Very low values were assigned to the initial density of activated cell fragments. Those were assumed to be concentrated in a 5 µm thick zone defined near the implant surface. Additionally, a very low value was given to the release rate. This led to a full ossification after 4 weeks of healing as in the experimental model. Importantly, bone apposition was not perceived onto the turned implant surface. As shown in Fig. 11.2 (top left), the release of the osteogenic growth by activated platelets in this area is
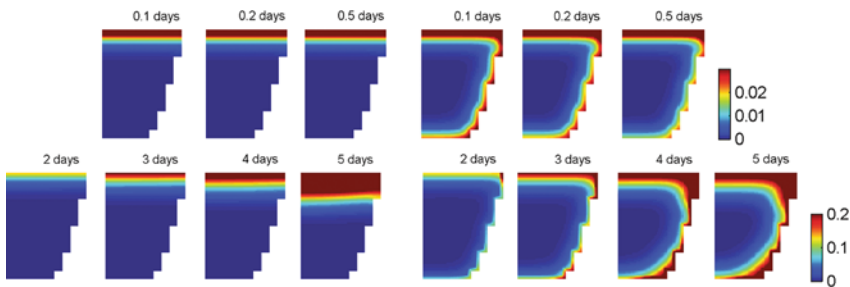
Fig. 11.2 *Top*: Spatiotemporal evolution of the osteogenic growth factor concentration ($\times[100$ ng ml^{-1}]) for the turned (*left*) and the SLA (*right*) implant surface during the early time points. *Bottom*: Spatiotemporal evolution of the density of osteoblast cells ($\times 10^6$ cells ml^{-1}) for both the turned (*left*) and the SLA (*right*) implant surface from day 2 till day 5

not apparent. Moreover, it is clear from Fig. 11.2 (bottom left) illustrating the spatiotemporal distribution of the osteoblasts that such cells do not exist onto the turned implant surface. This can be explained by the fact that mesenchymal stem cells do not reach the implant surface itself.

Furthermore, higher values were assigned to both the initial density of activated platelets and the release rate for the microrough implant surface (SLA). A full ossification was reached around 4 weeks of healing as in the histological observations [7]. As a result of the platelet release, the presence of the osteogenic growth factor in the vicinity of the microrough implant surface can clearly be seen (Fig. 11.2, top right). Osteoblasts can further be perceived onto the SLA implant surface (Fig. 11.2, bottom right) as a result of the differentiation of mesenchymal stem cells that reached the SLA surface.

Figure 11.3 provides a comparison of the spatiotemporal evolution of the densities of bone extracellular matrix (top) and fibrous extracellular matrix (bottom) for both the turned (left) and the SLA (right) surfaces. Similar to the histological examinations, newly formed bone started already during the first week and was only noticed near the host bone (Fig. 11.3, top, left). It was not deposited onto the turned surface but only soft tissue was in contact with this surface.

At 2 weeks of healing, bone formation extended continuously from the existing bone into the wound compartment and occupied the central region (50%). Fibrous tissue was still in contact with the turned implant surface (Fig. 11.3, bottom, left) indicating that only *distance osteogenesis* occurred around this smooth implant surface (Fig. 11.3, top, left). The same observations have been noticed histologically [8].

For the SLA surface, newly bone formation started early during the first week not only as an extension of the old bone to the implant surface but also directly onto the SLA implant surface (Fig. 11.3, top, right) indicating both *distance osteogenesis* and *contact osteogenesis* [17].

At 2 weeks of healing, the numerical predictions show that newly formed bone is continuously in progress in the two directions, while fibrous tissue is still present
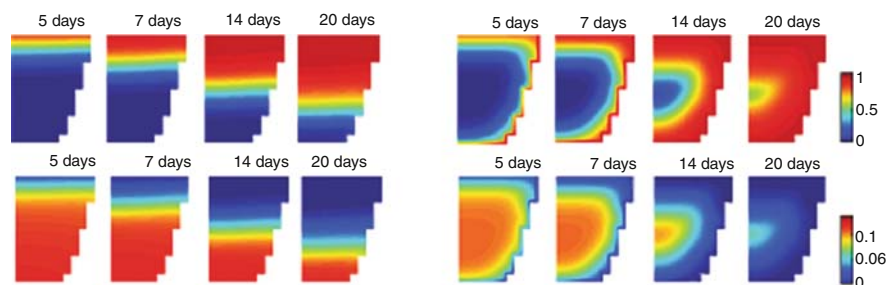
Fig. 11.3 *Top*: Spatiotemporal evolution of the average bone extracellular matrix density ($\times 0.1$ g ml^{-1}) for the turned (*left*) and the SLA (*right*) implant surfaces for days 5, 7, 14, and 20. *Bottom*: Spatiotemporal evolution of the average fibrous extracellular matrix density ($\times 0.1$ g ml^{-1}) for the turned (*left*) and the SLA (*right*) implant surfaces

in the central region (Fig. 11.3, right). Histological observations [8] showed that
the central region was devoid of mineralized tissue as seen here. The amount of
newly formed bone increased and occupied almost all the wound compartment
afterward.

A comparison between the predicted temporal variation of the average bone
extracellular matrix densities for both the SLA and the turned implant surfaces is
represented in Fig. 11.4. It reveals that new bone formation is faster for the SLA
than the turned implant surfaces.

Fig. 11.4 Temporal
evolution of the average
density of the bone
extracellular matrix for the
SLA and the turned implant
surfaces
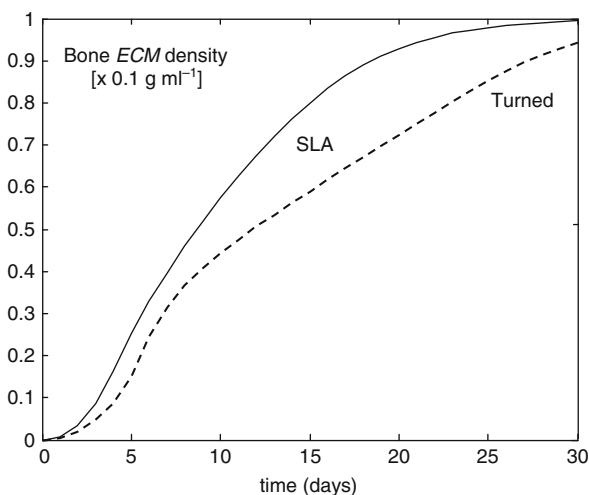
Finally, a sensitivity analysis considering both the release parameter and the ini-
tial density of the activated platelets was accomplished in order to see the influence
of these added parameters on the simulation outcome. Large variations of these
parameters were considered (five orders of magnitude). Figure 11.5 presents the
temporal evolution of the average density of the bone extracellular matrix for differ-
ent values of the initial density of activated platelets when the release rate was kept
constant (left) and for different values of the release rate when the initial density
of the activated platelets was maintained constant (right). This figure clearly shows
that these variations led to different rates in bone formation and, consequently, affect
the healing process. It has been noticed during numerical simulations that lower
values of both parameters can lead to a delay of *contact osteogenesis* (results not
shown). With very low values, this event was not perceived anymore. When higher
values were assigned to these parameters, *distance osteogenesis* was very slow com-
pared to *contact osteogenesis*. Variations of both parameters influenced the speed of
peri-implant healing as well.
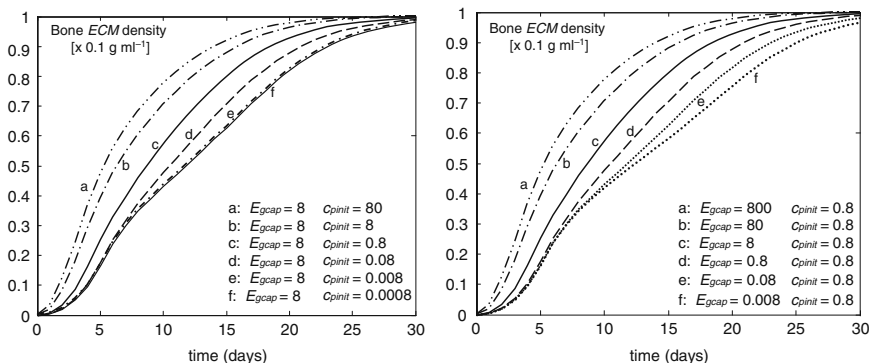
Fig. 11.5 Temporal variation of the average density of the bone extracellular matrix when the initial density of activated platelets varies for a fixed value of the release rate (*left*) and when the release rate of the osteogenic growth factor by activated platelets changes for a constant value of the initial density of the activated platelets (*right*). E_{gcap} (ng day^{-1} platelets^{-1}) is the release rate of the osteogenic growth factor by activated platelets and c_{pinit} is the initial density of activated platelets that were assumed to be concentrated in the vicinity of the implant surface ($\times 10^8$ platelets ml^{-1})

4 Discussion

The presented study demonstrated the capability of the mathematical model to adequately represent some features of peri-implant endosseous healing as described in the literature [5, 17]. This model considered both the role of activated platelets, which is one of the earlier and important events that occur during this process, and the influence of implant surface characteristics on the cellular response, which is a subsequent event. Importantly, this study showed how implant surface characteristics control the effect of activated platelets and modulate the outcome of peri-implant healing.

The influence of implant surface characteristics on both the effect of activated platelets and cell response was treated in a 5 μm thick zone in the vicinity of the implant surface. Activated platelets were assumed to be initially concentrated in this area with a density that is dependent on the implant surface characteristics. Moreover, the effect of activated platelets was represented by a release of osteogenic growth factor only. Additionally, the impact of surface properties on cell response was dealt with by identifying the most important parameters of the model that reflect this influence. Consequently, two sets of surface-specific model parameter values were determined based on a proposed algorithm and on in vitro findings [20]. Furthermore, another set of model parameter values were used far from the implant surface.

A well-designed in vivo animal model [8] that looked at the healing process around implants with different surface characteristics was selected. This pertinent setup allowed to see whether the prediction of the current mathematical model was similar to the experimental observations.

The influence of surface characteristics on cell response was captured by decreasing the rate of cell proliferation and increasing the rate of cell differentiation together with the rates of matrix synthesis and osteogenic factor production in the vicinity of the implant surface. A rationale for modulating these parameters was found in other conducted in vitro investigations [5, 13, 23].

Additionally, during numerical simulations, a very low value was assigned to the initial density of activated platelets for the smooth implant surface, whereas a higher value was given to this initial density for the microrough surface. An explanation to this alteration can be supported by the observations from a biochemical analysis [24] that showed an increased amount of fibrinogen on a microrough surface with respect to a smooth surface. In addition, the thickness of this layer of protein itself and the type of adsorbed protein depended on the surface characteristics as well [25]. Higher surface concentrations of adsorbed protein (fibrinogen) lead to higher levels of platelet adhesion [3]. Both are shown to be higher on rougher surface than on smoother surface [24]. This shows the sensitivity of protein and platelet responses to small variations in the biomaterial properties. Furthermore, it has been suggested [25] that microrough surfaces produce considerably higher agglomeration of red blood cells, meaning a significant aggregation of platelets on microrough surfaces with respect to smooth surfaces. Moreover, as platelet aggregation represents one functional aspect of platelet activation [4], platelet activation is then a function of micron/submicron roughness [17]. This might also explain why a high value was assigned to the release rate for the microrough with respect to the smooth implant surfaces during the numerical simulations. The platelet initial density and the release rate were estimated numerically, as in vitro data comparing platelet response to titanium substrates with surface roughnesses similar to that of the SLA and the turned implant surfaces are lacking. With these estimated values assigned to these parameters, the wound compartment was healed either by bidirectional or unidirectional bone formation depending on the implant surface type (microrough or smooth).

A good agreement between the numerical results and the experimental findings was obtained. This study showed that a microrough implant surface speeded up peri-implant healing and led to a higher rate of bone formation than did the smooth implant surface. This was also observed in the histomorphometric analysis [8].

This promising mathematical model can be extended to consider other aspects of peri-implant endosseous healing and also for the simulations of treatment strategies such as the use of platelet concentrates or the administration of osteogenic agents, such as bone morphogenic proteins.

References

1. Davies, J.E., Schüpbach, P., Cooper, L.: The changing of interface: osseointegration and dental implants. In: Asbjorn Jokstad (ed.).Willey-Blackwell, Inc., Iowa, pp. 213–223 (2009)

2. Park, J.Y., Gemmell, C.H., Davies, J.E.: Platelet interactions with titanium: modulation of platelet activity by surface topography. Biomaterials, 22, 2671–2682 (2001)

3. Kikuchi, L., Park, J.Y., Victor, C., Davies, J.E.: Platelet interactions with calcium-phosphate-coated surfaces. Biomaterials, 26, 5285–5295 (2005)

4. Anderson, J.M.: The cellular cascades of wound healing. In: Davies, J.E. (ed.). Bone Engineering. em Squared Inc., Toronto, pp. 81–93 (2000)

5. Schwartz, Z., Lohmann, C.H., Oefinger, J., Bonewald, L.F., Dean, D.D., Boyan, B.D.: Implant surface characteristics modulate differentiation behavior of cells in the osteoblastic lineage. Advances in Dental Research, 13, 38–48 (1999)

6. Buser, D., Broggini, N., Wieland, M., Schenk, R.K., Denzer, A.J., Cochran, D.L., Hoffmann, B., Lussi, A., Steinemann, S.G.: Enhanced bone apposition to a chemically modified SLA titanium surface. Journal of Dental Research, 83(7), 529–533 (2004)

7. Berglundh, T., Abrahamsson, I., Lang, N.P., Lindhe, J.: De novo alveolar bone formation adjacent to endosseous implants. A model study in the dog. Clinical Oral Implants Research, 14, 251–262 (2003)

8. Abrahamsson, I., Berglundh, T., Linder, E., Lang, N.P., Lindhe, J.: Early bone formation adjacent to rough and turned endosseous implant surfaces. An experimental study in the dog. Clinical Oral Implant Research, 15, 381–392 (2004)

9. Schwarz, F., Herten, M., Sager, M., Wieland, M., Dard, M., Becker, J.: Histological and immunohistochemical analysis of initial and early osseous integration at chemically modified and conventional SLA titanium implants: preliminary results of a pilot study in dogs. Clinical Oral Implants Research, 18, 481–488 (2007)

10. Schweikl, H., Müller, R., Englert, C., Hiller, K.A., Kujat, R., Nerlich, M., Schmalz, G.: Proliferation of osteoblasts and fibroblasts on model surfaces of varying roughness and surface chemistry. Journal of Materials Science. Materials in Medicine, 18(10), 1895–1905 (2007)

11. Brunette, D.M.: Fibroblasts on micromachined substrata orient hierarchically to grooves of different dimensions. Experimental Cell Research, 164, 11–26 (1986)

12. Boyan, B.D., Sylvia, V.L., Liu, Y., Sagun, R., Cochran, D.L., Lohmann, C.H., Dean, D.D., Schwartz, Z.: Surface roughness mediates its effects on osteoblasts via protein kinase A and phospholipase A_2. Biomaterials, 20, 2305–2310 (1999)

13. Boyan, B.D., Lossdörfer, S., Wang, L., Zhao, G., Lohmann, C.H., Cochran, D.L., Schwartz, Z.: Osteobalsts generate an osteogenic microenvironment when grown on surfaces with rough microtopographies. European Cells and Materials, 6, 22–27 (2003)

14. Amor, N., Geris, L., Vander Sloten, J., Van Oosterwyck, H.: Modelling the early phases of bone regeneration around an endosseous oral implant. Computer Methods in Biomechanics and Biomedical Engineering, 12, 459–468 (2009)

15. Bailòn Plaza, A., van der Meulen, M.C.H.: A mathematical framework to study the effects of growth factor influences on fracture healing. Journal of Theoretical Biology, 212, 191–209 (2001)

16. Geris, L., Gerisch, A., Maes, C., Carmeliet, G., Weiner, R., Vander Sloten, J., Van Oosterwyck, H.: Mathematical modeling of fracture healing in mice: comparison between experimental data and numerical simulation results. Medical and Biological Engineering and Computing, 44, 280–289 (2006)

17. Davies, J.E.: Understanding peri-implant endosseous healing. Journal of Dental Education, 67(8), 932–949 (2003)

18. Davies, J.E.: In vitro modeling of bone/implant interface. The Anatomical Record, 245, 426–445 (1996)

19. Bolander, M.E.: Regulation of Fracture repair by growth factors. Proceedings of the. Society for Experimental Biology and Medicine, 200, 165–170 (1992)

20. Lincks, J., Boyan, B.D., Blanchard, C.R., Lohmann, C.H., Liu, Y., Cochran, D.L., Dean, D.D., Schwartz, Z.: Responses of MG63 osteoblast-like cells to titanium and titanium alloy is dependent on surface roughness and composition. Biomaterials, 19, 2219–2232 (1998)

21. Gerisch, A., Chaplain, M.A.J.: Robust numerical methods for taxis-diffusion-reaction systems: applications to biomedical problems. Mathematical and Computer Modelling, 43, 49–75 (2005)

22. Davies, J.E., Hosseini, M.M.: Histodynamics of endosseous wound healing. In: Davies, J.E. (ed.): Bone Engineering. em Squared Inc., Toronto, pp. 1–14 (2000)

23. Kieswetter, K., Schwartz, Z., Dean, D.D., Boyan, B.D.: The role of implant surface characteristics in the healing of bone. Critical Review in Oral Medicine, 7, 329–245 (1996)

24. Nygren, H., Eriksson, C., Lausmaa, I.: Adhesion and activation of platelets and polymorphonuclear granulocyte cells at TiO2 surfaces. The Journal of Laboratory and Clinical Medicine, 129, 35–46 (1997)

25. Gemmell, C.H., Park, J.K.: Initial blood interactions with endosseous implant materials. In: Davies, J.E. (ed.): Bone Engineering. em Squared Inc., Toronto, pp. 108–117 (2000)

Chapter 12
Subject-Specific Ligament Models: Toward Real-Time Simulation of the Knee Joint

Tobias Heimann, François Chung, Hans Lamecker, and Hervé Delingette

Abstract We present an efficient finite element method to simulate a transversely isotropic nonlinear material for ligaments. The approach relies on tetrahedral elements and exploits the geometry to optimize computation of the derivatives of the strain energy. To better support incompressibility, deviatoric and dilational responses are uncoupled and a penalty term controls volume preservation. We derive stress and elasticity tensors required for implicit solvers and verify our model against the FEBio software using a variety of load scenarios with synthetic shapes. The maximum node positioning error for ligament materials is <5% for strains under physiological conditions.

To generate subject-specific ligament models, we propose a novel technique to estimate fiber orientation from segmented ligament geometry. The approach is based on an automatic centerline extraction and generation of the corresponding diffusion field. We present results for a medial collateral ligament segmented from standard MRI data. Results show the general viability of the method, but also the limitations of current MRI acquisitions. In the future, we hope to employ the presented techniques for real-time simulation of knee surgery.

Keywords Simulation · Knee · Ligament · Real-Time

1 Introduction

The human knee joint has been extensively studied in the field of biomechanics, both due to its complex anatomy and due to its high clinical relevance. It has to cope with high loads and large displacements during many daily activities. The knee ligaments, notably the two cruciate ligaments and the two collateral ligaments, play a key role in ensuring stability of the joint [1]. They are also at increased risk during

T. Heimann (✉)
Asclepios Project, INRIA, Sophia Antipolis, France
e-mail: tobias.heimann@inria.fr

high-impact scenarios as occurring, e.g., in many sports activities. In case of ligament rupture, kinematics of the knee are severely compromised and sophisticated surgical interventions are required to restore its function. Virtual simulation of these surgeries for subject-specific cases combined with a subsequent analysis of resulting knee kinematics seem a promising way to increase success rates of interventions [2, 3].

The finite element method (FEM) has successfully been used to analyze a variety of problems regarding the knee joint [3–5]. To achieve realistic simulation of ligaments, sophisticated material models have been presented [6, 7]. These models implement properties such as the transverse isotropy and nonlinear stress–strain curve due to internal collagen fibers and partly also viscoelastic behavior. In most works related to real-time simulation, however, material properties of ligaments are highly simplified to maintain the required framerate. Often, simple isotropic linear elasticity is used [8]. Picinbono et al. [9] presented an optimized FE model for tetrahedral elements, which also allowed transversely isotropic materials. However, the stress–strain relationship was still linear. A fast nonlinear anisotropic material model was presented by Teran et al. [10], who use the finite volume method to simulate muscles and tendons. This approach is equivalent to FEM for constant strain linear basis functions. Recently, Joldes et al. [11] developed a highly efficient framework for computation of soft tissue deformation, which is based on Total Lagrangian and explicit time integration. This framework was also implemented on GPU and used for viscoelastic nonlinear soft tissue simulation by Taylor et al. [12].

In this work, we present a material model that incorporates the ligament-specific properties of transverse isotropy and nonlinear stress–strain curve and that is suitable for both explicit and implicit solvers. The model is aimed at real-time simulation and reaches high efficiency due to the use of linear tetrahedral elements, which leads to an optimization of a large part of the involved computations. We also address the problem of generating subject-specific models, which is neglected in many current publications: with transversely isotropic materials for ligaments, the main fiber orientation has to be known for each finite element in the simulation. Techniques as X-ray diffraction or optical diffraction that can be used for experiments with cadavers are not possible in vivo. To employ FEM simulations of the knee for surgery planning, fiber orientations have to be extracted from clinical imaging modalities as MRI or DT-MRI.

The remainder of this chapter is organized as follows: in Section 2, we present our optimized FE model for ligaments. Subsequently, the method to determine local fiber orientation from segmented geometry is presented in Section 3. In Section 4, image data and rheological parameters to generate a subject-specific model of the medial collateral ligament (MCL) are described. In Section 5, we verify our FE model by comparing it to the established FEBio software[1] and we present our model of the MCL. We close with a discussion of results and future work.

---

[1]FEBio is available at the web site of the Musculoskeletal Research Laboratories of the University of Utah: http://mrl.sci.utah.edu/software.php

2 Transversely Isotropic Hyperelasticity for Tetrahedrons

In this section, we present the strain energy for the employed material model and derive its stress tensor (first derivative) and elasticity tensor (second derivative). The latter one is required if the model is used for implicit or quasi-static analysis. Throughout this work, we follow the concepts presented by Delingette [13] for triangular finite elements. In particular, the elasticity tensor for each node is assembled by accumulating terms from all adjacent edges, which allows to exploit symmetry to reduce computations.

2.1 Properties of Tetrahedral Elements

The tetrahedral element with linear basis function features a constant strain, which reduces integration to a multiplication by volume. Moreover, the deformation tensor can be calculated efficiently based on the current node positions $\mathbf{Q}_i$ and the *shape vectors* of the tetrahedron. Shape vectors $\mathbf{D}_i$ are defined by the rest configuration of the tetrahedron (with node positions $\mathbf{P}_i$) as

$$\mathbf{D}_i = \frac{s}{V_0} \left((\mathbf{P}_{i\oplus 2} - \mathbf{P}_{i\oplus 1}) \wedge (\mathbf{P}_{i\oplus 3} - \mathbf{P}_{i\oplus 1}) \right), \tag{1}$$

where $\wedge$ denotes the cross product, V_0 is the volume in rest configuration, and $s = 1$ for $i = 2,4$, else $s = -1$. Shape vector $\mathbf{D}_i$ stands perpendicular to the face opposite node i and points inward. For the many interesting properties of shape vectors, we refer the reader to [13]. Here, we note that the deformation gradient tensor $\nabla\mathbf{\Phi}$ can be expressed as

$$\nabla\mathbf{\Phi} = \sum_{i=1}^{4} \mathbf{Q}_i \otimes \mathbf{D}_i. \tag{2}$$

Consequently, the right Cauchy–Green deformation tensor $\mathbf{C}$ is

$$\mathbf{C} = \nabla\mathbf{\Phi}^T \nabla\mathbf{\Phi} = \sum_{i=1}^{4} \sum_{j=1}^{4} (\mathbf{Q}_i \cdot \mathbf{Q}_j)(\mathbf{D}_i \otimes \mathbf{D}_j). \tag{3}$$

The Jacobian J of the deformation gradient tensor $\nabla\mathbf{\Phi}$ can also be expressed as the ratio of volumes in deformed and in rest configuration: $J = V/V_0$. We sum up that the signed volume of a tetrahedron is given by

$$V = \frac{1}{6} \left((\mathbf{Q}_4 - \mathbf{Q}_1) \cdot ((\mathbf{Q}_2 - \mathbf{Q}_1) \wedge (\mathbf{Q}_3 - \mathbf{Q}_1)) \right), \tag{4}$$

where the order of nodes is interchangeable as long as the sign is kept.

As described in [13], forces on node i can be determined directly by $\mathbf{F}_i = -V \nabla \Phi \mathbf{S} \, \mathbf{D}_i$, where $\mathbf{S}$ is the second Piola–Kirchhoff tensor used for large deformations. Using the weak formulation for finite elements [14], the required derivative $\partial \mathbf{S}/\partial \mathbf{C}$ results in very complex expressions (see, e.g., [6]). Therefore, we employ the Rayleigh–Ritz approach and derive the required expressions directly from the discretized strain energy using individual node positions $\mathbf{Q}_i$.

2.2 Strain Energy

We base our strain energy W on the terms proposed by Weiss et al. [6] for incompressible, transversely isotropic materials. However, instead of using an Augmented Lagrangian method to ensure incompressibility, we employ a simple penalty approach based on the bulk modulus of the material. The energy is composed of three different terms:

$$W = F_G(I_1) + F_C(I_4) + F_V(J), \tag{5}$$

F_G describes the contribution of the isotropic ground substance matrix, F_C describes the contribution from the collagen fibers, and F_V is the penalty term for volume changes. The underlying invariants are defined as

$$
\begin{aligned}
I_1 &= J^{-\frac{2}{3}} \, \mathrm{tr} \, \mathbf{C}, \\
I_4 &= J^{-\frac{2}{3}} \, \mathbf{aCa} = \lambda^2, \\
J &= V/V_0.
\end{aligned}
\tag{6}
$$

Here, I_1 is a standard invariant of $\mathbf{C}$ for nearly incompressible materials [14]. I_4 arises from the anisotropy of the material, using main fiber orientation $\mathbf{a}$ [6]. $\lambda = l/l_0$ is the stretch along this direction. Note that in our formulation, I_1 and I_4 remain constant under a pure volume change. Thus, F_G and F_C represent a pure deviatoric response and F_V a pure dilational response.

2.3 Derivations for the Jacobian

Starting with the formula for the volume of a tetrahedron (4), the first derivative of J w.r.t. point $\mathbf{Q}_i$ can be determined as

$$\frac{\partial J}{\partial \mathbf{Q}_i} = \frac{1}{6V_0}(\mathbf{b} \wedge \mathbf{c})^T. \tag{7}$$

Here, $\mathbf{b} = \mathbf{Q}_j - \mathbf{Q}_l$ and $\mathbf{c} = \mathbf{Q}_k - \mathbf{Q}_l$ are edge vectors of the triangle opposing $\mathbf{Q}_i$. Thus, indices j,k,l depend directly on i and can be stored in a simple table. Using edge vector $\mathbf{c}$, the second derivative of J is

$$\frac{\partial^2 J}{\partial \mathbf{Q}_j \partial \mathbf{Q}_i} = \frac{1 - \delta_{ij}}{6V_0} \begin{bmatrix} 0 & -c_z & c_y \\ c_z & 0 & -c_x \\ -c_y & c_x & 0 \end{bmatrix}. \tag{8}$$

Here, δ_{ij} is the Kronecker delta and matrix elements c are components of the edge opposing points $\mathbf{Q}_i$ and $\mathbf{Q}_j$.

2.4 Derivations for Isotropic Ground Substance

Following Weiss et al. [6], we use a neo-Hookean material with shear modulus μ to model the response of the isotropic ground substance matrix:

$$F_G = \frac{\mu}{2} \left(J^{-\frac{2}{3}} \operatorname{tr} \mathbf{C} - 3 \right). \tag{9}$$

Stress tensor The individual terms required for the first derivative are

$$\frac{\partial J^{-\frac{2}{3}}}{\partial \mathbf{Q}_i} = -\frac{1}{9V_0} J^{-\frac{5}{3}} (\mathbf{b} \wedge \mathbf{c})^T \quad , \quad \frac{\partial \operatorname{tr} \mathbf{C}}{\partial \mathbf{Q}_i} = 2 \sum_{n=1}^{4} (\mathbf{D}_n \cdot \mathbf{D}_i) \mathbf{Q}_n^T. \tag{10}$$

The first derivative can then be calculated by

$$\frac{\partial F_G}{\partial \mathbf{Q}_i} = \frac{\mu}{2} \left(J^{-\frac{2}{3}} \frac{\partial \operatorname{tr} \mathbf{C}}{\partial \mathbf{Q}_i} + \frac{\partial J^{-\frac{2}{3}}}{\partial \mathbf{Q}_i} \operatorname{tr} \mathbf{C} \right). \tag{11}$$

Elasticity tensor Again, we start with the individual terms of F_G:

$$\frac{\partial^2 J^{-\frac{2}{3}}}{\partial \mathbf{Q}_j \partial \mathbf{Q}_i} = \frac{10}{9} J^{-\frac{8}{3}} \left(\frac{\partial J}{\partial \mathbf{Q}_j} \right)^T \frac{\partial J}{\partial \mathbf{Q}_i} - \frac{2}{3} J^{-\frac{5}{3}} \frac{\partial^2 J}{\partial \mathbf{Q}_j \partial \mathbf{Q}_i} \quad , \quad \frac{\partial^2 \operatorname{tr} \mathbf{C}}{\partial \mathbf{Q}_j \partial \mathbf{Q}_i} = 2(\mathbf{D}_i \cdot \mathbf{D}_j) \mathbf{1}. \tag{12}$$

Using these results, the second derivative is

$$\frac{\partial^2 F_G}{\partial \mathbf{Q}_j \partial \mathbf{Q}_i} = \frac{\mu}{2} \left(\frac{\partial^2 J^{-\frac{2}{3}}}{\partial \mathbf{Q}_j \partial \mathbf{Q}_i} \operatorname{tr} \mathbf{C} + \left(\frac{\partial \operatorname{tr} \mathbf{C}}{\partial \mathbf{Q}_j} \right)^T \frac{\partial J^{-\frac{2}{3}}}{\partial \mathbf{Q}_i} + \left(\frac{\partial J^{-\frac{2}{3}}}{\partial \mathbf{Q}_j} \right)^T \frac{\partial \operatorname{tr} \mathbf{C}}{\partial \mathbf{Q}_i} + J^{-\frac{2}{3}} \frac{\partial^2 \operatorname{tr} \mathbf{C}}{\partial \mathbf{Q}_j \partial \mathbf{Q}_i} \right). \tag{13}$$

2.5 Derivations for Collagen Fiber Family

F_C is a scalar function governing the nonlinear behavior of the material along the main fiber orientation. We employ the formulation by Weiss et al. [6] and explicitly model the toe region of the stress–strain curve, which represents the successive recruitment of collagen fibers in ligaments under lower strains $\lambda < \lambda^*$:

$$\frac{\partial F_C}{\partial \lambda} = 0 \qquad\qquad , \quad \lambda < 1,$$

$$\frac{\partial F_C}{\partial \lambda} = C_3(\exp{(C_4(\lambda - 1))} - 1) \qquad , \quad \lambda < \lambda^*, \qquad\qquad (14)$$

$$\frac{\partial F_C}{\partial \lambda} = C_5 \lambda + C_6 \qquad\qquad , \quad \lambda \geq \lambda^*.$$

Stress tensor First, we note that

$$\frac{\partial F_C}{\partial \mathbf{Q}_i} = \frac{\partial F_C}{\partial \lambda} \frac{\partial \lambda}{\partial I_4} \frac{\partial I_4}{\partial \mathbf{Q}_i} = \frac{\partial F_C}{\partial \lambda} \frac{1}{2\lambda} \frac{\partial I_4}{\partial \mathbf{Q}_i}. \qquad\qquad (15)$$

This leaves us with finding the derivative for I_4. As we can use the result for $\partial J^{-\frac{2}{3}}/\partial \mathbf{Q}_i$ from (10), we continue with

$$\frac{\partial \mathbf{aCa}}{\partial \mathbf{Q}_i} = 2(\mathbf{a} \cdot \mathbf{D}_i) \sum_{n=1}^{4} (\mathbf{a} \cdot \mathbf{D}_n) \mathbf{Q}_n^T. \qquad\qquad (16)$$

We now know all the individual terms required for the derivative of I_4:

$$\frac{\partial I_4}{\partial \mathbf{Q}_i} = J^{-2/3} \frac{\partial \mathbf{aCa}}{\partial \mathbf{Q}_i} + \frac{\partial J^{-\frac{2}{3}}}{\partial \mathbf{Q}_i} \mathbf{aCa}. \qquad\qquad (17)$$

Using this in (15) delivers the stress tensor for F_C.

Elasticity tensor The second derivatives of the stress–strain curve are

$$\frac{\partial^2 F_C}{\partial \lambda^2} = 0 \qquad\qquad , \quad \lambda < 1,$$

$$\frac{\partial^2 F_C}{\partial \lambda^2} = C_3 C_4 \exp{(C_4(\lambda - 1))} \qquad , \quad \lambda < \lambda^*, \qquad\qquad (18)$$

$$\frac{\partial^2 F_C}{\partial \lambda^2} = C_5 \qquad\qquad , \quad \lambda \geq \lambda^*.$$

We continue from (15), which gives us

$$\frac{\partial^2 F_C}{\partial \mathbf{Q}_j \partial \mathbf{Q}_i} = \left(\frac{\partial^2 F_C}{\partial \lambda^2} \left(\frac{\partial \lambda}{\partial I_4} \right)^2 + \frac{\partial F_C}{\partial \lambda} \frac{\partial^2 \lambda}{\partial I_4^2} \right) \left(\frac{\partial I_4}{\partial \mathbf{Q}_j} \right)^T \frac{\partial I_4}{\partial \mathbf{Q}_i} + \frac{\partial F_C}{\partial \lambda} \frac{\partial \lambda}{\partial I_4} \frac{\partial^2 I_4}{\partial \mathbf{Q}_j \partial \mathbf{Q}_i}. \qquad (19)$$

The second derivative of λ w.r.t. I_4 is simply $\frac{\partial^2 \lambda}{\partial I_4^2} = -\frac{1}{4\sqrt{I_4}^3}$. Next, we require the second derivative of I_4:

$$\frac{\partial^2 I_4}{\partial \mathbf{Q}_j \partial \mathbf{Q}_i} = \frac{\partial^2 J^{-\frac{2}{3}}}{\partial \mathbf{Q}_j \partial \mathbf{Q}_i} \mathbf{aCa} + \left(\frac{\partial \mathbf{aCa}}{\partial \mathbf{Q}_j} \right)^T \frac{\partial J^{-\frac{2}{3}}}{\partial \mathbf{Q}_i} + \left(\frac{\partial J^{-\frac{2}{3}}}{\partial \mathbf{Q}_j} \right)^T \frac{\partial \mathbf{aCa}}{\partial \mathbf{Q}_i} + J^{-\frac{2}{3}} \frac{\partial^2 \mathbf{aCa}}{\partial \mathbf{Q}_j \partial \mathbf{Q}_i}. \qquad (20)$$

The only new term in this equation is the second derivative of **aCa**, which is

$$\frac{\partial^2 \mathbf{aCa}}{\partial \mathbf{Q}_j \partial \mathbf{Q}_i} = 2(\mathbf{a} \cdot \mathbf{D}_i)(\mathbf{a} \cdot \mathbf{D}_j)\mathbf{1}. \tag{21}$$

Now all terms required for (19) are known and we can calculate the elasticity tensor for F_C.

2.6 Derivations for Volume Conservation

The penalty term controlling response of an element to volume changes is the same as for a nearly incompressible neo-Hookean model [14]:

$$F_V = \frac{K}{2}(J-1)^2, \tag{22}$$

with K as the bulk modulus of the material.

Stress tensor The derivation of the first derivative is straightforward:

$$\frac{\partial F_V}{\partial \mathbf{Q}_i} = K(J-1)\frac{\partial J}{\partial \mathbf{Q}_i}. \tag{23}$$

Elasticity tensor The second derivative of the penalty term is

$$\frac{\partial^2 F_V}{\partial \mathbf{Q}_j \partial \mathbf{Q}_i} = K\left(\left(\frac{\partial J}{\partial \mathbf{Q}_j}\right)^T \frac{\partial J}{\partial \mathbf{Q}_i} + (J-1)\frac{\partial^2 J}{\partial \mathbf{Q}_j \partial \mathbf{Q}_i}\right). \tag{24}$$

2.7 In Situ Stress

When joints as the knee are in neutral position, the involved ligaments are usually still under tension [15]. Since this tension stabilizes the joint even when no muscles are active, the so-called *in situ stress* plays an important role in joint kinematics. To achieve realistic simulation results, the employed FE model should thus include pre-stressed materials. In our model, we incorporate in situ stress by increasing the magnitude of direction vectors in the fiber orientation field. By default, fiber orientation **a** is represented by a unit vector. If we use a modified orientation vector $\mathbf{a}' = (1+c)\mathbf{a}$, the material is under a strain of c even for an identity deformation gradient tensor.

3 Estimating Subject-Specific Fiber Orientations

We assume that the subject-specific geometry of the ligament to be simulated is given by a high-resolution mesh. The attachment areas to the two bones the ligament

connects are specified by two sets of vertices of this mesh, A_1 and A_2. The first step in our approach consists of finding the centerline between these two areas. This line provides a solid estimate of the main fiber orientation.

3.1 Centerline Extraction

Centerline extraction is a common problem in medical image analysis, employed, e.g., for vessel tracking or for generating fly-through paths for virtual endoscopy. For a brief overview of existing approaches see Bouix et al. [16]. As we can calculate the line start and end positions as the average positions of A_1 and A_2, we opt for a method based on minimal cost paths. Among all possible paths $P(s)$ connecting both points, we search the one that minimizes a specific metric $\mathcal{C}$. We include two components in $\mathcal{C}$: first, the path should be as short as possible, and second, it should run at maximum distance from the mesh surface (i.e., as close to the medial sheet of the shape as possible). Both components are weighted by $\alpha \in [0,1]$ such that $\alpha = 0$ results in the shortest possible path (a straight line) and $\alpha = 1$ in a path around the geometric center. This leads to the following metric:

$$\mathcal{C}(P) = \int_0^1 \left| \frac{\partial P}{\partial s} \right| \left(\frac{\alpha}{d^2(P(s))} + (1 - \alpha) \right) ds, \tag{25}$$

where $d(x)$ is the closest distance to the mesh surface from point x.

The search for the minimal cost path is set in a discrete setting. First, the surface mesh is rendered to an image volume and the corresponding distance transformation is calculated. Then, a graph is constructed with all object voxels as nodes and the 26-neighborhood for each voxel as edges. A Dijkstra search finally delivers the minimum cost path that serves as centerline for the ligament.

3.2 Local Fiber Orientation

To calculate fiber orientations for all positions inside the segmented ligament mesh, we use the gradient of a diffusion field between centerline and mesh boundary. The diffusion field D is constructed such that all voxels on the centerline have a value of 0 and all voxels on the mesh boundary a value of 1. Generation of this field is a classical Dirichlet problem. In our current implementation we use the following geometric method: for each point x within the mesh, the closest point on the centerline $C(x)$ is determined. A ray is cast from $C(x)$ through x until it hits the mesh boundary at $B(x)$. We then set $D(x) = |x - C(x)|/|B(x) - C(x)|$.

We assume that fibers are oriented parallel to the boundary for positions on the boundary and parallel to the centerline for positions on the centerline. In between, fiber directions are interpolated so that they run perpendicular to the gradient ∇D, i.e., on an isosurface of the diffusion field. To determine the orientation vector $\mathbf{a}(x)$,

the direction of the centerline at $C(x)$ is projected onto the isosurface at x and normalized. Finally, orientation vectors for all x inside a specific tetrahedral element are averaged to yield **a** for this element.

4 Material for Subject-Specific Ligament Model

As proof of concept for the presented methods, we simulate the medial collateral ligament (MCL) in a subject-specific knee joint.

4.1 Image Data

MRI data was used as source for the geometry of the simulation. An institutional medical ethics committee approved the image acquisition and the subject gave his written consent. The employed data set covers the right knee of a healthy male subject (age 38) in full extension. It was acquired using a 1.5T Siemens MRI device with Flair Sagittal 3D T1 protocol and 256×256 matrix. Image resolution was 0.5×0.5 mm with a slice thickness of 1.0 mm.

4.2 Rheological Parameters

While it is possible to extract subject-specific geometry for a living subject, we can think of no way to determine subject-specific material properties. For our simulation of the MCL, we thus employ the rheological parameters presented for this structure by Weiss et al. [6]: $\mu = 27.7$ MPa, $\lambda^* = 1.03$, $C_3 = 2.07$ MPa, $C_4 = 61.44$, $C_5 = 640.7$ MPa. In situ strain was set to 2.9%. To achieve near-incompressible behavior, the bulk modulus was set to $K = 1{,}000$.

5 Experiments and Results

5.1 Verification

To verify our implementation of the material model, we conducted a number of tests on a synthetic cube shape of 1 mm edge length. The employed mesh consisted of 4,316 nodes and 20,737 tetrahedral elements. Material parameters were set to the values given in Section 4.2. Constraints were used to fix positions of all nodes on the lower side of the cube. To all nodes on the upper side of the cube, we applied constant forces pointing upward (tensile strain) or downward (compressive strain). An implicit solver with velocity damping was run until convergence and the resulting deformed mesh was exported.

The scenario was then simulated with the FEBio software, using the same mesh and identical boundary conditions. The material model in FEBio was set to transversely isotropic Mooney Rivlin with the same parameters as above. Volume conservation was enforced using the Augmented Lagrangian approach. The solution was obtained for the quasi-static case with the default BFGS solver.

We compared our results to the FEBio reference solution for a variety of cases. All positioning errors are expressed in percent of the edge length of the cube in rest configuration. Table 12.1 lists results for tensile forces typically encountered in ligaments under physiological conditions. In Fig. 12.1, the corresponding node positioning errors are visualized. Table 12.2 lists results for cases that usually do not occur in ligaments (as loading perpendicular to fiber orientation) and also compares our results to the FEBio solution without Augmented Lagrangian. Figure 12.2 again visualizes the corresponding node positioning errors.

Table 12.1 Results of experiments on the synthetic cube with fibers oriented parallel to tensile forces. For each load, the resulting average fiber strain and volume change is given. From comparison to the FEBio solution, we determined the average positioning error for all nodes on the top surface of the cube as well as the maximum error

Load/node	Total load	Avg. fiber strain(%)	Vol. change(%)	Avg. error(%)	Max. error(%)
0.02 N	5.8 N	+1.6	+0.2	0.1	0.4
0.05 N	14.5 N	+3.0	+0.5	0.3	1.0
0.10 N	28.9 N	+4.9	+1.1	0.5	1.9
0.20 N	57.8 N	+8.8	+2.2	0.9	3.4
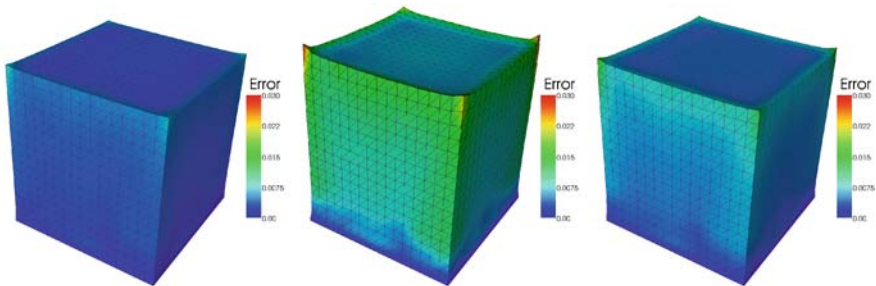
Fig. 12.1 Node positioning errors to FEBio reference solution for tensile loading, color-coded from 0 to 3%. From *left* to *right*, applied tensile forces per node are 0.05 N, 0.1 N, and 0.2 N, respectively. Fibers are oriented parallel to forces

5.2 MCL Simulation

Geometry of femur, tibia, and MCL was segmented manually from the MRI data set described in Section 4. For the centerline extraction, we set $\alpha = 0.1$. Figure 12.3 shows the segmented ligament mesh and the resulting centerline. From the surface,

Table 12.2 Additional experiments on the synthetic cube. The first two cases represent unusual load scenarios, the last two (marked with *) are compared to the FEBio solution without Augmented Lagrangian

Setup	Vol. change(%)	Avg. error(%)	Max. error(%)
Fibers perpendicular to tensile load (0.05 N)	+0.7	3.9	5.8
Fibers parallel to compressive load (0.05 N)	−0.5	2.4	5.6
Fibers parallel to compressive load (0.10 N)*	+1.1	0.3	0.6
Fibers perpendicular to tensile load (0.05 N)*	+0.7	0.4	0.5
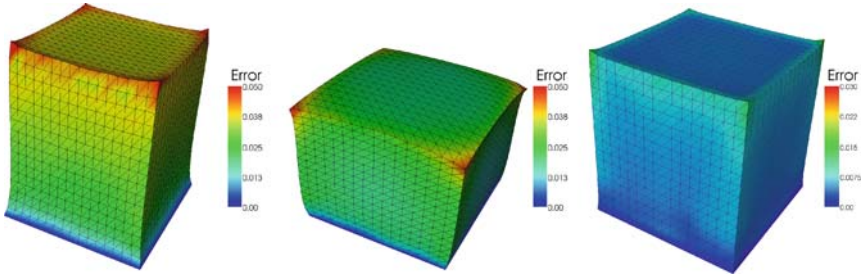
Fig. 12.2 Node positioning errors for alternative test cases. *Left*: Tensile forces of 0.05 N/node, but with fibers oriented perpendicular to forces. *Center*: Compressing forces of 0.05 N/node. *Right*: Same scenario as in Fig. 12.1 *center*, but compared to FEBio without Augmented Langrangian. Note the different error scales (up to 6% for *left* and *center*, up to 1% for *right*)
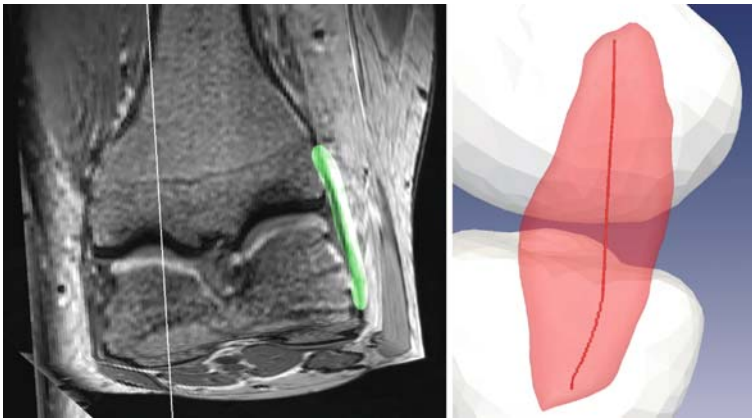
Fig. 12.3 Segmented ligament mesh together with the original MRI data (*left*) and the extracted centerline connecting the attachment areas of femur and tibia (*right*)

we generated a volumetric mesh consisting of 1,193 nodes and 5,911 tetrahedra. Using the presented rheological parameters for the ligament and rigid bones, a dynamic simulation was set up with the SOFA software [17]. An Euler implicit scheme was used for time integration, and a modified conjugate gradient solver [18]

was employed to solve the system of equations. While the tibia was fixed, the femur was moved manually to different flexion angles. Figure 12.4 shows the resulting strain energy within the MCL for these cases. On an Intel Core 2 Duo notebook with 2.2 GHz CPU the obtained framerate was 15 frames/s (including simulation and visualization).
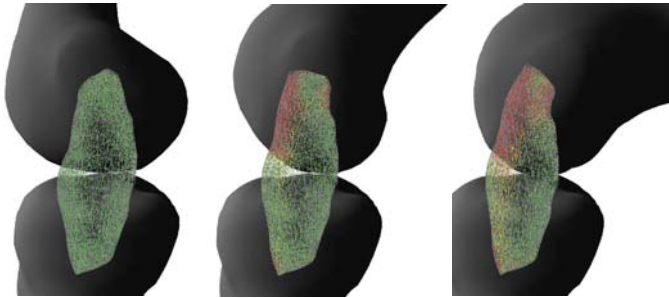
Fig. 12.4 Simulation of strain in the MCL at $0°$, $45°$, and $90°$ of knee flexion. Strain energy is color coded from *green* to *red*, the lines indicate local fiber orientation.

6 Discussion

The comparison of our FE model to FEBio results in average node positioning errors <1% for the intended application, which we regard as sufficient accuracy. As a comparison to FEBio without Augmented Lagrangian reveals, the discrepancies are mainly due to the different approach to volume conservation. Our method to estimate fiber orientations requires only minimal interaction for the definition of attachment areas (which are required in any case) and delivers mostly convincing results. However, some problems occur at the attachment areas, where orientation cannot be determined reliably when the centerline does not start at the mesh boundary. While the obtained framerate is not yet suitable for real-time simulation, it is nonetheless much faster than classic FE solvers. Indeed, the largest challenge we see for future virtual surgeries is not the performance of the FE model, but the generation of accurate subject-specific geometries: ligaments are hardly visible in standard MRI data, and small variations in the segmentation can affect simulation results considerably. As a next step, we plan to validate the presented methods against experimental studies on real ligament tissue.

References

1. Woo, S.L.Y., Debski, R.E., Withrow, J.D., Janaushek, M.A.: Biomechanics of knee ligaments. The American Journal of Sports Medicine, 27(4), 533–543 (1999)

2. Chen, J.X., Wechsler, H., Pullen, J.M., Zhu, Y., MacMahon, E.B.: Knee surgery assistance: patient model construction, motion simulation, and biomechanical visualization. IEEE Transactions on Biomedical Engineering, 48(9), 1042–1052 (2001)

3. Ramaniraka, N.A., Saunier, P., Siegrist, O., Pioletti, D.P.: Biomechanical evaluation of intra-articular and extra-articular procedures in anterior cruciate ligament reconstruction: a finite element analysis. Clinical Biomechanics, 22, 336–343 (2007)

4. Ellis, B.J., Lujan, T.J., Dalton, M.S., Weiss, J.A.: Medial collateral ligament insertion site and contact forces in the ACL-deficient knee. Journal of Orthopaedic Research, 24(4) 800–810 (2006)

5. Fernandez, J.W., Hunter, P.J.: An anatomically based patient-specific finite element model of patella articulation: towards a diagnostic tool. Biomechanics and Modeling in Mechanobiology, 4, 20–38 (2005)

6. Weiss, J.A., Maker, B.N., Govindjee, S.: Finite element implementation of incompressible, transversely isotropic hyperelasticity. Computer Methods in Applied Mechanics and Engineering, 135, 107–128 (1996)

7. Pioletti, D.P., Rakotomanana, L.R., Benvenuti, J.F., Leyvraz, P.F.: Viscoelastic constitutive law in large deformations: application to human knee ligaments and tendons. Journal of Biomechanics, 31, 753–757 (1998)

8. Wu, W., Heng, P.A.: An improved scheme of an interactive finite element model for 3D soft-tissue cutting and deformation. The Visual Computer, 21, 707–716 (2005)

9. Picinbono, G., Delingette, H., Ayache, N.: Non-linear anisotropic elasticity for real-time surgery simulation. Graphical Models, 65, 305–321 (2003)

10. Teran, J., Sifakis, E., Blemker, S.S., Ng-Thow-Hing, V., Lau, C., Fedkiw, R.: Creating and simulating skeletal muscle from the visible human data set. IEEE Transactions on Visualization and Computer Graphics, 11(3), 317–328 (2005)

11. Joldes, G.R., Wittek, A., Miller, K.: Suite of finite element algorithms for accurate computation of soft tissue deformation for surgical simulation. Medical Image Analysis, 13(6), 912–919 (2009)

12. Taylor, Z.A., Comas, O., Cheng, M., Passenger, J., Hawkes, D.J., Atkinson, D., Ourselin, S.: On modelling of anisotropic viscoelasticity for soft tissue simulation: Numerical solution and GPU execution. Medical Image Analysis, 13(2), 234–244 (2009)

13. Delingette, H.: Triangular springs for modeling nonlinear membranes. IEEE Transactions on Visualization and Computer Graphics, 14(2), 329–341 (2008)

14. Bower, A.F.: Applied mechanics of solids. CRC, Boca Raton, FL (2009)

15. Weiss, J.A., Gardiner, J.C.: Computational modeling of ligament mechanics. Critical Reviews in Biomedical Engineering, 29(4), 1–70 (2001)

16. Bouix, S., Siddiqi, K., Tannenbaum, A.: Flux driven automatic centerline extraction. Medical Image Analysis, 9, 205–221 (2005)

17. Allard, J., Cotin, S., Faure, F., Bensoussan, P.J., Poyer, F., Duriez, C., Delingette, H., Grisoni, L.: SOFA – an open source framework for medical simulation. In: Medicine Meets Virtual Reality (MMVR'15). Long Beach, USA (2007)

18. Baraff, D., Witkin, A.P.: Large steps in cloth simulation. In: Proceedings of the SIGGRAPH, pp. 43–54 (1998)

Chapter 13
Ergonomic Assessment of Hand Movements in Laparoscopic Surgery Using the CyberGlove®

Francisco M. Sánchez-Margallo, Juan A. Sánchez-Margallo, José B. Pagador, José L. Moyano, José Moreno, and Jesús Usón

Abstract The main objective of this chapter is the automation of the ergonomic assessment of the wrist's positions, through biomechanics analysis techniques, specifically using the rapid upper limb assessment (RULA). So, this allows establishing new use and design guidelines of the laparoscopic instruments, in order to reduce the influence of risk factors in the wrist area, which are associated with forced positions during the development of laparoscopic activities.

The movements of the right wrist of the surgeons have been recorded with CyberGlove® data glove, during basic laparoscopic tasks. The obtained data were processed according to an adaptation of the ergonomic assessment of the RULA method.

The results of the study show the virtual glove is a useful and fast tool to determine the adoption of forced positions of the surgeons' wrist. These positions mean a high risk to suffer from muscle alterations. For this reason, setting out improvements in the use and design of the current laparoscopic instruments is considered indispensable.

Keywords Ergonomics · Laparoscopy · RULA method · CyberGlove® · Wrist joint · Laparoscopic instruments

1 Introduction

The laparoscopic surgery emerged 20 years ago, and currently it is firmly introduced in the surgical practice. The laparoscopic surgery stresses versus the open surgery, owing to its numerous advantages in patients' recovery, although it presents several inconveniences for the surgeon: lack of spatial depth and tactile

F.M. Sánchez-Margallo (✉)
Department of Laparoscopic Surgery, Minimally Invasive Surgery Centre Jesús Usón, Cáceres, Spain
e-mail: msanchez@ccmijesususon.com

sensation and adoption of forced positions, which mean a high level of muscle–
skeletal stress. Consequently, the development of ergonomics studies on design and
use of laparoscopic instruments is really important.

In this study, we try to create an automatic technique for analysis of wrist's posi-
tions. Taking as starting point the subjective usual techniques of ergonomic study (as
video-based analysis) and the objectives ones (as goniometry and the electromyog-
raphy analysis), we used a recording device of data (CyberGlove®) as alternative
method. This device allows recording the movements of the wrist joints for later
analysis.

This methodology of ergonomic assessment means the union of the advantages
of the objectiveness, speed (improving the video-based analysis), and functionality
(less instruments and more comfort for the surgeon than the goniometry).

1.1 Aims

The main objective of this study is the automation of data collection relating to the
angles of flexion and extension of the wrist during the performance of basic laparo-
scopic tasks and their subsequent analysis by the ergonomic method of assessment
RULA [1]. This is achieved using the CyberGlove® data glove.

This study also analyzes the influence of five types of laparoscopic instruments
in flexion–extension of the wrist joint, both at rest and during performance of
laparoscopic tasks.

1.2 Previous Research Works with the CyberGlove®

The CyberGlove® has been present in several clinical and technology research
projects. This device has mainly been used in developing virtual reality systems
[2–5] and the study of hand movements in the use of hand tools [6–8].

Finally, the research has been focused on the development of the virtual reality
systems for the rehabilitation of patients with brain injuries [9, 10] and the devel-
opment of virtual reality systems to assist surgeons in planning surgery [11, 12] in
clinical field.

2 Tools and Method

The data of the ergonomic study have been recorded for a sample of 17 surgeons
between 28 and 50 years old, with levels of medium and high experience in laparo-
scopic surgery. The maneuvers of laparoscopic cutting, dissection, and suturing
were carried out in a physical simulator (SIMULAP-IC05®, CCMIJU, Cáceres,
Spain). During these activities, the movements of the right hand were recorded,
both the wrist and the rest of joints, using the CyberGlove®.

2.1 SIMULAP-IC05 Features

To standardize the study in a controllable and reproducible environment, we have used the physical laparosocopic simulator SIMULAP-IC05®, which is mainly dedicated to the learning of laparoscopic maneuvers with some technical difficulty (vascular anastomosis, Nissen funduplicature, radical prostatectomy, etc.). This training device simulates the abdominal cavity and has a transparent plastic cover that allows the introduction of trocars to handle the instruments.

The surgeon follows the maneuvers performed through the transparent top cover or through the images projected on screens when using the laparoscopic camera integrated in this device [13, 14].

2.2 The CyberGlove® Features

CyberGlove® is a device with a sensor package of conductive material, its resistance varies with the flexion and allows registering the movements of the fingers and wrist joints.

The model of CyberGlove® used in this study has 18 sensors which record the metacarpophalangeal and interphalangeal deviation of the fingers, the distance among them, the turning of the thumb and the little finger with respect to the palm of the hand, and flexion–extension and ulna–radial deviation of the wrist.

Maximum speed is 114 kBaud sampling (100 samples of each sensor per second) and is connected to the computer via the RS232 serial port [15].

2.3 Clinical Evaluation Characteristics

Perspectives have been derived from the work area using two video cameras: one with front view and another with left lateral view of the surgeon to be able to compare, in future research, the results obtained with a video metric analysis.

One right hand CyberGlove® is used, which was previously calibrated according to the anatomical characteristics of each surgeon's hand. For data acquisition, how to grip the instrument is analyzed, according to two criteria: the neutral position or at rest, and during the performance of laparoscopic tasks (Fig. 13.1). The instrumental group chosen includes scissors, dissector, and three models of laparoscopic needle holders (curved, straight, and straight with rings).

We define as resting or neutral position, that position of the gripping instrument, which is considered by each surgeon as ergonomics and it is associated with less muscle-skeletal stress for him.

The data are recorded during the tasks of cutting sheet of latex with laparoscopic scissors, the dissection of the gastric serous layer with laparoscopic dissector, and suturing in laparoscopic sheet of latex using three different models of laparoscopic needle holder.

Fig. 13.1 Positions of the surgeon's hand during the recording of data using the CyberGlove®

The time data recording was 5 s for each neutral position and 1 min for each laparoscopic task. The data recording of each laparoscopic task has been taken for the same surgical position for each surgeon.

2.4 RULA Method

For the assessment of risk associated with postural load there are several methods, each one with a scope of application and different results [16–18]. The RULA method, chosen for such experiments, was developed by doctors *McAtammey* and *Corlett* in 1993 to assess the risk factors in workers, which may cause disturbances in the upper limbs of the body: postures, repetitiveness of movement, static activity of the skeletal muscle system, and so on.

We rely on this method for ergonomic evaluation of the wrist in the grip of basic laparoscopic instrumentation.

The RULA method divides its evaluation into two corporal groups: group A, which includes the upper limbs (arms, wrists and forearms), and group B, which covers the legs, trunk, and neck. In our case, the assessment will only focus on the wrist joint, included in the group of upper limbs of the body.

The evaluation of a specific position of a subject with this method only makes sense, if one takes into account both the joint group of upper and lower members.

2.5 Computer Application

To carry out the ergonomic study, we developed a software application on the Microsoft® Visual C++ 2005® platform.

This application analyzes and interprets the degree of flexion–extension of each of the joints of the hand obtained by the data glove. Similarly, it allows the display
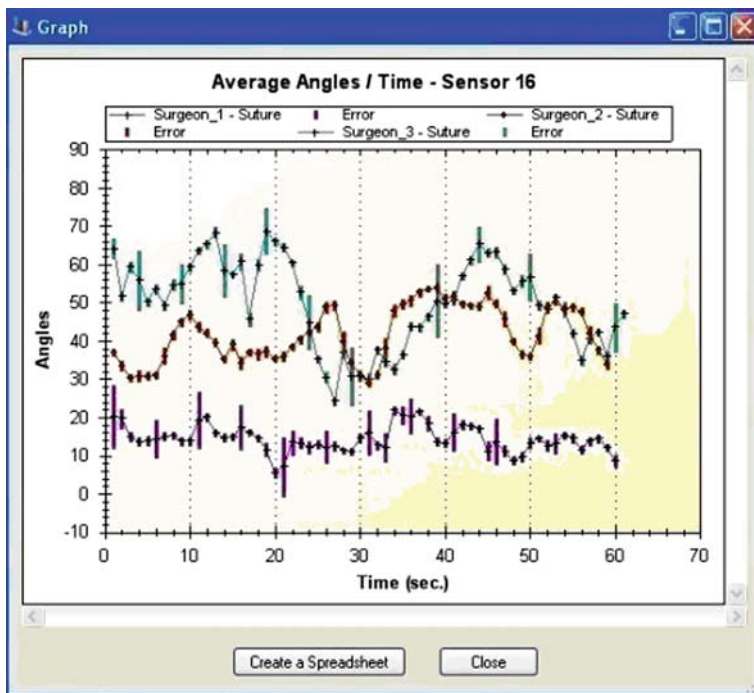
Fig. 13.2 Comparative chart of the angles described by the wrist of three surgeons during the development of laparoscopic suturing in latex using a curved needle holder

of charts of evolution in the degrees of each of the joints and the comparison among different surgeons during a surgical task (Fig. 13.2).

Another utility of the computer application is the automatic comparison of the wrist joint information, using RULA score regarding the flexion–extension wrist movements.

2.6 Data Analysis

We used the arithmetic mean of the degrees of motion (angular average value), with its corresponding error for each sensor. Because we work with a range of positive values, it was not necessary to use the effective value on the sample data [19].

The arithmetic average of the wrist angle of the sample of surgeons has been calculated for each instrumental in his neutral and active position. An analysis of variance (ANOVA) has been conducted for comparison of the values obtained in both positions. The level of significance was set at $p < 0.05$.

3 Results

The typical rating of the RULA method, with respect to flexion–extension of the wrist, has been adapted to the positive range of angles used, which will depend on the values provided by the CyberGlove$^®$ (Table 13.1). This range of angles is between 0° and 120°, but it can vary from one subject to another depending on his anatomical features. We consider a score between 1 and 2 as an acceptable extension–flexion of the wrist and a 3 score as inappropriate.

Table 13.1 Adaptation of the RULA method regarding the wrist, for the values obtained from the CyberGlove$^®$

Score	Position
1	If the flexion–extension angle is 60° ± 3°
2	If the wrist is flexed or extended between 45° and 75°, except for the score 1 case
3	If the flexion–extension is greater than 75° or below 45°

Our results (Table 13.2) showed that there is no statistical evidence of relationship between neutral position and the active position for each instrument.

Table 13.2 Comparison of the wrist flexion–extension angle (mean value ± standard deviation) in the neutral position and active position

Laparoscopic instruments	Neutral position	Active position	Significance level
Scissors	19.63 ± 0.65	16.42 ± 1.36	NS
Dissector	26.48 ± 0.77	24.97 ± 1.57	NS
Needle holder	36.41 ± 0.98	35.31 ± 1.95	NS
Axial handle	32.96 ± 1.04	36.64 ± 2.03	NS
Pistol handle	43.52 ± 0.99	42.42 ± 1.98	NS
Ring axial handle	32.74 + 0.90	26.87 + 1.82	NS

NS = not significant

4 Discussion

The necessary applications have been generated to acquire and analyze the degrees of flexion–extension of the wrist and its harmonization with the RULA values.

For all laparoscopic instruments analyzed, most surgeons have unfavorable angles of flexion–extension, both in the neutral position and during the performance of basic laparoscopic tasks.

There has been no statistical evidence of relationship between the neutral or at rest positions, which we consider adequate, and the active position for the wrist angle for each instrument. Consequently, we cannot determine whether adverse angles obtained in most cases are due to an incorrect grip of the tool by the surgeon or the improper design of the instruments used.

Because we used a sample of 17 expert surgeons in laparoscopic surgery, this leads us to focus future works on improving ergonomics in the design of such instruments.

4.1 Future Researches

Within the lines of future work arising during the development of this work, the validation of this technique over other more established techniques, the consideration of the ulna–radial deviation, and the inclusion of a spatial position sensor to assess the twist of the wrist remain.

References

1. McAtamney, L., Corlett, E.: RULA: a survey method for the investigation of work-related upper limb disorders. Applied Ergonomics, 24, 91–99 (1993)
2. De Bonnefoy, N., Jessel, J.: A mixed reality system for design engineering: thinking, issues and solutions. MIXER 2004: workshop on exploring the design and engineering of mixed reality systems, Funchal, Island of Madeira, Portugal (2004)
3. Yun, M.H., Cannon, D., Freivalds, A., Thomas, G.: An instrumented glove for grasp specification in virtual-reality-based point-and-direct telerobotics. IEEE Transactions on Systems Man and Cybernetics Part B-Cybernetics, 27, 835–846 (1997)
4. Bloomfield, A., Deng, Y., Wampler, J., Rondot, P., Harth, D., McManus, M., Badler, N.: A taxonomy and comparison of haptic actions for disassembly tasks. IEEE Virtual Reality 2003, Proceedings, pp. 225–231 (2003)
5. Wong, J.P.Y., Lau, R.W.H., Ma, L.Z.: Virtual 3D sculpting. Journal of Visualization and Computer Animation, 11, 155–166 (2000)
6. Grinyagin, I.V., Biryukova, E.V., Maier, M.A.: Kinematic and dynamic synergies of human precision-grip movements. Journal of Neurophysiology, 94, 2284–2294 (2005)
7. Yun, M.H., Eoh, H.J., Cho, J.: A two-dimensional dynamic finger modeling for the analysis of repetitive finger flexion and extension. International Journal of Industrial Ergonomics, 29, 231–248 (2002)
8. Chao, A., Kumar, A., Emery, C., Nagarajarao, K., You, H.: An ergonomic evaluation of Cleco pliers. Human Factors and Ergonomics Society Annual Meeting Proceedings, 44, 441–442 (2000)
9. Jack, D., Boian, R., Merians, A.S., Tremaine, M., Burdea, G.C., Adamovich, S.V., Recce, M., Poizner, H.: Virtual reality-enhanced stroke rehabilitation. IEEE Transactions on Neural Systems and Rehabilitation Engineering, 9, 308–318 (2001)
10. MacDonald, P.A., Paus, T.: The role of parietal cortex in awareness of self-generated movements: A transcranial magnetic stimulation study. Cerebral Cortex, 13, 962–967 (2003)
11. Montgomery, K.N.: VERS – A virtual environment for reconstructive surgery planning. Stereoscopic Displays and Virtual Reality Systems Iv, 3012, 487–492 (1997)
12. Stalfors, J., Kling-Petersen, T., Rydmark, M., Westin, T.: Haptic palpation of head and neck cancer patients – Implications for education and telemedicine. Medicine Meets Virtual Reality 2001: Outer Space, Inner Space, Virtual Space, 81, 471–474 (2001)
13. Usón, J., Sánchez, F., Pascual, S., Climent, S.: Formación en Cirugía Laparoscópica Paso a Paso. Centro de Cirugía de Mínima Invasión (2007)
14. Sánchez-Margallo, F.M., Díaz-Güemes, I., Pérez, F.J., Sánchez, M.A., Loscertales, B., Uson, J.: Preliminary results with a training program for thoracoscopic atrial fibrillation therapy. Surgical Endoscopy, 23, 1882–1886 (2008)

15. Muñoz, J.: ErgoRec: Simulación Mediante Realidad Virtual de la Ergonomía con un Guante de Datos. Universidad de Extremadura, Cáceres (2005)
16. Nignett, S., McAtammey, L.: REBA: rapid entire body assessment. applied ergonomics, 31, 201–205 (2000)
17. Waters, T.R., Putz-Anderson, V., Garg, A., Fine, L.J.: Revised NIOSH euation for the design and evaluation of manual lifting task. Ergonomics, 7, 36 (1993)
18. Karhu, S., Kansi, P., Kuorinka, L.: Correcting working postures in industry: A practical method for analysis. Applied Ergonomics, 8, 199–201 (1977)
19. Nunes, I.L.: Quantitative method for processing objective data from posture analysis. In: Karwowski, W. (ed.): International encyclopedia of ergonomics and human factors, Vol. 3. University of Louisville, Kentucky, USA (2006)

Chapter 14
Effects of Fetal Head Motion on Pelvic Floor Mechanics

Xinshan Li, Jennifer A. Kruger, Martyn P. Nash, and Poul M.F. Nielsen

Abstract We have developed a modelling framework to simulate vaginal delivery using individual-specific pelvic floor geometries derived from magnetic resonance images, which could potentially be used to study the effect of various contributing factors (such as muscle mass and muscle tone) on the childbirth process. One important goal of this is to faithfully represent the path of the fetal head as it descends through the maternal pelvis. Previous studies have prescribed or restricted the path of the fetal head. In this study, we investigate the effect of the fetal head motion on the mechanical response of the pelvic floor muscle by applying three types of constraints to the fetal head: (1) a completely prescribed head path; (2) allowing rotation about one point on the head; and (3) a minimally constrained head, allowing both rotation and translation. The results were analysed by comparing the normalised reaction forces exerted on the fetal head and the maximum principal stretch ratios of the pelvic floor muscles. The reaction forces for case (3) were markedly reduced compared to cases (1) and (2), indicating that the path of the fetal head has significant influence on the force required to achieve delivery. These results also indicate that models should use a minimally constrained fetal head so that its path is determined by the geometry of the head and the pelvic floor. Future work will introduce nonlinearity and anisotropy into the pelvic floor muscles and use this modelling framework to compare the mechanical response between athlete and non-athlete in order to determine the factors that contribute to difficulties during the second stage of labour for athletic mothers.

Keywords Pelvic floor mechanics · Fetal head motion · Finite element method · Second stage of labour

1 Introduction

The series of motions of the fetus during the second stage of labour are known collectively as the mechanism of labour. These movements, including descent, flexion,

X. Li (✉)
Auckland Bioengineering Institute, The University of Auckland, Auckland, New Zealand
e-mail: shannon.li@auckland.ac.nz

internal rotation, extension and external rotation [1], take place in sequence as the fetus adapts to the geometry of the maternal pelvis. Early observations of these movements were reported in 1793 by William Smellie as a set of anatomical tables [2]. They were later confirmed by Borell and Fernstrom through their radiography studies on women in labour [3–7]. These studies have built up our current understanding of the labour mechanism that the fetal head path is determined primarily by the size and shape of the bony pelvis and the fetal head, with additional influences from the pelvic floor muscles and the surrounding soft tissues. The pelvic floor muscles consist of the iliococcygeus, the pubococcygeus and the puborectalis, which are known collectively as the levator ani (LA) muscle group.

In recent years, several groups have modelled the second stage of labour using finite element methods [8–11]. However, the main focus has been on the injury mechanism of the LA during a vaginal delivery. Few have investigated the movement of the fetal head during the process. Most childbirth models have completely prescribed the path of the fetal head based on descriptions in the literature. For example, Martins et al. simulated the movements of the fetal head (engagement, descent, flexion, internal rotation and extension) by controlling the movement of several points on the fetal head mesh [8]; Lien et al. and Hoyte et al. displaced the head along the curve of Carus [9,10]. However, the path of the fetal head is highly dependent on the individual-specific geometries of the bony pelvis, the pelvic floor muscles and the fetal head itself. It is important to be able to reproduce the fetal head path with minimal constraints in order to objectively assess the risk of damage on an individual-specific basis.

In this Chapter, we present our simulation results of a vaginal birth using three different types of fetal head constraints. The geometries of the pelvic floor muscles and the bony pelvis were obtained from a healthy nulliparous woman (who has never given birth). Isotropic (Mooney–Rivlin) hyperelastic material descriptions were used for the pelvic floor structures and the fetal head. The force exerted on the head and the overall maximum principal stretch ratios of the pelvic floor were compared to show that the fetal head path has significant influence on the stress response of the pelvic floor muscles.

2 Method

2.1 Finite Element Model Creation

The pelvic floor model was created from a set of magnetic resonance images obtained from a previous study [12]. The images were acquired using a 3D TSE Siemens SPACE sequence 1 mm × 1 mm × 1 mm with a Siemens Magnetom Avanto 1.5T scanner. Major pelvic floor muscles and the bony pelvis were segmented and fitted using tricubic Hermite meshes (hexahedral elements) [13].

The fetal head surface data was obtained by Lapeer et al., in which a skull replica produced by ESP Ltd was scanned [14]. A bicubic linear mesh (hexahedral elements with linear interpolation through the thickness) was fitted to the surface data and a

constant thickness was applied. For simplicity, the face was excluded from the mesh as it is typically not in direct contact with the pelvic floor structures during the second stage of labour.

Figure 14.1 shows the model used for our simulation. The pelvic floor model (4,896 degrees of freedom) consists of three components: the levator ani in yellow, the support mesh, which includes part of the obturator internus and obturator fascia in brown, and part of the pubis in silver. The fetal head mesh (1,344 degrees of freedom) has a biparietal diameter of 90 mm and a suboccipitofrontal diameter of 100 mm.

Fig. 14.1 Anterior views of the pelvic floor on the *left* with the levator ani (*yellow*), support mesh (*brown*) and pubis (*silver*) and the fetal head in an occiput anterior position on the *right*. The axes show positive *y*-direction into the page
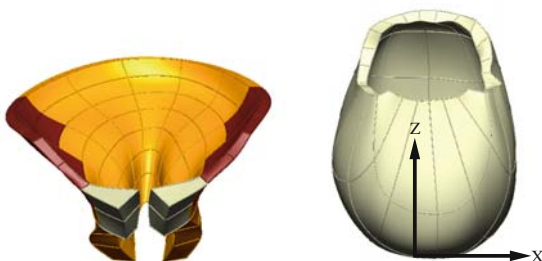
2.2 Mechanical Constraints

The fetal head was presented occiput anteriorly as it engaged with iliococcygeus. It was then displaced through the LA under three different constraint scenarios until the biparietal diameter was passed through the maternal pelvis. The three scenarios are (1) a completely prescribed head path; (2) allowing rotation about one point on the head; and (3) a minimally constrained head, allowing both rotation and translation. In case (1), the head was translated straight down by prescribing the vertical displacements at the top nodes. In case (2), the vertical displacement of the lowest internal node was prescribed and the head was allowed to rotate about this point. In case (3), the fetal head was free to rotate and translate in both *x*-and *y*-directions and only the *z* displacement at the lowest internal point was prescribed.

The head was displaced through the LA over a series of steps. The descent of the fetal head was measured as the distance between the lowest point of the head and the line joining the ischial spines according to obstetrical convention. It was defined as positive when the lowest point was below the ischial spines.

The LA muscle was fixed at its attachment to the coccyx and the support mesh was fixed bilaterally at the attachment points to the bony pelvis. The pubis was fixed along the line of pubis symphasis.

2.3 Mechanics Simulation Framework

Frictionless contact interaction between the fetal head and the pelvic floor muscles was modelled using finite deformation hyperelasticity coupled with contact

mechanics cross-constraints [15]. The algorithms described below were implemented using in-house software CMISS[1] [16,17].

The deformation of a body can be described using the Lagrange strain tensor $\mathbf{E}$ and the right Cauchy–Green deformation tensor $\mathbf{C}$:

$$\mathbf{E} = \frac{1}{2}(\mathbf{C} - \mathbf{I}), \tag{1}$$

where $\mathbf{C} = \mathbf{F}^T\mathbf{F}$ is determined from the deformation gradient tensor $\mathbf{F}$, which relates reference coordinates $\mathbf{X}$ and deformed coordinates $\mathbf{x}$. Polar decomposition expresses $\mathbf{F}$ as the product of a rotation tensor $\mathbf{R}$ and a stretch tensor $\mathbf{U}$. The eigenvalues λ_i ($i = 1, \ldots, 3$) of $\mathbf{U}$ are the principal stretch ratios.

The governing equation of finite elasticity can be derived from stress equilibrium [15]:

$$\delta\mathrm{W} = \int_V \boldsymbol{\sigma} : \frac{\partial(\delta\mathbf{u})}{\partial\mathbf{x}} dV - \int_V \mathbf{b} \cdot \delta\mathbf{u} dV - \int_S \mathbf{t} \cdot \delta\mathbf{u} dS, \tag{2}$$

where $\boldsymbol{\sigma}$ is the Cauchy stress tensor, $\delta\mathbf{u}$ is the field of virtual displacements, $\mathbf{b}$ is the body force (per unit mass) and $\mathbf{t}$ is the surface traction vector. The integrals are performed over the reference volume V and its bounding surface S. $\boldsymbol{\sigma}$ can be derived from the constitutive equation by differentiating the strain energy density function Ψ with respect to $\mathbf{E}$, then transforming the resulting Lagrangian stress tensor using $\mathbf{F}$. In this study, a second–order Mooney–Rivlin hyperelastic material description was assumed:

$$\Psi = c_{10}(I_1 - 3) + c_{20}(I_1 - 3)^2, \tag{3}$$

where $I_1 = tr(\mathbf{C})$ is the first principal invariant of $\mathbf{C}$ and $c_{10} = 2.5$ kPa, $c_{20} = 0.625$ kPa for the pelvic floor muscles [18]. The values for c_{10} and c_{20} were assumed to be 500 times and 1,000 times larger for the fetal head and the pubis, respectively, because they are much stiffer than the muscle. The simulation results are insensitive to this factor (confirmed by rigid body motion).

The principal of virtual work for coupled contact mechanics is defined as follows:

$$\delta\mathrm{W}^{\text{coupled}} = \sum_{i=1}^2 \delta\mathrm{W}^{(i)} + \int_{S_c^{(1)}} (t_N\delta g_N) \, dS_c^{(1)}, \tag{4}$$

where i is the index denoting the two bodies in contact: $i = 1$ is the slave (pelvic floor) and $i = 2$ is the master (fetal head); t_N is the contact pressure calculated using

---

[1]An interactive computer program for *C*ontinuum *M*echanics, *I*mage analysis, *S*ignal processing and *S*ystem Identification, http://www.cmiss.org/

the penalty method; and δg_N is the variation in gap function. The integration is performed over the surface of the slave mesh $S_c^{(1)}$.

3 Results

The motion of the fetal head for case (3) is illustrated in Fig. 14.2 in the anterior view (x–z orientation; left column), the right lateral view (y–z orientation; middle column) and the superior view (x–y orientation; right column) at four load steps (a–d). The dashed line represents the location of the ischial spines. The fetal head displacements at its centre of mass relative to the initial x, y positions are plotted at the bottom. Significant motion was observed in the y-direction. The amount of shift in the x-direction was relatively minor. In contrast, little motion was observed in the x-and y-directions in case (2) when the only motion permitted was rotation about a fixed point (data not shown).

   Two parameters were compared to investigate the effect of different fetal head constraints on the simulation: the force required for delivery and the maximum principal stretch ratio in the LA.

   The force required for delivery was estimated by summing the reaction forces on the pelvic floor. These values were normalised with respect to the peak value found in case (1). Figure 14.3 shows the evolution of the sum of normalised reaction forces (total) as the fetal head descends. Considerable forces were present as a result of the fixed head path in the x-and y-directions for cases (1) and (2) (data not shown). A much lower total force was required to push the fetus out for the minimally constrained head in case (3).

   The maximum principal stretch ratio was found at the right LA attachment point to pubis in all three cases. Figure 14.4 shows the principal stretch ratio in this region for the three different head constraint scenarios. The amount of stretch was almost identical for cases (1) and (2), with small variations for case (3). Overall, the maximum principal stretch ratio was found to be 2.6 for cases (1) and (2) and 2.7 for case (3).

4 Discussion

To the authors' knowledge, this is the first childbirth model where the fetal head path is determined by the geometries of the pelvic floor and the head. From the plot of reaction force versus fetal head descent (Fig. 14.3), we can see that by applying minimal constraints (fixing only 1 degree of freedom) on the fetal head, and hence letting the head determine the minimum energy state, a markedly lower (-25%) overall force was required for birth. By contrast, adding rotation to the fetal head, as in case (2), did not markedly alter model predictions compared to case (1).

   A wide variation of maximum principal stretch ratios were previously reported [8–10], with values ranging from 1.6 to 3.5. We have found similar maximum
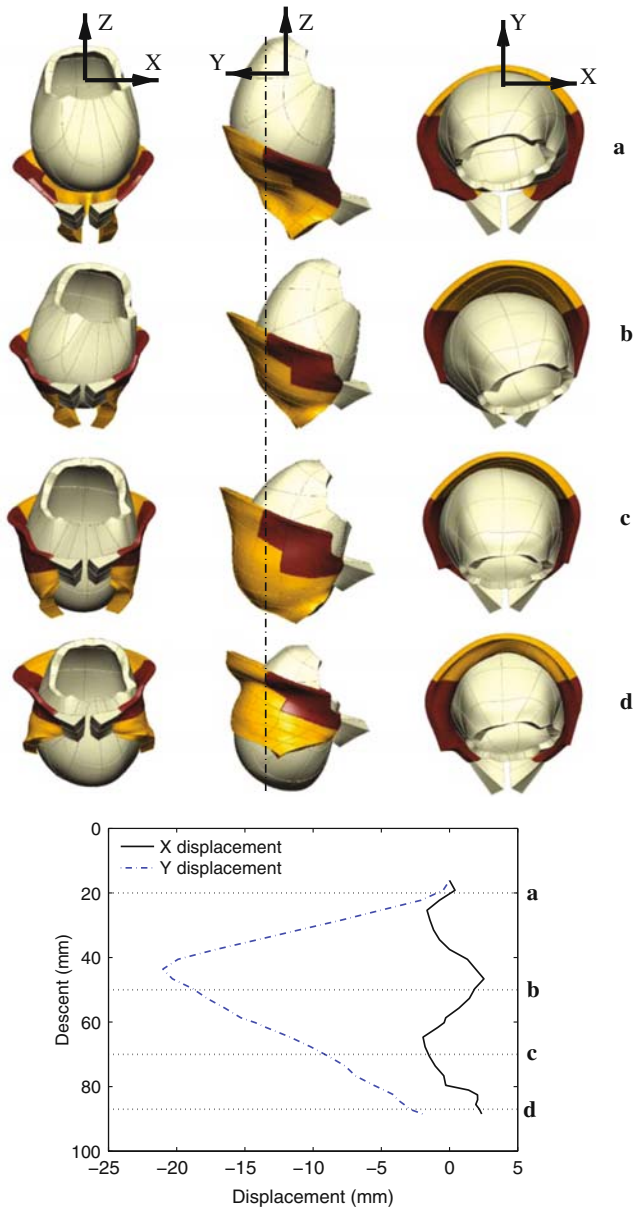
Fig. 14.2 The sequence of fetal head motion in case (3) is shown on *top*, at four different stages: *a*, *b*, *c* and *d*. The relative displacements of the centre of mass in the *x*-and *y*-directions with respect to their initial values are plotted against fetal head descent at the *bottom*

Fig. 14.3 Plots of the total normalised reaction forces versus fetal head descent for constraint scenarios (1), (2) and (3)
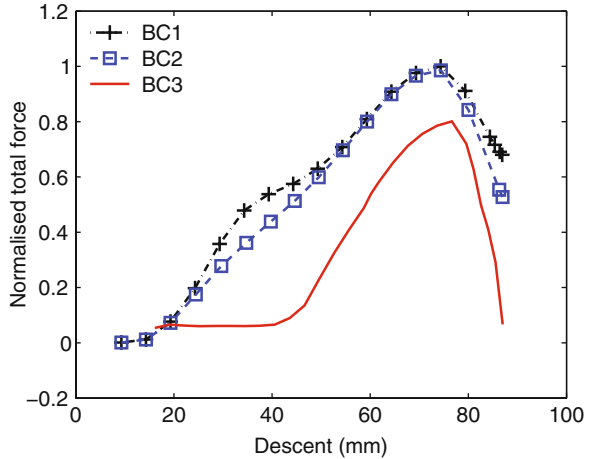
Fig. 14.4 Principal stretch ratio at the right LA attachment for three different constraint scenarios against fetal head descent
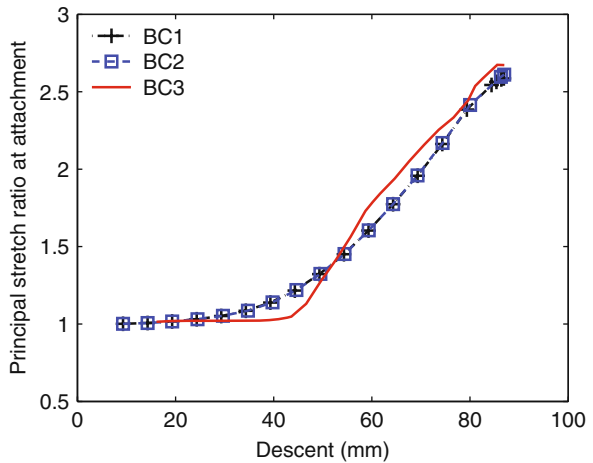
stretch ratios for the head constraint scenarios considered in this study. This may be explained by the fact that the same fetal head was used for all three cases and the position of the fetal head with respect to the pelvic floor was similar when the maximum principal stretch ratio was reached (OA position with the neck directly under the symphysis pubis).

Although this model offers significant improvements compared to our previous study [11], there are still limitations that need to be addressed to further improve our modelling framework. We assumed that the LA was isotropic (Mooney–Rivlin) and acted passively as the fetal head passed through. In reality, the LA muscle group has distinct muscle fibre structures. This indicates the importance of introducing fibre

anisotropy into the LA muscle and incorporating possible muscle activation during the simulation.

Fetal head moulding is another factor that determines the kinematics of the LA muscle during childbirth. Moulding occurs when the fetal skull changes shape due to forces exerted by the surrounding tissue during labour. This change in geometry will alter the fetal head path as well as the mechanical response of the LA muscle. Several studies have modelled fetal head moulding. However, none has simultaneously combined this process with pelvic floor deformations. We plan to incorporate these factors into our modelling framework so that more realistic boundary constraints can be used to simulate the second stage of labour.

The long-term goal of this project is to assist clinicians to better understand the mechanism of labour and the role of pelvic floor muscles during a vaginal delivery.

References

1. Varney, H., Kriebs, J.M., Gegor, C.L.: Varney's midwifery, 14th Ed. Jones and Bartlett Pub., Sudbury (2004)
2. Smellie, W., Hamilton, A.: A set of anatomical tables, with explanations: and an abridgment of the practice of midwifery. London (1793)
3. Borell, U., Fernstrom, I.: Shape and course of the human birth canal–a radiographic study in the human. Acta Obstetricia et Gynecologica Scandinavica, 36, 166–179 (1957b)
4. Borell, U., Fernstrom, I.: The movements in the mechanism of disengagement with special reference to the attitude of the foetal head. Acta Obstetricia et Gynecologica Scandinavica, 36, 347 (1957c)
5. Borell, U., Fernstrom, I.: Radiographic studies of the rotation of the foetal shoulders during labour. Acta Obstetricia et Gynecologica Scandinavica, 37, 54–61 (1958)
6. Borell, U., Fernstrom, I.: Internal anterior rotation of the foetal head–a contribution to its explanation. Acta Obstetricia et Gynecologica Scandinavica, 38, 103–109 (1959)
7. Borell, U., Fernstrom, I.: The mechanism of labour. Radiologic Clinics of North America, 5, 73–85 (1967)
8. Martins, J.A.C., Pato, M.P.M., Pires, E.B., Jorge, R.M.N., Parente, M., Mascarenhas, T.: Finite element studies of the deformation of the pelvic floor. Annals of the New York Academy of Sciences, 1101(1), 316–334 (2007)
9. Lien, K., Mooney, B., DeLancey, J.O.L., Ashton-Miller, J.A.: Levator ani muscle stretch induced by simulated vaginal birth. The American College of Obstetricians and Gynecologists, 103(1), 31–40 (2004)
10. Hoyte, L., Damaser, M.S., Warfield, S.K., Chukkapalli, G., Majumdar, A., Choi, D.J., Trivedi, A., Krysl, P.: Quantity and distribution of levator ani stretch during simulated vaginal childbirth. American Journal of Obstetrics & Gynecology, 199(2), 198.e1–198.e5 (2008)
11. Li X., Kruger, J., Chung, J., Nash, M.P., Nielsen, P.M.F.: Modelling childbirth: Comparing athlete and non-athlete pelvic floor mechanics. In: Lecture Notes in Computer Science: Medical Image Computing and Computer-Assisted Intervention MICCAI 2008. Springer, Berlin/Heidelberg, pp.750–757 (2008)
12. Kruger, J.A., Heap, S.W., Murphy, B.A., Dietz, H.P.: Pelvic floor function in nulliparous women using three-dimensional ultrasound and magnetic resonance imaging. Obstetrics & Gynecology, 111(3), 631–638 (2008)
13. Li, X., Kruger, J., Chung, J., Nash, M.P., Nielsen, P.M.F.: Modelling the pelvic floor for investigating difficulties during childbirth. Proceedings of SPIE, 6916(69160 V), (2008)

14. Lapeer, R.J., Prager, R.W.: Fetal head moulding: finite element analysis of a fetal skull subjected to uterine pressures during the first stage of labour. Journal of Biomechanics, 34, 1125–1133 (2001)
15. Laursen, T.A.: Computational contact and impact mechanics, 1st Ed. Springer, Berlin (2002)
16. Chung, J.: Modelling mammographic mechanics. PhD thesis, University of Auckland, New Zealand (2008)
17. Chung, J., Rajagopal, V., Laursen, T.A., Nielsen, P.M.F., Nash, M.P.: Frictional contact mechanics methods for soft materials: application to tracking breast cancers. Journal of Biomechanics, 41(1), 69–77 (2008)
18. Lee, S., Darzi, A., Yang, G.: Subject specific finite element modelling of the levator ani. Medical Image Computing and Computer-Assisted Intervention, 8, 360–367 (2005)

Chapter 15
Novel Monitoring Method of Proximal Caries Using Digital Subtraction Radiography

Jeong-Hoon Park, Yong-Suk Choi, Gi-Ja Lee, Samjin Choi, Ji-Hye Park, Kyung-Sook Kim, Young-Ho Park, and Hun-Kuk Park

Abstract The objective of this study was to mark the points of emphasis in hidden dental caries from 15 subjects' dental X-ray images. Each image is an 8-bit grayscale image taken by digital image radiography. For each caries lesion diagnosed, a mean pixel value was obtained in digital subtraction radiographs using a scale ranging from 0 to 255 gray values. Hence, the purpose of this study was to design a novel detection method of proximal caries, based on pixel gray values in digital subtraction radiography images from a patient's single dental image, used for monitoring of dental caries. As a result, in digital subtraction radiography, the image is used to mark the points of emphasis in hidden dental caries using a novel detection method of proximal caries from a patient's single dental image.

Keywords Proximal caries · Caries monitoring · Pixel subtraction of radiograph · Digital subtraction radiography

1 Introduction

Radiography has been primarily used for the detection of lesions on the proximal surfaces of teeth, which are not clinically visible for inspection, and it is a main diagnostic tool for detecting dental and maxillofacial lesions [1–3]. Radiologic images have two dimensions of three-dimensional reality; the images of different anatomical structures are superimposed on each other and, thus, make it difficult to detect the lesions [2, 4].

The protective outer surface of anatomic crowns is made up of enamel. Dental caries is the disease process of decay in which acid formed from carbohydrate,

H.-K. Park (✉)
Department of Biomedical Engineering, School of Medicine, Kyung Hee University, Seoul 130-702, Republic of Korea; Healthcare Industry Research Institute, Kyung Hee University, Seoul 130-702, Republic of Korea; Program of Medical Engineering, Kyung Hee University, Seoul 130-702, Republic of Korea
e-mail: sigmoidus@khu.ac.kr

aided by *Streptococcus mutans* bacteria, attacks tooth surfaces [5]. Digital sub-traction radiography (DSR) is a method that can resolve deficiencies and increase diagnostic accuracy [6–8]. The subtraction method was introduced by B.G. Ziedes des Plantes in the 1920s. A subtraction image is used to suppress background fea-tures and reduce background complexity, compress the dynamic range, and amplify small differences by superimposing the scenes obtained at different times [9, 10]. Subtraction radiography was introduced into dentistry in the 1980s [6, 11–13]. It is used to compare standardized radiographs taken at sequential examination visits. All unchanged structures are subtracted and these areas are displayed in a neutral gray shade in the subtraction image; regions that have changed are displayed in darker or lighter shades of gray [14–16]. For radiographic dentinal lesions, the frac-tion of surfaces with cavitation has been reported to range between 50 and 90% [17]. Recurrent caries is more accurately detected with subtraction techniques. The dynamic nature of caries remineralization/demineralization also could be explored with reliable digital subtraction techniques [18]. The purpose of this study was to investigate the detection of proximal caries using digital subtraction radiography. The X-ray images of sound and caries teeth of individuals were analyzed. In digital subtraction radiography, the image is used to mark the points of emphasis in hid-den dental caries. Hence, the purpose of this study was to design a novel detection method of proximal caries, based on pixel gray values in digital subtraction radio-graphy images from a patient's single dental image, used for monitoring of dental caries.

2 Materials and Methods

2.1 Tooth Images Selected

Study subjects were chosen from among the patients who were diagnosed as hav-ing proximal dental caries using the intraoral X-ray system at the Dental Medical Center, Kyung Hee University. The purpose of this study was to mark the points of emphasis in hidden dental caries from 15 subjects' dental X-ray images. Each image is an 8-bit grayscale image taken by digital image radiography. The digital radiographs were acquired using an intraoral X-ray system by Heliodent DS (Sirona Dental System GmbH, Bensheim, Germany) and storage phosphor plates by Kodak RVG 6100 system. The digital image receptors were $1,140 \times 1,920$ pixels (dimen-sions of active area: 27×36 mm) with true image resolution, 256 gray levels, and were capable of providing more than 20 lp/mm spatial resolution. The images were extracted in an uncompressed format (Windows jpeg). Each of the images was taken using the system setup with a 12-in. cone operating at 60 kVp, 7 mA, and 0.32 s.

2.2 Pixel Subtraction of Radiographs

The pixel subtraction operator takes two images as input and produces as output a third image whose pixel values are simply those of the first image minus the

corresponding pixel values from the second image. It is also often possible to just use a single image as input and subtract a constant value from all the pixels. Some versions of the operator will just output the absolute difference between pixel values, rather than the straightforward signed output. The subtraction of two images is performed straightforwardly in a single pass. Let I_c, I_m and I_s be the contrast, mask and subtraction images, respectively. A simple image subtraction would be the output pixel values given by

$$I_s(i,j) = |I_c(i,j) - I_m(i,j)| \tag{1}$$

If the operator calculates absolute differences and the two input images use the same pixel value type, then it is impossible for the output pixel values to be outside the range that may be represented by the input pixel type and so this problem does not arise. This is one good reason for using absolute differences. Image subtraction is used both as a substep in complicated image processing sequences, and also as an important operator in its own right. Digital imaging is the result of X-ray interaction with electrons in electronic sensor pixels (picture elements), conversion of analog data to digital data, computer processing, and display of the visible image on a computer screen. Data acquired by the sensor are communicated to the computer in analog form. Computers operate on the binary number system in which two digits (0 and 1) are used to represent data. These two characters are called bits (binary digit), and they form words of 8 or more bits in length called bytes. The total number of possible bytes for 8-bit language is $2^8 = 256$.

2.3 Proposed Novel Method of Image Subtraction

When two radiographs are recorded with at least partly controlled projection angles, the information from the most recent one may be digitally subtracted from that of the former. Optimally, all unchanged anatomical background structures will cancel, and unchanged areas will be displayed in a neutral gray shade in the subtraction image [19]. Areas of mineral loss are conventionally displayed in darker shades of gray, while areas of gain appear lighter than the background. For the detection of caries, subtraction has been used in laboratory studies [20], but the technique may also be applicable for monitoring caries in the clinic. Digital subtraction radiography is a technique that allows us to determine quantitative changes in radiographs. The premise is quite simple. A radiographic image is generated before a particular treatment is performed. At some time after the treatment, another image is generated. The resultant image shows only the changes that have occurred and "subtracts" those components of the image that are unchanged. The magnitude of the changes can then be measured by evaluating the histogram (graphic depiction of the distribution of gray levels) of the resultant image. Direct digital imaging has been a great help in the quest to take the technique of digital subtraction radiography out of the laboratory setting and actually use it clinically.

Fig. 15.1 Novel detection
method of proximal caries
from a patient's single dental
image by digital subtraction
radiography
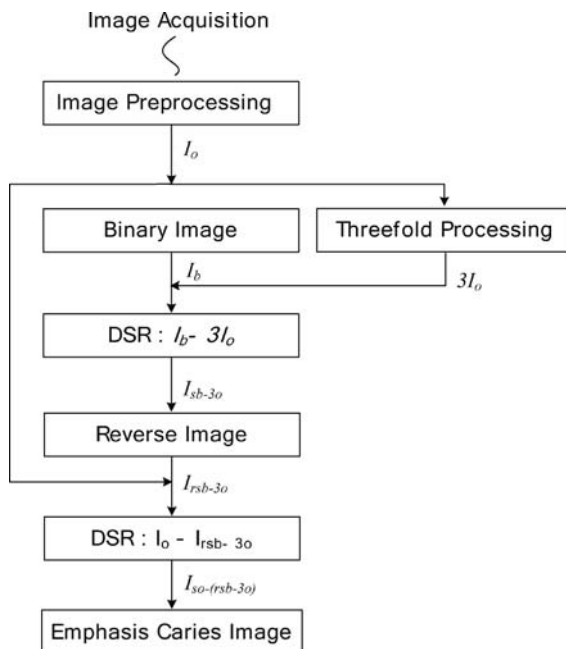
Figure 15.1 shows the flowchart of our novel method for proximal caries detection from a patient's single dental image by digital subtraction radiography. The X-ray dental image is first subjected to image preprocessing. This image preprocessing is used to reduce the background noise from a lookup table and also to prepare the image for further processing such as image subtraction.

After preprocessing the original X-ray image (I_o), dense structures that block the passage of the X-ray beam through the gum, such as the dental bones, appear white while the soft gum tissues that allow the X-ray beams to pass through, such as the skin and muscles, appear darker see Fig. 15.2a original image.

Threefold processing ($3I_o$) is performed on the triploid original image after image preprocessing. The binary image (I_b) is the image of binary information from the original image. Digital subtraction radiography (I_b-3I_o) detects tissue mass changes by subtraction of the triploid original image from the binary image. Reverse image (I_{rsb-3o}) is the reversed image from digital subtraction radiography image (I_b-3I_o). Digital subtraction radiography (I_o-I_{rsb-3o}) detects tissue mass changes by subtraction of the reverse image from the original image.

After generating final digital subtraction radiography, the image (I_o-I_{rsb-3o}) is used to mark the points of emphasis in hidden dental caries. Hence, the purpose of this study was to design a novel detection method of proximal caries, based on pixel gray values in digital subtraction radiography images, from a patient's single dental image, used for monitoring of dental caries.
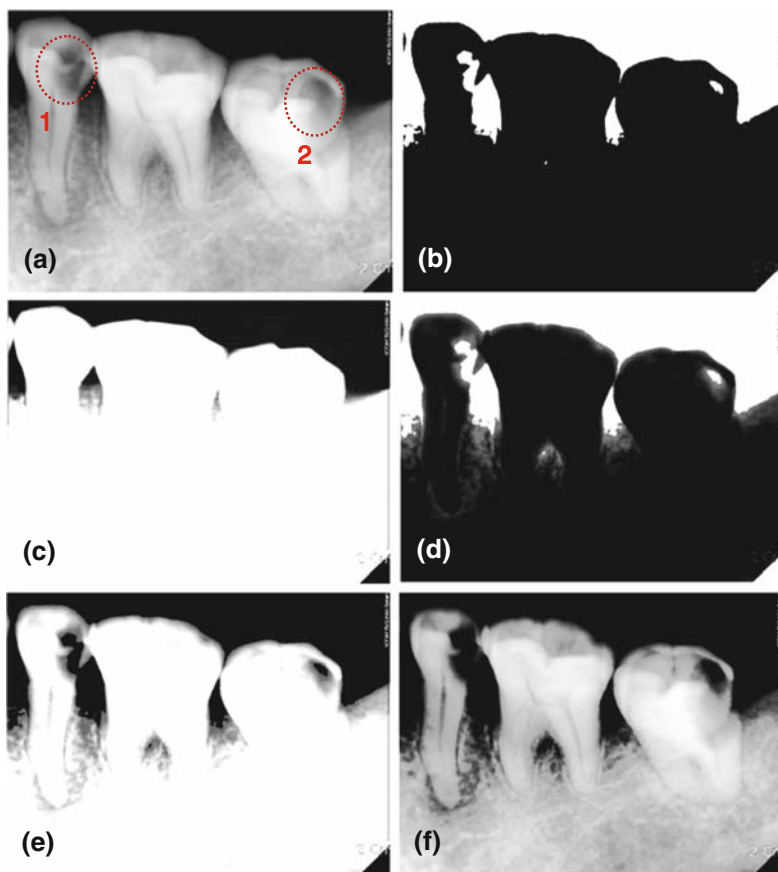
Fig. 15.2 Emphasis image of hidden proximal caries from single dental image of patient by digital subtraction radiography. (**a**) Original image. (**b**) Binary image. (**c**) Triploid original image. (**d**) Digital subtraction radiography. (**e**) Reverse image. (**f**) Emphasis image in hidden dental caries from final digital subtraction radiography

3   Experimental Results and Discussion

Digital radiology offers the opportunity to apply a sophisticated type of diagnostic technique, i.e., subtraction radiology. Suppose a digital bitewing radiograph is made for the purpose of caries diagnosis, and some time later a second digital radiograph of the exact same region is produced with identical exposure time, tube current and tube voltage. The numbers indicating the gray values in both digital images should be the same, except for sites where changes have occurred. By subtracting the gray values for each coordinate of the first radiograph from the equivalent coordinate of the second radiograph, a subtraction image is obtained. If no changes have occurred, the result of the subtraction is zero. A nonzero result will be obtained in the case of changes such as the onset or progression of demineralization. These sites can

be easily found by the observers on the subtraction images. In vitro studies have shown that the subtraction method could be a powerful tool in the diagnosis of secondary and primary caries [21, 22]. This image subtraction method, although commonly used in clinical dental research, has not yet routinely been applied in clinical caries diagnosis by general practitioners, mainly because of the difficulty of image registration, i.e., aligning the second radiograph with the first.

In this study, the advantage of single digital subtraction radiography is knowing the status of current teeth with caries without requiring a second digital radiograph. Figure 15.2 shows the resultant images obtained for proximal caries detection from a patient's single dental image by our novel detection method of proximal caries (Fig. 15.1). The X-ray dental image of Fig. 15.2a is first subjected to image pre-processing. Figure 15.2a reveals that caries of area 1 is very severe. However, the state of caries in area 2 is not clear. Figure 15.2c shows threefold processing of the triploid original image after image preprocessing, and Fig. 15.2b is the image of binary information from the original image. Figure 15.2d detects tissue mass changes by subtraction of the triploid original image from the binary image. Reverse image is the reversed image from Fig. 15.2d, that is, Fig. 15.2e. Final digital sub-traction radiography, Fig. 15.2f, detects tissue mass changes by subtraction of the reverse image from the original image. After all, Fig. 15.2f shows the only image in this study used to mark the points of emphasis in hidden dental caries. The goal of this study was the monitoring of proximal caries by digital subtraction radiog-raphy. However, few studies have focused on the quantitative radiographic analysis of mineral changes, especially in in vivo experiments [23–25]. This is probably due to the difficulties involved in standardizing methods and controlling clinical variables in human settings. This research protocol simulates controlled clinical procedures which may vary in routine clinical practice. In a clinical validity study, Nummikoski et al. [26] found that digitized radiographs and subsequent subtraction presented greater accuracy in the detection of alveolar crestal bone loss compared with conventional film viewing. The same procedures were also successfully used by Eberhard et al. [24] for monitoring in vitro dental demineralization and by Ortman et al. [27] for detecting changes in alveolar bone defects with bone loss in the range of 1–5%. It is known that digital radiographic imaging has the advan-tage of reducing work time, but some practical disadvantages, such as the difficulty in positioning the rigid sensor intraorally, reduce image reproducibility and com-monly result in undesired retakes. Greater values were observed for remineralized lesions, lower values for demineralized lesions, while intermediary values (near 128 gray value) were consistent with stabilized lesions.

4 Conclusions

Digital radiology offers the opportunity to apply a sophisticated type of diagnos-tic technique, i.e., subtraction radiology. For example, a digital bitewing radiograph is made for the purpose of caries diagnosis, and some time later a second digital radiograph of the exact same region is produced with identical exposure time, tube

current and tube voltage. It has been demonstrated that pixel gray value measurements in subtraction radiography images may constitute a suitable complementary method for monitoring outcomes of the remineralization protocol. This image subtraction method, although commonly used in clinical dental research, has not yet routinely been applied in clinical caries diagnosis by general practitioners, mainly because of the difficulty of image registration, i.e., aligning the second radiograph with the first. Hence, the purpose of this study was to design a novel detection method of proximal caries, based on pixel gray values in digital subtraction radiography images from a patient's single dental image, used for monitoring of dental caries.

In digital subtraction radiography, the image is used to mark the points of emphasis in hidden dental caries, hence the novel monitoring method of dental caries in this study. Evaluating lesion behavior over time, we found higher interobserver agreement with assessment of subtraction images than in comparison of two digital bitewing images. The results demonstrated that digital subtraction radiography from a patient's single radiographic image was highly efficient in the detection of dental caries compared to the data from a simple digital radiograph.

References

1. Brent Dove, S., McDavid, W.D., Hamilton, K.E.: Analysis of sensitivity and specificity of a new digital subtraction system. Oral Surgery, Oral Medicine, Oral Pathology, Oral Radiology & Endodontics, 89, 771–776 (2000)
2. Matteson, S.R., Deahl, S.T.: Advanced imaging methods. Critical Review Oral Biology and Medicine, 7, 346–395 (1996)
3. Fidler, A., Liker, B.: Influence of developer exhaustion on accuracy of quantitative digital subtraction radiography. Oral Surgery, Oral Medicine, Oral Pathology, Oral Radiology & Endodontics, 90, 233–239 (2000)
4. Christgau, M., Hiller, K.A.: Quantitative digital subtraction radiography for the determination of small changes in bone thickness. Oral Surgery, Oral Medicine, Oral Pathology, Oral Radiology & Endodontics, 85, 462–472 (1998)
5. Woelfel, J.B.: Dental anatomy: its relevance to dentistry, 4th ed. Lee & Febiger, Malvern, PA (1990)
6. Bragger, U.: Digital imaging in periodontal radiography. A review. Journal of Clinical Periodontology, 15, 551–557 (1988)
7. Reddy, M.S., Jeffcoat, M.K.: Digital subtraction radiography. Dental Clinics of North America, 37, 553–565 (1993)
8. Vandre, R.H., Webber, R.L.: Future trends in dental radiology. Oral Surgery, Oral Medicine, Oral Pathology, Oral Radiology & Endodontics, 80, 471–478 (1995)
9. Woo, B.M.S., Zee, K.-Y.: In vitro calibration and validation of a digital subtraction radiography system using scanned images. Journal of Clinical Periodontology, 30, 114–118 (2003)
10. Vannier, M.W.: Subtraction radiography. Journal of Periodontology, 67, 949–950 (1996)
11. Webber, R.L., Ruttimann, U.E., Grondahl, H.G.: X-ray image subtraction as a basis for assessment of periodontal changes. Journal of Periodontal Research, 17, 509–511 (1982)
12. Grondahl, H.G., Grondahl, K., Webber, R.L.: A digital subtraction technique for dental radiography. Oral Surgery, Oral Medicine, Oral Pathology, 5, 6–102 (1983)

13. Hausmann, E., Christersson, L.: Usefulness of subtraction radiography in the evaluation of periodontal therapy. Journal of Periodontology, 56(Suppl), 4–7 (1985)
14. Reddy, M.S., Wang, I.C.: Radiographic determinants of implant performance. Advances in Dental Research, 13, 136–145 (1999)
15. Wenzel, A., Anthonisen, P.N., Juul, M.B.: Reproducibility in the assessment of caries lesion behaviour: a comparison between conventional film and subtraction radiography. Caries Research, 34, 214–218 (2000)
16. Eberhard, J., Hartman, B.: Digital subtraction radiography for monitoring dental demineralization. Caries Research, 34, 219–224 (2000)
17. Ratledge, D.K., Kidd, E.A.M., Beighton, D.: A clinical and microbiological study of approximal carious lesions. Part 1: the relationship between cavitation, radiographic lesion depth, the site specific gingival index and the level of infection of the dentine. Caries Research, 35, 3–7 (2001)
18. Bader, J., Shugars, D.: Need for change in standards of caries diagnosis epidemiology and health services research perspective. Journal of Dental Education, 57, 415–421 (1993)
19. Wenzel, A.: Influence of computerized information technologies on image quality in dental radiographs. Danish Dental Journal, 95, 527–559 (1991)
20. Wenzel, A., Halse, A.: Digital subtraction radiography after stannous fluoride treatment for occlusal caries diagnosis. Oral Surgery, Oral Medicine, Oral Pathology, 74, 824–828 (1992)
21. Minah, G.E., Vander, R.H., Talaksi, R.: Subtraction radiography of dentinal caries-like lesions induced in vitro by cariogenic bacteria. Pediatric Dental, 20, 345–349 (1998)
22. Nummikoski, P.V., Martinez, T.S., Matteson, S.R., McDavid, W.D., Dove, S.B.: Digital subtraction radiography in artificial recurrent caries detection. Dentomaxillofacial Radiology, 21, 59–64 (1992)
23. Wenzel, A.: Digital radiography and caries diagnosis. Dentomaxillofacial Radiology, 27, 3–11 (1998)
24. Eberhard, J., Hartman, B., Lenhard, M., Mayer, T., Kocher, T., Eickholz, P.: Digital subtraction radiography for monitoring dental demineralization. An in vitro study. Caries Research, 34, 219–224 (2000)
25. Parks, E.T., Williamson, G.F.: Digital radiography: an overview. The Journal of Contemporary Dental Practice, 3, 23–39 (2002)
26. Nummikoski, P.V., Steffensen, B., Hamilton, K., Dove, S.B.: Clinical validation of a new subtraction radiography technique for periodontal bone loss detection. Journal of Periodontology, 71, 598–605 (2000)
27. Ortman, L.F., Dunford, R., McHenry, K., Hausmann, E.: Subtraction radiography and computer assisted densitometric analyses of standardized radiographs. A comparative study with 125I absorptiometry. Journal of Periodontal Research, 20, 644–651 (1985)

Index

Note: The letters 'f' and 't' following the locators refer to figures and tables respectively